Electromagnetic aspects of ESPAR and digitally controllable scatterers with a look at low-complexity algorithm design

Juan Bucheli Garcia

INSTITUT POLYTECHNIQUE DE PARIS

NNT : 2020IPPAT004

Thèse de doctorat

Electromagnetic aspects of ESPAR and digitally controllable scatterers with a look at low-complexity algorithm design

Thèse de doctorat de l'Institut Polytechnique de Paris
préparée à Télécom Paris

École doctorale n°626 Telecom Paris (ED IP Paris)
Spécialité de doctorat: Information, communications, électronique

Thèse présentée et soutenue à Paris, le 6 Février 2020, par

JUAN CARLOS BUCHELI GARCIA

Composition du Jury :

Martine Liénard Prof., Univ. Lille	Présidente
Constantinos Papadias Prof., Athens Information Technology Inst.	Rapporteur
Guillaume Villemaud Assoc. Prof., INSA Lyon	Rapporteur
Martine Liénard Prof., Univ. Lille	Examinatrice
Marco Di Renzo Senior Researcher, CNRS CentraleSupelec	Examinateur
Alain Sibille Prof., Telecom Paris	Directeur de thèse
Mohamed Kamoun Research Eng., Huawei France	Co-directeur de thèse

Preface

This dissertation is submitted in partial fulfillment of the requirements for the degree of Philosophiae Doctor at the department of communications and electronics (*COMELEC* by its initials) in Telecom Paris, a member of the Institut Polytechnique de Paris in Palauseau, France. The project has also been carried out at the Mathematical and Algorithmic Science Lab, Huawei FRC in Boulogne-Billancourt, France.

In particular, as an industry oriented doctorate, Alain Sibille and Mohamed Kamoun have been my supervisors from Telecom Paris and Huawei technologies, respectively.

The current manuscript is meant to be self-contained as way to highlight the main contributions during the three-year research project. More precisely, the contents were subdivided in three *parts*, defined so that anyone interested in the fundamentals can rely on the document itself, specifically, as an introduction to the most relevant matters.

As a note to the reader interested in the central topics of research, departing from Chapter 5 shall be sufficient as a way to follow the main arrived-at conclusions. Indeed, references to the relevant subjects under consideration (in the so-called *Fundamentals* part) are commonplace. Nonetheless, whenever possible, it is recommended to follow the progression of the document from the very beginning, which was intended to give a better understanding of the material.

Paris, France. February 11, 2020.

Acknowledgments

As it is often the case, I would like to begin this dissertation by the so-deserved acknowledgments. Firstly, because this project extends well beyond the document itself and, in my head, it makes some sense to place it at the beginning to mark its precedence and relevance.

That being said, I have been lucky enough to be surrounded by people that contributed to my life during these years. My parents and sister, relatives, friends and love. I think, and I hope, I have made them well-aware of their impact in my life. It is thanks to each and all of them that I could not only go through the challenges, but grow with them while enjoying the successes.

Last, but indeed not least, I would like to thank my supervisors Mohamed Kamoun from Huawei and Alain Sibille from Telecom Paris. It is thanks to them that this project sees the end after tons of hours of enriching discussion. It has been gratifying to learn from their expertise, which is only superseded by their human quality, as they made me feel all along the project.

Introduction

This project has been conceived thanks to the collaboration of industry and academia through the support of the french government via the CIFRE program (standing for Conventions Industrielles de Formation par la Recherche). On the one hand, around 80% of the work has been carried out at Huawei's Mathematical and Algorithmic Science Lab in Boulogne-Billancourt and, the other 20%, at Telecom Paris as the doctoral school under the supervision of both Prof. Alain Sibille and Dr. Mohamed Kamoun from the academia and industry, respectively.

The interest in this project arises from the need of alternative multi-antenna architectures to deal with the continuously increasing requirements with looks at reducing energy consumption and fabrication cost. Thus, the thesis focuses on the idea of exploiting the spatial domain (as opposed to the exploitation of the time-frequency resource) of wireless environments from two *fronts*: a) ESPAR antennas (standing for Electronically Steerable Parasitic Array Radiator) as a potential inexpensive alternative to conventional multi-antenna architectures[1], and b) the study of reactively loaded arrays to deliver controllable scattering as a mean of adding degrees of freedom to the propagation environment itself.

As a way to understand the structure of this manuscript, in connection to that of the project, it is appropriate to highlight the importance given to the interface between electromagnetism and the signal characterization. More specifically, both of the so-mentioned work-*fronts* require the understanding of electromagnetic (EM) phenomena that is not fully accounted for through conventional link-level descriptions. More importantly, the latter is proof of the need to join the approaches of the two related research communities to cope with the scarcity of resources that is only expected to grow in the decades to come.

In fact, this document is mostly positioned from the view of someone with a background in telecommunications (unlike pure electromagnetism)

[1]– inexpensive in relation to the number of radio frequency front-ends these conventional architectures are often assumed to be provided with.

with looks at enlightening the underlying EM mechanisms. It is roughly composed of three parts, namely: fundamentals, the ESPAR antenna and digitally controllable scatterers. In fact, the aim of having one part of the document dedicated purely to fundamentals is to describe the EM phenomena while highlighting all relevant details to the remaining two.

More specifically, the part *fundamentals* begins with Maxwell's equations (and their convenient solution for far-field radiation problems) all the way to the well-known $y = hx + n$ signal characterization many of us without a pure background in electromagnetics feel so comfortable with. As the seemingly least appropriate description to work with[2] but most complete characterization of the EM phenomena, Maxwell's equations are the basis that link our mathematical description to the very same reality. Thus, the objective of this part is to expose the connection between fields and signals, as well as to open the door to questioning the conventional transmitter-receiver signal model. The latter is one of the most exciting outcomes of this project in line with the research-related aim of challenging our vision to expand our understanding of a problem.

To continue, the second part is dedicated to the ESPAR antenna as a preamble of what is meant by "questioning the conventional transmitter-receiver signal model". Particularly, ESPAR obliges us to depart from the abstract signal space in which traditional multi-antenna link-level characterizations are depicted. As a contribution of this work, it will be shown how a local approximation of the system model offers an alternative view. Notably, through such an approximation of the system model, a computationally-efficient solution to the non-trivial problem of channel-based adaptation of the radiation characteristics of ESPAR is found.

Last, but not least, the third part deals with digitally controllable scatterers as a mean of improving energy efficiency. Such an exciting concept has gained significant attention in the recent years and, in a sense, opens the door to a radically different way to conceive communication problems. Even though these devices are in their infancy, it is not difficult for me to imagine how the decades to come could be marked by the massification of this technology.

One of the main contributions of this project is, in fact, the understanding of how digitally controllable scatterers allow to defy the view of wireless environments as unavoidably contingent. As a preamble, one outcome of this project was to show that, through the adoption of this technology, free-space propagation can be outperformed under entirely obstructed (also known as non-line-of-sight) propagation conditions.

[2]– from a conventional link level perspective

Contributions

Along this project several papers have been submitted to peer-reviewed conferences and journals. Particularly, four conference papers have been published, another one has been recently accepted for publication, and two journal papers are under review (among which one is in *minor revision*).

Notably, related to ESPAR, an approximation of its admittance matrix was proposed. The latter allowed to linearize the system model in order to solve the problem of channel-state-based reactance optimization for analog beam-forming, particularly, at a significantly low computational complexity with respect to existing work in the literature.

Moreover, the linearization was further exploited as a mean to come up with a real-time (i.e. sample-per-sample update) algorithm that solves the previous problem, in specific, avoiding the need to know the complex impedance matrix and channel state vector. Such an algorithm, relying solely on a-priori-known pilot symbols, is able to adapt the radiation properties of ESPAR with as few as 50 pilot symbols for a five element array.

On the other hand, related to DCS, the derivation of a dipole based and impedance controlled antenna array was proposed as means of scattering characterization. The directional properties of different architectures, among which bulky and ground-plane backed, were analyzed and their models corroborated. Additionally, the interdependence of its physical size and the interacting Fresnel zones at the DCS location were found to be fundamental for their differentiation as scatterers or reflectors.

Particularly, it was shown that the key to understand and unify both such opposite behaviors lies in the appropriate identification of the array near field, and its further approximation. In fact, one of the contributions of this project is a way to seamlessly characterize DCS on all of its operation regions through the here-called generalized array manifold. Moreover, a compact yet thorough input-output link-level signal characterization for a wireless system in the presence of DCS was proposed.

The exhaustive list of publications can be found in Appendix F.

Context of the project

In light of the new set of telecommunication standards (usually grouped as generations), which is supposed to cope with the latest requirements in data transmission (given by applications as virtual and augmented reality, super-ultra high definition, big data, Internet of Things, etc.), alternative network infrastructures (to conventional ones, see Fig. 1) are envisaged to deal with some issues as coverage, network adaptability, among others. A more efficient infrastructure involve an active role of devices (among which users) in transmuting data to other users, comparable to relay-like broadcasters as in Fig. 2. The challenges the latter represents, nevertheless, are not straightforward.

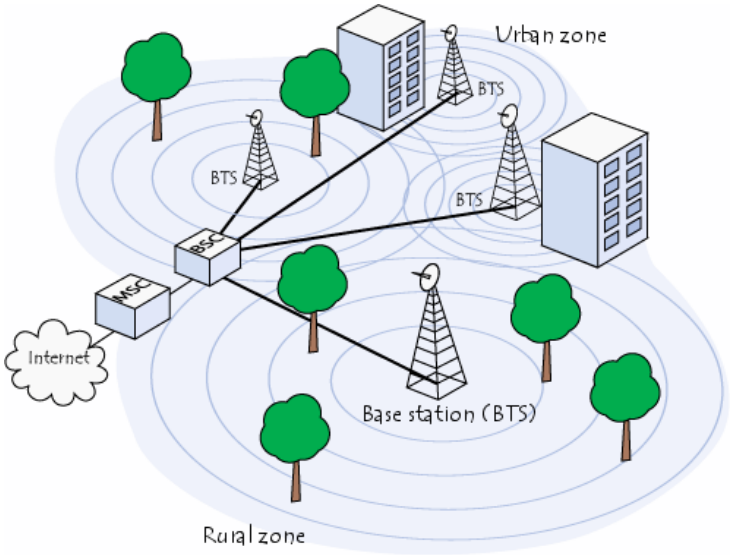

Figure 1: Representation of a conventional cell centric infrastructure such as the GSM network[3].

One important goal in recent generations of communications is the resource optimization in terms of energy efficiency as means of coping with

[3]Downloaded from url under license Creative Commons 3.0.

the high data demand with economic feasibility in mind. Understanding the main resources as time, frequency and space, the use of multi-antenna systems is fundamental to access the spatial domain of wireless environments.

Specifically, there is a strong effort in the research to exploit the high frequency spectrum with the so called millimeter-wave communications (for frequencies above 30 GHz). In this work, nonetheless, the focus is mostly placed on the spatial domain of wireless environments at the important sub-6 GHz part of the spectrum.

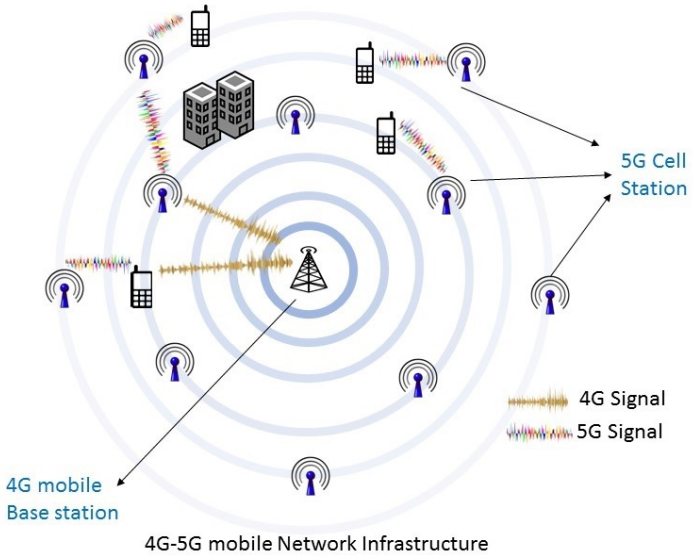

Figure 2: Representation of a network infrastructure in which all devices play an active role[4].

Although *old* in the scientific literature, multiple antenna systems are one of the topics that receive the most of attention nowadays due to the advances in the electronics required. Some of the most praised results include, under some assumptions, a linear increase in capacity with the minimum of the antennas at the transmitter and receiver sides. The latter, known as spatial multiplexing, makes use of the small coherence distance present on rich wireless multi-path channels. Particularly, it can be seen as having independent communication links on systems provided with antennas sufficiently separated in space. the latter means that, even-though signals are combined among different antennas at the receiver side, there is an algorithm that with high probability can separate the multiple streams that coincide both in the time and frequency domains.

[4]Downloaded from url under license Creative Commons 4.0.

From a more practical point of view several factors, such as production cost and energy consumption, are relevant of consideration for the operators and users with economic feasibility in mind.

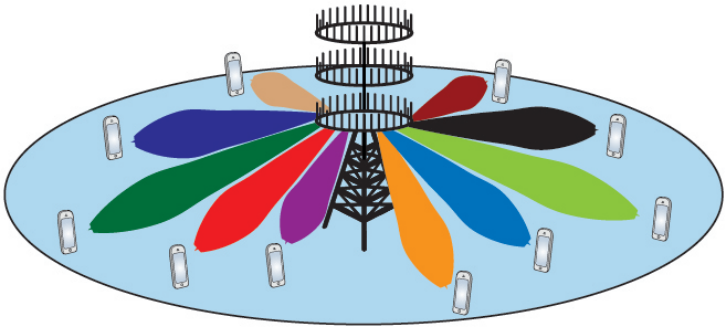

Figure 3: Massive MIMO scheme[5].

From the network perspective, one of 5G's key front-lines is the so called Massive MIMO. Massive MIMO involves the use of plenty of antennas (hundreds even, as pictorially represented in Fig. 3) on base stations in order to exploit the spatial domain mentioned. Nonetheless, unlike previously, as a way to increase the network capacity, even when user terminals are equipped with few antenna elements each, as in Fig. 4. Particularly, given that operators are willing to invest in order to increase the number of served users.

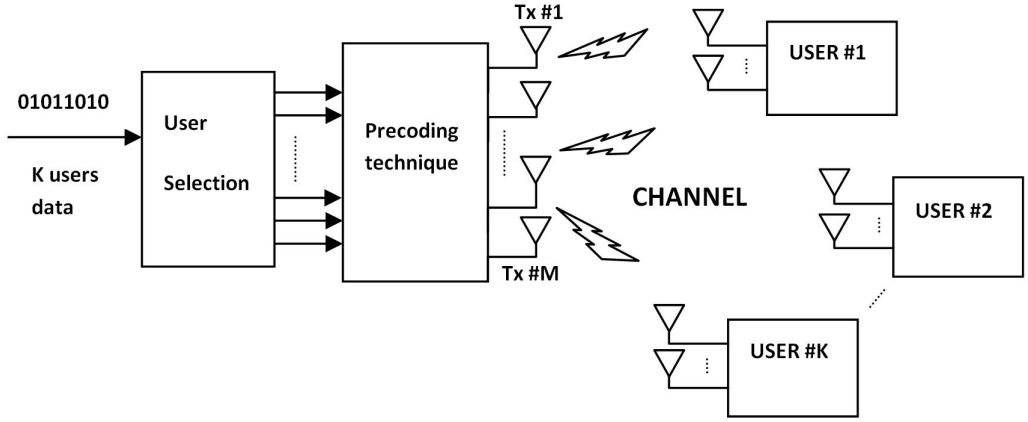

Figure 4: Multi user multiple input multiple output (MU-MIMO) scheme[6].

Coming back to the network represented on Figure 2, massive MIMO increases the network sum-rate for base-station related transmissions. Nev-

[5]Downloaded from url by kind permission of the author.
[6]Downloaded from url under license Creative Commons 4.0.

ertheless, the device-mediated and relayed transmissions remain challenging as close to channel capacities have already been achieved on SISO (singular input singular output), among others, by the use of advanced coding techniques.

As a consequence, new techniques that exploit spatial richness while having in mind cost, energy efficiency and physical adequacy are nowadays imperative.

This motivation leads to considering two concepts existing in the research even since decades ago, both of which have become more appealing in the recent years. In brief, the present work is based on the use of the electronically steerable parasitic array radiator (ESPAR) and digitally controllable scatterers (DCS) as a way to face such a challenge.

To conclude, as preamble, ESPAR refers to low-cost antenna array being fed by a single radio frequency (RF) front-end. Translating to the reduction of fabrication and operation costs. On the other hand, DCS correspond to the arrangement of a massive amount of inexpensive antenna elements with the objective of capturing and scattering energy in a controllable manner. As such, allowing to introduce degrees of freedom to the propagation environment itself.

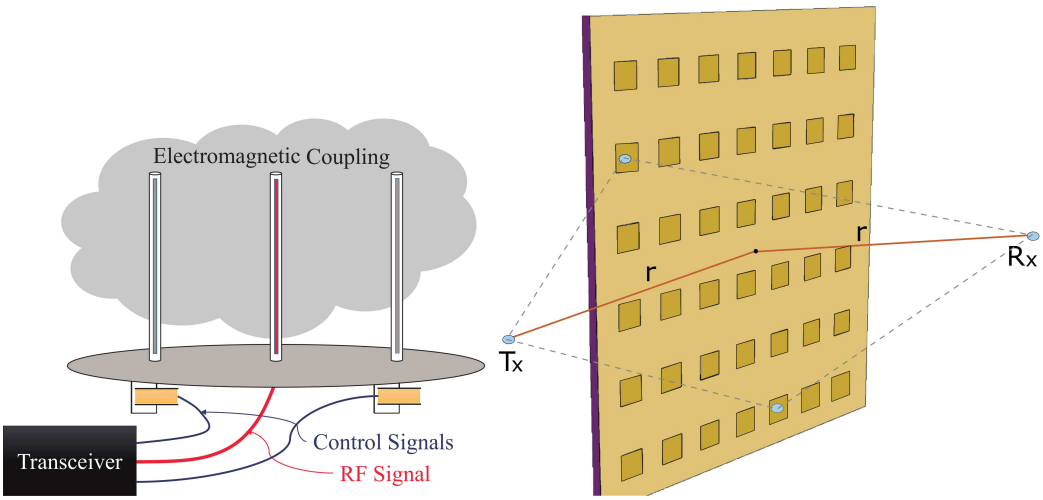

Figure 5: Example ESPAR antenna (left) and DCS (right)

Contents

Part I

Fundamentals

Chapter 1

Maxwell's equations

As mentioned, there is an interest on reviewing the fundamental electromagnetic (EM) phenomena that takes place in communication problems. Thus, Maxwell's equations and their solution will be briefly inspected for the region we are interested in analyzing the most, i.e. the far-field zone [1]. Moreover, the superposition principle and boundary conditions, that are key to the understanding of antennas as receivers and as scatterers, will also be looked at. These are relevant concepts to gain intuition on the interaction among field quantities involved in all wireless communication problems.

Let us begin by one of the most fundamental descriptions we have of the EM phenomena: Maxwell's equations in steady state under harmonic excitation:

$$\begin{aligned} \nabla \cdot \boldsymbol{D} &= \rho, \\ \nabla \cdot \boldsymbol{B} &= 0, \\ \nabla \times \boldsymbol{E} &= -\jmath\omega \boldsymbol{B}, \\ \nabla \times \boldsymbol{H} &= \boldsymbol{J} + \jmath\omega \boldsymbol{D}. \end{aligned}$$

In the previous equations, uppercase letters represent complex field quantities on any arbitrary spatial system of coordinates. In particular, $\boldsymbol{E}$ represents the electric field intensity in units of ${}^{volt}/_{m}$, $\boldsymbol{H}$ the magnetic field intensity in units of ${}^{ampere}/_{m^2}$, $\boldsymbol{J}$ the electric current density accounting for external sources in units of ${}^{ampere}/_{m}$ and ρ the volumetric charge density in units of ${}^{coulomb}/_{m^3}$. Additionally, $\boldsymbol{D}$ represents the electric displacement in units of ${}^{coulomb}/_{m^2}$ and $\boldsymbol{B}$ the magnetic induction in units of ${}^{weber}/_{m^2}$ or $tesla$.

In order to gain insight of these equation, note first that there exist constitutive relations between the field intensities $\boldsymbol{E}$, $\boldsymbol{H}$ and the flux densities $\boldsymbol{D}$, $\boldsymbol{B}$. We could imagine the field intensities as the way the medium reacts

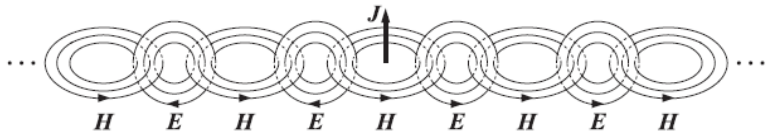

Figure 1.1: Representation of EM radiation.
Extract [2], educational use. S. J. Orfanidis © 2016.

to the presence of the flux densities $\boldsymbol{D}$ and $\boldsymbol{B}$ through:

$$\boldsymbol{D} = \epsilon \boldsymbol{E} \quad = \epsilon_0 \epsilon_r \boldsymbol{E}, \tag{1.1}$$

$$\boldsymbol{B} = \mu \boldsymbol{H} \quad = \mu_0 \mu_r \boldsymbol{H}. \tag{1.2}$$

The constitutive relations in (1.1) and (1.2) are for simple homogeneous and isotropic dielectrics as the ones we are interested in here. Additionally, ϵ and μ characterize, respectively, the electric and magnetic polarization properties of the material with the subindex 0 indicating their reference value for vacuum and r their material-specific relative value.

By the inclusion of such constitutive relations, Maxwell's equations take the convenient form:

$$\nabla \cdot \boldsymbol{E} \quad = \frac{1}{\epsilon}\rho, \tag{1.3}$$

$$\nabla \cdot \boldsymbol{H} \quad = 0, \tag{1.4}$$

$$\nabla \times \boldsymbol{E} \quad = -\jmath\, \omega \mu\, \boldsymbol{H}, \tag{1.5}$$

$$\nabla \times \boldsymbol{H} \quad = \boldsymbol{J} + \jmath\, \omega \epsilon\, \boldsymbol{E}. \tag{1.6}$$

Equations (1.3) to (1.6) give a complete description of the curl and divergence[1] of both the electric and magnetic field intensities in the presence of the source electric current density $\boldsymbol{J}$. Moreover, in the source-free region (i.e. $\boldsymbol{J} = \mathbf{o}$ and $\rho = 0$), note that the curl in (1.5) and (1.6) do not immediately vanish but exhibit a harmonic dependence; leading to what is known as EM radiation; shown away from $\boldsymbol{J}$ in Fig. 1.1.

To continue, let us recall that (1.4) is a direct consequence of the non-existence of magnetic monopoles. The latter translates to that, while $\boldsymbol{E}$ generally has divergent and rotational components, $\boldsymbol{H}$ can be described entirely in terms of a vector potential (i.e. as the rotational of another vector field).

[1] therefore completely characterizing these fields under appropriate conditions of smoothness and decay, according to the fundamental theorem of vector calculus [3].

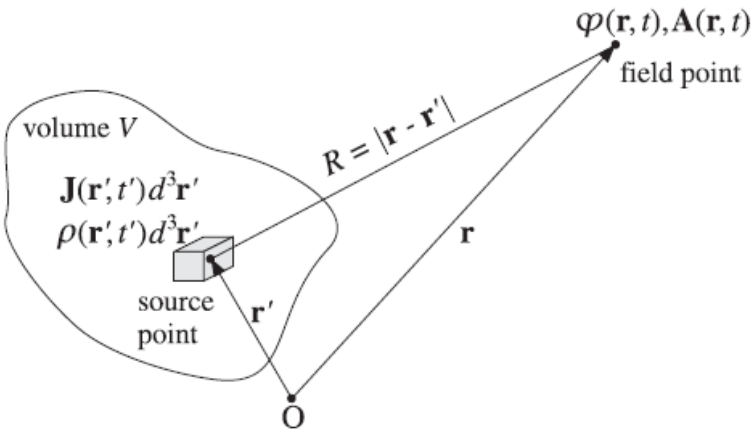

Figure 1.2: Representation of source and field points.
Extract [2], educational use. S. J. Orfanidis © 2016.

Thus, through Helmholtz decomposition [3], it can be shown[2] that $\boldsymbol{E}$ and $\boldsymbol{H}$ can be jointly decomposed into a vector potential $\boldsymbol{A}$ (also known as magnetic potential) and a scalar potential φ (also known as electric potential), namely:

$$\boldsymbol{E} = -\nabla\varphi - \jmath\omega\boldsymbol{A}, \tag{1.7}$$

$$\boldsymbol{H} = \frac{1}{\mu}\nabla\times\boldsymbol{A}. \tag{1.8}$$

The previous transformation allows us to rewrite Maxwell's equations in an equivalent wave-equation form[3]:

$$\nabla^2\varphi + k^2\varphi = -\frac{1}{\epsilon}\rho, \tag{1.9}$$

$$\nabla^2\boldsymbol{A} + k^2\boldsymbol{A} = -\mu\boldsymbol{J}, \tag{1.10}$$

with $k = {}^{2\pi}/_{\lambda}$ being the free-space wavenumber. Moreover, because of the assumed harmonic time dependence for all quantities, e.g.

$$\varphi(\boldsymbol{r},t) = \varphi(\boldsymbol{r})\,\mathrm{e}^{\jmath\omega t},\ \ \boldsymbol{A}(\boldsymbol{r},t) = \boldsymbol{A}(\boldsymbol{r})\,\mathrm{e}^{\jmath\omega t},\ \ \rho(\boldsymbol{r},t) = \rho(\boldsymbol{r})\,\mathrm{e}^{\jmath\omega t},\ \text{ etc.},$$

the solution for (1.9) and (1.10) to the excitations $\boldsymbol{J}$ and ρ can be given in convolutional form as:

$$\varphi(\boldsymbol{r}) = \frac{1}{\epsilon}\int_V \rho(\boldsymbol{r}')G(\boldsymbol{r}-\boldsymbol{r}')\,d^3\boldsymbol{r}', \tag{1.11}$$

[2]– see chapter 15 of [2].

[3]Lorenz condition ($\nabla\cdot\boldsymbol{A} + \frac{\jmath\omega}{c^2}\varphi = 0$) is also imposed in (1.9) and (1.10) to break the gauge invariance; which in fact results in charge conservation law [2].

$$\boldsymbol{A}(\boldsymbol{r}) = I_{\mathrm{m}}\,\mu \int_V \boldsymbol{J}_0(\boldsymbol{r}')G(\boldsymbol{r}-\boldsymbol{r}')\,d^3\boldsymbol{r}', \tag{1.12}$$

where $\boldsymbol{r}$ is the field (observation) point, $\boldsymbol{r}'$ is the source (integration) point (i.e. over V that is a volume containing all sources as shown in Fig. 1.2) and the source current density has been re-expressed as $\boldsymbol{J}(\boldsymbol{r}) = I_{\mathrm{m}}\,\boldsymbol{J}_0(\boldsymbol{r})$; with $\boldsymbol{J}_0(\boldsymbol{r})$ the normalized (to I_{m}) current distribution[4].

Note that $G(\boldsymbol{r})$ in (1.11) and (1.12) is the Green function of the Helmholtz equation:

$$\nabla^2 G(\boldsymbol{r}) + k^2 G(\boldsymbol{r}) = -\delta(\boldsymbol{r}),\;\; G(\boldsymbol{r}) = \frac{\mathrm{e}^{-\jmath kr}}{4\pi r}, \tag{1.13}$$

with $\delta(\boldsymbol{r})$ being the three-dimensional delta distribution and $r = |\boldsymbol{r}|$.

In particular, $G(\boldsymbol{r})$ can be seen as the impulse response or kernel of the system characterized by the wave differential equations (1.9) and (1.10). Moreover, (1.11) and (1.12) are of extreme relevance to the goal of linking the EM phenomena to signal processing.

More specifically, observe that the vector potential are linear on the excitation given by I_{m}. Additionally, the corresponding radiated field intensities $\boldsymbol{E}$ and $\boldsymbol{H}$ are also linear on the magnetic potential vector[5]. In other words, if we denote by $\boldsymbol{E}(I_n\,\boldsymbol{J}_n)$ and $\boldsymbol{H}(I_n\,\boldsymbol{J}_n)$ the field intensities at a given location $\boldsymbol{r}$ due to some current distribution $\boldsymbol{J}_n = \boldsymbol{J}_0(\boldsymbol{r}-\boldsymbol{r}_n)\,\forall\, n = 1, 2$, we can show that the superposition principle holds:

$$\boldsymbol{E}(I_1\,\boldsymbol{J}_1 + I_2\,\boldsymbol{J}_2) = I_1\boldsymbol{E}(\boldsymbol{J}_1) + I_2\boldsymbol{E}(\boldsymbol{J}_2), \tag{1.14}$$

$$\boldsymbol{H}(I_1\,\boldsymbol{J}_1 + I_2\,\boldsymbol{J}_2) = I_1\boldsymbol{H}(\boldsymbol{J}_1) + I_2\boldsymbol{H}(\boldsymbol{J}_2), \tag{1.15}$$

where the integration volume should entirely contain both $\boldsymbol{J}_1$ and $\boldsymbol{J}_2$.

1.1 Far-field solution with currents as sources

It must be stressed that, in spite of the simplification of Maxwell's equations as of (1.9) and (1.10), the solution for the potentials with harmonic currents as sources of fields is analytically difficult to work with regardless the coordinate system. In particular, the shifted argument of the Green function, i.e. $G(\boldsymbol{r}-\boldsymbol{r}')$ in (1.11) and (1.12), can be approximated for a region of validity known as far-field, namely through:

$$G(\boldsymbol{r}-\boldsymbol{r}') = \frac{\mathrm{e}^{-\jmath k|\boldsymbol{r}-\boldsymbol{r}'|}}{4\pi|\boldsymbol{r}-\boldsymbol{r}'|} \approxeq \frac{\mathrm{e}^{-\jmath k(r-\hat{\boldsymbol{r}}\cdot\boldsymbol{r}')}}{4\pi r}, \quad r \gg l \text{ and } r \gg \frac{2l^2}{\lambda} \tag{1.16}$$

[4]Particularly, I_{m} can be related to the input current to the antenna terminals.

[5]Note that, by the aid of the Lorentz condition, both $\boldsymbol{E}$ and $\boldsymbol{H}$ can be expressed completely in terms of such magnetic potential vector $\boldsymbol{A}$.

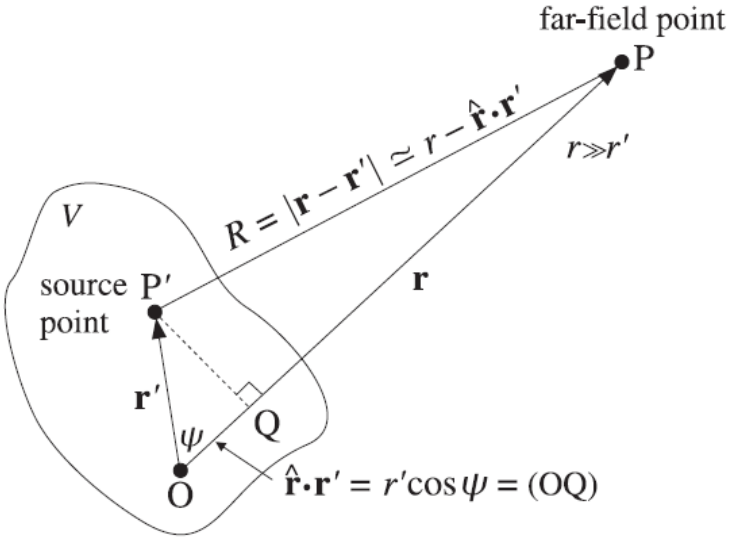

Figure 1.3: Representation of far field approximation.
Extract [2], educational use. S. J. Orfanidis © 2016.

where l is the largest dimension of the smallest integration volume containing all sources and $\hat{\boldsymbol{r}}$ is a unitary vector pointing at the far-field observation point as shown in Fig. 1.3.

More specifically, in (1.16), the dependence with the observation point in the numerator was replaced by a first order approximation whereas the denominator was replaced by an approximation of order zero.

Using the far-field approximation of the Helmholtz Green function we obtain for the far-field scalar and vector potentials:

$$\varphi(\boldsymbol{r}) = \frac{\mathrm{e}^{-\jmath kr}}{4\pi\epsilon r} \int_V \rho(\boldsymbol{r}')\mathrm{e}^{\jmath \boldsymbol{k}\cdot\boldsymbol{r}'}\, d^3\boldsymbol{r}',\ \ \boldsymbol{k} = k\hat{\boldsymbol{r}}, \tag{1.17}$$

$$\boldsymbol{A}(\boldsymbol{r}) = \frac{I_\mathrm{m}\,\mu\mathrm{e}^{-\jmath kr}}{4\pi r} \underbrace{\int_V \boldsymbol{J}_0(\boldsymbol{r}')\mathrm{e}^{\jmath \boldsymbol{k}\cdot\boldsymbol{r}'}\, d^3\boldsymbol{r}'}_{\boldsymbol{F}(\hat{\boldsymbol{r}})},\ \ \boldsymbol{k} = k\hat{\boldsymbol{r}}. \tag{1.18}$$

Note that the integrands in (1.17) and (1.18) correspond to a three dimensional Fourier transform of the sources.

Moreover, the so-called radiation vector is, thus, defined by:

$$\boldsymbol{F}(\hat{\boldsymbol{r}}) := \int_V \boldsymbol{J}_0(\boldsymbol{r}')\mathrm{e}^{\jmath \boldsymbol{k}\cdot\boldsymbol{r}'}\, d^3\boldsymbol{r}',\ \ \boldsymbol{k} = k\hat{\boldsymbol{r}}. \tag{1.19}$$

The addition of the radiation vector is very useful at this point given that, after employing the scalar and vector potentials as an intermediate step, the solution for the far-field electric and magnetic field intensities can be easily expressed in terms of the radiation vector. Moreover, as already mentioned, the radiation vector corresponds to the Fourier transform of the source current distribution; what is advantageous given that many properties and algorithms such as the fast Fourier transform (FFT) are well known.

To finish the current section we will jump directly to the anticipated result. More specifically, through the expressions for $\boldsymbol{E}$ and $\boldsymbol{H}$ in terms of the scalar and vector potentials of (1.9) and (1.10), the Lorenz condition to find $\varphi(\boldsymbol{r})$ in terms of $\boldsymbol{A}(\boldsymbol{r})$ and (1.18); it can be shown that $\boldsymbol{E}$ and $\boldsymbol{H}$ in the far-field approximation are given by:

$$\boldsymbol{E}(\boldsymbol{r}) = -\jmath\, I_{\mathrm{m}}\, k\eta \frac{\mathrm{e}^{-\jmath\, kr}}{4\pi r}\big[\hat{\boldsymbol{\theta}} F_\theta + \hat{\boldsymbol{\phi}} F_\phi + \hat{\boldsymbol{r}}\, 0\,\big], \tag{1.20}$$

$$\boldsymbol{H}(\boldsymbol{r}) = -\jmath\, I_{\mathrm{m}}\, k \frac{\mathrm{e}^{-\jmath\, kr}}{4\pi r}\big[\hat{\boldsymbol{\phi}} F_\theta - \hat{\boldsymbol{\theta}} F_\phi + \hat{\boldsymbol{r}}\, 0\,\big], \tag{1.21}$$

where $\eta = \sqrt{\mu/\epsilon}$ is known as the impedance of the medium, i.e. $\eta = 120\pi$ for vacuum.

In particular, (1.20) and (1.21) show explicitly that the fields in the far-field region both contain and depend exclusively on the components orthogonal to the direction of propagation (that is given by $\hat{\boldsymbol{r}}$). The latter is a consequence of the far-field approximation and is known as transversal electric magnetic (TEM) propagation.

Additionally, apart from belonging to the plane transversal to the direction of propagation, $\boldsymbol{E}$ and $\boldsymbol{H}$ form (with $\hat{\boldsymbol{r}}$) a right-handed vector system:

$$\boldsymbol{E} = \eta\, \boldsymbol{H} \times \hat{\boldsymbol{r}}, \tag{1.22}$$

$$\boldsymbol{H} = \frac{1}{\eta}\, \hat{\boldsymbol{r}} \times \boldsymbol{E}, \tag{1.23}$$

meaning that, in the far-field, knowing either $\boldsymbol{E}$ or $\boldsymbol{H}$ suffices to completely characterize the EM radiation.

The half-wave dipole case

Based on (1.17) and (1.18), the far-field radiation resulting from a simple geometry such as a linear wire can be easily computed. Moreover, given that thin half-wave dipoles have been extensively used throughout the whole thesis, the derivation of their radiated fields will be shown in detail.

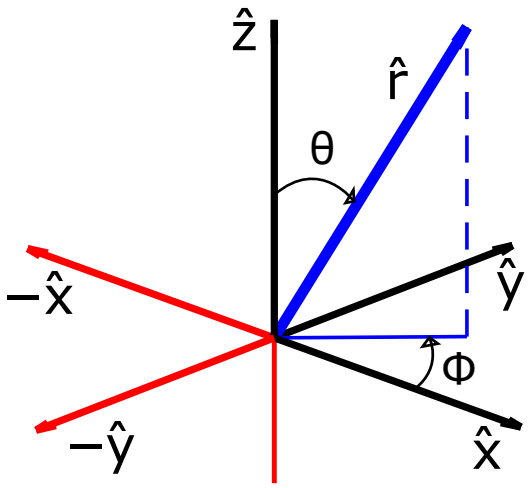

Figure 1.4: Representation of the adopted spherical coordinate system, i.e. $0 \leq \theta \leq \pi$ and $0 \leq \phi \leq 2\pi$

If we assume a vertically oriented wire in the positive $\hat{\boldsymbol{z}}$ direction according to the coordinate system of Fig. 1.4, the natural resonance of a thin half-wave dipole would result in a current distribution that can be well approximated as sinusoidal, i.e.:

$$\boldsymbol{J}_0(\boldsymbol{r}) = \hat{\boldsymbol{z}}\, \cos(kz)\delta(x)\delta(y), \quad |z| \leq \frac{\lambda}{4}. \tag{1.24}$$

According to the coordinate system of Fig. 1.4, the wavevector $\boldsymbol{k}$ is a function of the polar angle θ and azimuth angle ϕ, and it is given by:

$$\boldsymbol{k}(\theta,\phi) = k\hat{\boldsymbol{r}} = k\sin(\theta)\cos(\phi)\,\hat{\boldsymbol{x}} + k\sin(\theta)\sin(\phi)\,\hat{\boldsymbol{y}} + k\cos(\theta)\,\hat{\boldsymbol{z}}. \tag{1.25}$$

Therefore, the radiation vector contains only a vertical $\hat{\boldsymbol{z}}$ component. In particular it is given by:

$$\boldsymbol{F}(\boldsymbol{r}) = \hat{\boldsymbol{z}} \int_{-\frac{\lambda}{4}}^{\frac{\lambda}{4}} \cos(kz')\mathrm{e}^{\jmath\, k\cos(\theta)z'}\, dz'.$$

Furthermore, by substitution and integration by parts, such a vector can be shown to be equivalent to (in spherical coordinates):

$$\boldsymbol{F}(\boldsymbol{r}) = \overbrace{\left[\hat{\boldsymbol{r}}\cos\theta - \hat{\boldsymbol{\theta}}\sin\theta\right]}^{\hat{\boldsymbol{z}}} \frac{2}{k}\frac{\cos\left(\frac{\pi}{2}\cos\theta\right)}{\sin^2\theta}, \tag{1.26}$$

resulting, through (1.20), into an expression for the far-field electric field intensity given by:

$$\boldsymbol{E}(\boldsymbol{r}) = \hat{\boldsymbol{\theta}}\,\jmath\, I_\mathrm{m}\,\eta\frac{\mathrm{e}^{-\jmath kr}}{2\pi r}\frac{\cos\left(\frac{\pi}{2}\cos\theta\right)}{\sin\theta}, \tag{1.27}$$

where, to recall the reader, it can be clearly seen that $\boldsymbol{E}(\boldsymbol{r})$ is linear on the excitation at the center of the dipole (i.e. I_{m}) and as predicted by (1.14).

1.2 Boundary conditions

To recapitulate, in the first part of the current chapter it has been shown how currents act as sources of EM fields and, in particular, how these fields look like far away when a resonant half-wave dipole is excited at its center by a current I_{m}, i.e. (1.27).

As a means of understanding the opposite process, namely: how currents are induced as a result of incident EM waves, the current section will make an overview of basic yet important relations between EM fields when interacting on different media. Thus, we are interested in the interface between dielectrics (such as vacuum) and conductors.

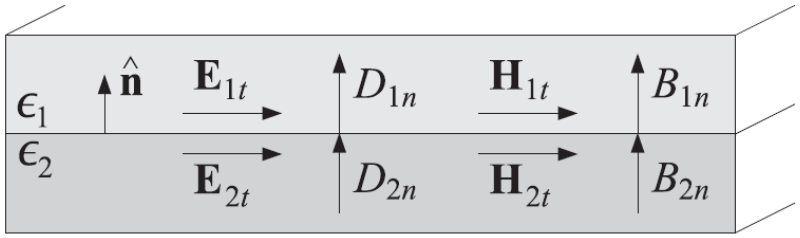

Figure 1.5: Depiction of boundary conditions between two different media. Extract [2], educational use. S. J. Orfanidis © 2016.

In particular, the boundary conditions describe constraints that EM fields should obey across such interfaces. These conditions can be derived from the integral form of Maxwell's equations after applying some regularity assumptions on the fields and are given by:

$$\begin{aligned}
\hat{\boldsymbol{n}} \times (\boldsymbol{E}_1 - \boldsymbol{E}_2) &= \mathbf{o}, \\
\hat{\boldsymbol{n}} \cdot (\boldsymbol{D}_1 - \boldsymbol{D}_2) &= \rho_s, \\
\hat{\boldsymbol{n}} \times (\boldsymbol{H}_1 - \boldsymbol{H}_2) &= \boldsymbol{J}_s, \\
\hat{\boldsymbol{n}} \cdot (\boldsymbol{B}_1 - \boldsymbol{B}_2) &= 0,
\end{aligned}$$

where the subindices 1 and 2 characterize the fields at the different media as shown in Fig. 1.5. Note that the previous conditions are enforced exclusively at the interface between the two media.

Moreover, recall that inside perfect electrical conductors (PEC) the net electric field is zero as a result of the free charges. In particular, as a reaction to any incident field $\boldsymbol{E}_{\text{inc}}$, free electrons displace and cause a field $\boldsymbol{E}_{\text{reac}}$ as *reaction* that is equal in magnitude and opposite in direction; effectively canceling out the total field inside the material.

The latter is key to the understanding of antennas in reception and, as will be seen later, of antennas working as scatterers of EM radiation. More specifically, when there is incident EM radiation from the first medium while the second medium is a PEC, the first boundary condition gives for the interface between both media:

$$\hat{\boldsymbol{n}} \times (\boldsymbol{E}_1 - \cancelto{\mathbf{o}}{\boldsymbol{E}_2}) = \mathbf{o}. \tag{1.28}$$

The implications of (1.28) are of prime importance to the current thesis. As the net tangential component of the electric field $\boldsymbol{E}_1$ at the boundary is zero, there are currents induced at the surface of the PEC that produce the field $\boldsymbol{E}_{1,\text{reac}}$ as *reaction*; effectively enforcing (1.28) through:

$$\hat{\boldsymbol{n}} \times \boldsymbol{E}_{1,\text{inc}} = -\hat{\boldsymbol{n}} \times \boldsymbol{E}_{1,\text{reac}}. \tag{1.29}$$

Nonetheless, given that (1.29) is only enforced at such an interface, the induced currents continue to radiate into the first medium. Even more, in the case where the PEC of the second medium corresponds to the surface of an antenna, the energy radiated by the *reaction* field can propagate into a transmission line and be used to sense what the antenna is effectively receiving.

Thus, apart from hinting on how receiving antennas work, the boundary conditions give an intuition on how antennas (or more generally conducting bodies) scattered fields that propagate back to the environment.

1.3 Overview

The chapter reviewed Maxwell's equations and their far-field solution for currents as sources. The superposition principle, as a result of the linearity of the convolutional operator, was also recalled as it plays a fundamental role in the link-level signal characterization. Moreover, the boundary conditions were presented as a means of giving a notion of such a process in the reverse direction, namely, reception and scattering due to incident EM radiation to a perfect electric conductor (PEC) material.

Chapter 2

Antennas as conductor-air interfaces

To proceed, the current chapter will be exclusively dedicated to the adoption of antennas as transmitting and receiving devices. The complete picture of antennas in the far-field linking the electrical and field perspectives, both in terms of its equivalent circuit and radiation pattern characterization, will be presented.

The chapter will close with an overview of the simplest power characterization of a transmitter-receiver link, known as link budget, for an unobstructed (also known as line-of-sight) scenario.

2.1 The electrical perspective

As exemplified through a half-wave dipole antenna, Maxwell's equations were used to find the far-field radiated electric field intensity $\boldsymbol{E}(\boldsymbol{r})$ as a (linear) function of the current at the antenna terminals I_{m}. Recalling the reader, this resulted in:

$$\boldsymbol{E}(\boldsymbol{r}) = \hat{\boldsymbol{\theta}}\, \jmath\, I_{\mathrm{m}}\, \eta \frac{\mathrm{e}^{-\jmath kr}}{2\pi r} \frac{\cos\left(\frac{\pi}{2}\cos\theta\right)}{\sin\theta}, \tag{1.27}$$

where the first link between a circuit quantity (the source current I_{m}) and a field quantity (the far-zone radiated electric field intensity $\boldsymbol{E}$) was hinted on. Consequently, the rest of the current section will introduce a more precise characterization of antennas as components of electrical circuits.

2.1.1 The effective length vector

Likewise, it can be shown that the electromotive force (emf) at the terminals of any antenna as a result of an incident EM field, characterized by $\boldsymbol{E}_{\text{inc}}$, can be equivalently expressed as [4]:

$$\mathcal{E} = \boldsymbol{l}_{\text{e}}(\hat{\boldsymbol{r}}_{\text{inc}}) \cdot \boldsymbol{E}_{\text{inc}}, \tag{2.1}$$

where $\boldsymbol{l}_{\text{e}}(\hat{\boldsymbol{r}}_{\text{inc}}) \in \mathbb{C}^3$ refers to what is known as the effective length vector of the antenna under consideration (evaluated at the direction of incidence of the field $\boldsymbol{E}_{\text{inc}}$).

Note that, according to (2.1), the impact on the induced emf due to a mismatch in polarization can be easily related to the cosine of the angle between the effective length vector $\boldsymbol{l}_{\text{e}}$ and the incident electric field intensity $\boldsymbol{E}_{\text{inc}}$. Moreover, through reciprocity considerations [5], the effective length vector can be related to the far-zone electric field intensity $\boldsymbol{E}$ radiated by such an antenna due to a given current at its terminals as [4]:

$$\boldsymbol{E}_{\text{rad}}(\boldsymbol{r}) := -\jmath\, I_{\text{m}}\, k\eta \frac{\mathrm{e}^{-\jmath kr}}{4\pi r} \boldsymbol{l}_{\text{e}}(\hat{\boldsymbol{r}}). \tag{2.2}$$

Consequently, from (1.20) and (2.2), the effective length vector of any antenna can be expressed in terms of the previously introduced radiation vector $\boldsymbol{F}$ as:

$$\boldsymbol{l}_{\text{e}}(\hat{\boldsymbol{r}}) := \boldsymbol{F}_{\perp}(\hat{\boldsymbol{r}}) = \hat{\boldsymbol{\theta}} F_{\theta}(\hat{\boldsymbol{r}}) + \hat{\boldsymbol{\phi}} F_{\phi}(\hat{\boldsymbol{r}}). \tag{2.3}$$

In the particular case of a vertically polarized half-wave dipole, and based on (1.26), such an effective length vector can be shown to be equivalent to:

$$\boldsymbol{l}_{\text{e}}(\hat{\boldsymbol{r}}) = -\hat{\boldsymbol{\theta}}\, \frac{2}{k} \frac{\cos\left(\frac{\pi}{2}\cos\theta\right)}{\sin\theta}. \tag{2.4}$$

Note also that, through (2.1) and (2.2), the field radiated by a transmitter antenna and the induced emf at a receiver antenna are fully described in terms of the so-defined effective length vector.

However, in order to fully characterize antennas as part of an electrical circuit (and predict issues such as impedance mismatch), an equivalent circuit representation of the antenna is required. In the following, given that voltages and currents can be defined at the antenna port, the concept of antenna impedance is introduced in order to construct such a circuit characterization.

2.1.2 Equivalent circuit representation of an antenna

To begin with, note that the voltage at the antenna port can be related to the line integral of the $\boldsymbol{E}$ field across the port terminals [2]. Moreover, recall

the important property of linearity of the $\boldsymbol{E}$ field[1] with the source current density as in (1.14). Thus, as a result of the linearity of the integro-differential operator, the voltage across the antenna terminals is also linearly related to the current at the antenna port.

The latter allows us to look at a transmitting antenna simply as an impedance[2] Z_A that extracts energy and radiates part of it into the surroundings. Additionally, given that we are dealing with time-harmonic fields, note that such an impedance is composed of both a resistive and a reactive component. In particular, its resistive component relates to energy being radiated[3] and dissipated due to ohmic or other losses in the materials. On the other hand, the reactive component of the antenna relates to energy confined in the form of electric and magnetic fields at the so-called near-field region of the antenna.

What's more, a receiving antenna can be equivalently represented by an ideal source with an emf given by (2.1) in series with Z_A debiting into the actual receiver load as shown in Fig. 2.1.

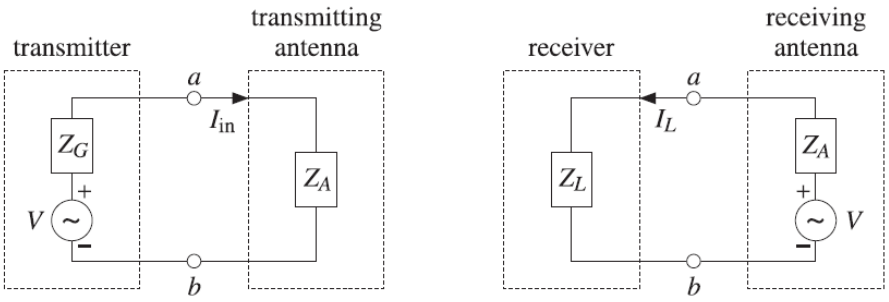

Figure 2.1: Circuit representation of an antenna in transmission (left) and reception (right). $V = \mathcal{E}$ and $I_{in} = I_{\text{m}}$ in connection with (2.1) and (2.2). Extract [2], educational use. S. J. Orfanidis © 2016.

Thus, by the inclusion of: first, the antenna impedance Z_A; second, its emf in reception (2.1) and; third, its radiated field in transmission (2.2), the precise link between the circuit and the field perspectives is revealed.

Lastly, in spite of the relevance of the antenna impedance as a means of characterizing it, the computation of such an impedance is omitted in the current thesis for brevity (in particular its reactive part being mathematically

[1]– this property holds at all regions, i.e. not only at the far-field region.

[2]– more precisely defined as the ratio of the voltage across its terminals to its input current.

[3]the term *radiated* refers to the far-field zone and, consequently, we refer here to energy contained in the fields characterized in Sec. 1.1.

extensive) as this is well documented in every book dealing with antenna theory [2, 5]. Nonetheless, it must be stressed that simple expressions have been found for the impedance of the type of antennas of interest for the current work [5], i.e. linear thin wire radiators.

2.2 The field perspective

After revealing a means for characterizing antennas as circuit components, it remains to introduce a way to describe the manner they radiate (or extract) energy to (or from) the environment in transmission (or reception). As a matter of fact, one consequence of the principle of reciprocity [5] is that the very same characterization applies both for antennas used in transmission or in reception.

Moreover, as will be explained in the following, only a directional characterization of the antenna is required. The latter is a direct consequence of the nature of far-field radiation in which the distance and angular dependencies are decoupled; effectively simplifying its description.

Finally, even though such a characterization could be carried out in the realm of the complex E and H fields, it will prove convenient to work in the domain of power[4]. In particular, working in the domain of power allows to connect more naturally with the yet-to-be-introduced notions of directivity, gain and effective area, apart from coming directly into play in the link budget.

2.2.1 The flux vector

To begin with, recall that the Poynting vector is a quantity that describes the flux of energy per unit area and unit time; generally in units of $^{\mathrm{W}}/_{m^2}$. More specifically, as the $\boldsymbol{E}$ and $\boldsymbol{H}$ fields are assumed to be time-harmonic, we are interested in the time averaged Poynting vector that describes the net flux of energy and is given by:

$$\boldsymbol{\mathcal{P}} = \frac{1}{2}\Re\{\boldsymbol{E}\times\boldsymbol{H}^*\} \overset{\text{far-field}}{\approx} \hat{\boldsymbol{r}}\,\frac{1}{2\eta}|\boldsymbol{E}|^2. \tag{2.5}$$

Moreover, in connection to the radiation vector[5] defined in Sec. 1.1 for the field radiated by a given source current, the flux vector can be re-expressed shortly as:

$$\boldsymbol{\mathcal{P}}(\boldsymbol{r}) = \hat{\boldsymbol{r}}\,\mathcal{P}_r = \hat{\boldsymbol{r}}\,\frac{\eta k^2|I_{\mathrm{m}}|^2}{32\pi^2 r^2}|\boldsymbol{F}_\perp(\hat{\boldsymbol{r}})|^2, \tag{2.6}$$

[4]– the Poynting vector's or a domain alike.

[5]– therefore applicable at the far-field region.

where the scalar function $\mathcal{P}_r$ is known as the radiation density and $|\boldsymbol{F}_\perp(\hat{\boldsymbol{r}})|^2$ corresponds to the squared norm of the radiation vector after the removal of the component in the direction of propagation; i.e. removing its $\hat{\boldsymbol{r}}$ component. As aforementioned, it is also clear from (2.6) that the distance and angular dependencies can be decoupled into the product of two factors.

Even more, note that (2.6) shows that the energy carried by the EM radiation decreases locally with r^2. Fundamentally, according to it, the radiation is contained at the surface of a sphere[6] whose area grows with the observation distance.

Nonetheless, as we are assuming a lossless antenna and propagation environment, it can be shown that:

$$P_{\text{rad}} := \oint_{S(V)} \boldsymbol{\mathcal{P}} \cdot \hat{\boldsymbol{n}}\, dS = \frac{1}{2}|I_{\text{m}}|^2 \Re\{Z_A\}, \tag{2.7}$$

where S is any closed surface surrounding a volume V that fully contains the antenna, $\hat{\boldsymbol{n}}$ is a unit norm vector pointing outwards from such a surface and dS is an infinitesimal surface element.

Note that, as the right hand side of the previous equation is the power extracted by the antenna resistance, (2.7) is simply a consequence of conservation of energy for the case in which no dissipative losses exist.

Moreover, (2.7) allows to study the radiation of a physically unrealizable yet useful reference antenna: the isotropic radiator. In particular, fixing the total radiated power, the directional characteristics of any antenna can be compared to those of a fair[7] isotropic radiator.

Thus, choosing $S(V)$ in (2.7) as the surface of a sphere of radius r, the flux resulting from an isotropic radiator can be shown to be equivalent to:

$$\boldsymbol{\mathcal{P}}^{\text{iso}}(r) = \hat{\boldsymbol{r}}\, \mathcal{P}_r^{\text{iso}} = \hat{\boldsymbol{r}}\, \frac{P_{\text{rad}}}{4\pi r^2}, \tag{2.8}$$

that is to say, the density of the radiated power is *uniformly* spread across the propagating wavefront (i.e. the surface area of the sphere of radius r).

2.2.2 Directivity, gain and effective area

Consequently, joining (2.6) and (2.8), the far-field metric known as directivity can be now precisely defined. In particular, the directivity measures how much is gained in a specific direction[8] by using a given antenna instead of

[6]– centered at the antenna location with a radius of r.

[7]fair in the sense that it does not exhibit any preferred direction of radiation.

[8]– for a fixed total radiated power.

a hypothetical isotropic radiator. Thus, it is defined as the ratio of the radiation intensity of such an antenna to that of an isotropic radiator for the same net radiated power, i.e.

$$D(\hat{\boldsymbol{r}}) := \frac{\mathcal{P}_r}{\mathcal{P}_r^{\text{iso}}} = \frac{\eta\, k^2 |I_{\text{m}}|^2}{8\pi P_{\text{rad}}} |\boldsymbol{F}_\perp(\hat{\boldsymbol{r}})|^2. \tag{2.9}$$

Note from (2.9) that, due to the nature of the far-zone fields, the directivity is a function of the direction of observation and, particularly, it is independent of the observation distance.

Nevertheless, recall that P_{rad} in (2.7) refers to effectively radiated power; which is in practice lower than the power *accepted* by the antenna terminals due to conduction losses at the antenna. Therefore, and because of the difficulty on modeling conduction losses, the *accepted* power P_T is often characterized in terms of a factor known as the radiation efficiency e, namely:

$$P_{\text{rad}} = e\, P_T \tag{2.10}$$

where $0 \leq e \leq 1$. Moreover, as per (2.9), the metric of antenna gain is defined in the same way as the directivity but, instead, relative to the power accepted by the antenna terminals; namely:

$$G(\hat{\boldsymbol{r}}) = \frac{\eta\, k^2 |I_{\text{m}}|^2}{8\pi P_T} |\boldsymbol{F}_\perp(\hat{\boldsymbol{r}})|^2. \tag{2.11}$$

Additionally, based on (2.9) and (2.10), the antenna gain and directivity are related simply by $G(\hat{\boldsymbol{r}}) = e\, D(\hat{\boldsymbol{r}})$.

It is important to highlight the usefulness of the antenna directivity and gain as means of characterizing (exclusively) the directional behavior of antennas in the far-field. Thus, the radiation density of a transmitter antenna can be expressed simply in terms of the power accepted by the antenna terminals and the gain as:

$$\mathcal{P}_r(\boldsymbol{r}) = \frac{P_T}{4\pi r^2}\, G(\hat{\boldsymbol{r}}). \tag{2.12}$$

Note that the radiation density describes the power per unit area contained in an EM field from which, in reception, an antenna would be able to extract energy. As a consequence, the notion of an area from which the receiver antenna is able to *collect* energy can be introduced.

Therefore, the effective area A is defined as that area which multiplied by the incident radiation density gives the power available[9] at the output

[9]The available power in the sense used here corresponds to the power delivered via conjugate matching.

antenna terminals. With the aid of the circuit representation of Sec. 2.1.2 in connection with (2.11) and after many simplifications, it can be shown to be simply related to the antenna gain as [2]:

$$A(\hat{\boldsymbol{r}}) := \frac{P_{R,\,\mathrm{conj}}}{\mathcal{P}_{\mathrm{inc}}} = \frac{\lambda^2}{4\pi} G(\hat{\boldsymbol{r}}), \tag{2.13}$$

where $P_{R,\,\mathrm{conj}}$ corresponds to the power delivered to a conjugate matched receiver.

Note that, through an impedance mismatch factor e_{load}, an alternative metric that generalizes the conjugate-matched effective area of (2.13) can be incorporated. In particular, the absorption cross-section σ_a is defined here as that area which, multiplied by the incident radiation density, gives the power delivered to any arbitrary load attached to the antenna terminals; namely:

$$\sigma_a(\hat{\boldsymbol{r}}, Z) = e_{\mathrm{load}}(Z)\, A(\hat{\boldsymbol{r}}),\ e_{\mathrm{load}}(Z_L) = \frac{4R_L R_A}{|Z_L + Z_A|^2}, \tag{2.14}$$

where $Z_L = R_L + \jmath\, X_L$ and $Z_A = R_A + \jmath\, X_A$ represent the impedance of the receiver device and receiver antenna, respectively.

From (2.14), it can be shown that $\sigma_a(\hat{\boldsymbol{r}}, Z) \leq A(\hat{\boldsymbol{r}})$ (for $\Re\{Z\} \geq 0$) with strict equality when $Z = Z_A^*$.

To summarize, a directional characterization for the radiated and absorbed power was obtained through the antenna gain and effective area. The latter will allow in the following section to build a model for the power received via an unobstructed transmitter-receiver link or free-space link budget.

2.3 Link budget

With the electrical and field perspectives (and their corresponding characterization) of antennas as conductor-air interfaces, a model (known as the Friis equation) can be expressed as a chain of propagation steps starting by the power accepted by the transmit antenna terminals all the way to the power delivered to a matched receiver.

In specific, from (2.12) and (2.13), we can readily show:

$$\begin{aligned} P_{R,\,\mathrm{conj}} &= \overbrace{\frac{P_T}{4\pi r^2}\, G_T(\hat{\boldsymbol{r}}_T)}^{\mathcal{P}_{\mathrm{inc}}}\ A_R(\hat{\boldsymbol{r}}_R), \\ P_{R,\,\mathrm{conj}} &= P_T\, G_T(\hat{\boldsymbol{r}}_T)\, G_R(\hat{\boldsymbol{r}}_R) \left(\frac{\lambda}{4\pi r}\right)^2, \end{aligned} \tag{2.15}$$

where the impact of polarization and impedance mismatch at the receiver have been discarded for the sake of brevity.

On the other hand, if such a mismatch is to be considered it can be included through:

$$P_R = P_T\, G_T(\hat{\boldsymbol{r}}_T)\, G_R(\hat{\boldsymbol{r}}_R) \left(\frac{\lambda}{4\pi r}\right)^2 e_{\text{load}}\, e_{\text{pol}}, \tag{2.16}$$

with e_{load} from (2.14) and $0 \leq e_{\text{pol}} \leq 1$ given by:

$$e_{\text{pol}} = \frac{|\boldsymbol{l}_{\text{e}}(\hat{\boldsymbol{r}}_T) \cdot \boldsymbol{l}_{\text{e}}(\hat{\boldsymbol{r}}_R)|^2}{|\boldsymbol{l}_{\text{e},T}(\hat{\boldsymbol{r}}_T)|^2 |\boldsymbol{l}_{\text{e},R}(\hat{\boldsymbol{r}}_R)|^2}, \tag{2.17}$$

with e_{pol} characterizing the polarization mismatch in terms of the effective length vectors at the transmitter[10] and the receiver side.

[10]– recall that the effective length vector is parallel to the radiated electric field intensity and, thus, determines the polarization of the radiated field.

Chapter 3

Antennas as scatterers

The beginning of the so-called *fundamentals* dealt with the conceptual solution of Maxwell's equations for general geometries in the far-field and, in detail, for radiation from thin half-wave dipoles. Additionally, the picture of antennas as conductor-air interfaces was complemented through the respective electrical and field perspectives, both for transmission and reception.

The current chapter deepens into the alternative view of antennas as objects that scatter fields when exposed to EM radiation from the environment. Recalling Sec. 1.2 on the boundary conditions, the notion of a field appearing as a reaction to external excitation becomes central to such a view.

More specifically, antennas behaving as scatterers are pervasive (in fact all antennas in reception scatter back to the environment at least part of the energy they collect) and, thus, the goal of this chapter is to present a way to characterize their behavior. The latter will allow to predict and control the impact of simple yet useful antennas designed as controllable scatterers.

3.1 The field scattered by an antenna

To recall, the boundary condition (1.29) says that the incident field induces a current at the PEC that, in response, produces a field $\boldsymbol{E}_{\text{reac}}$; effectively annihilating the net tangential component of the electric field at the boundary. Nonetheless, $\boldsymbol{E}_{\text{reac}}$ continues to radiate outside the interface and results into what is called here a scattered field $\boldsymbol{E}_{\text{scat}}$.

Thus, the task of characterizing the field scattered by any antenna could be decoupled into two stages: finding the induced current density and computing the radiated field resulting from such an induced current.

In particular, as per (1.7), (1.11) and (1.12), the scattered field can be given in terms of the linear operator L that acts on the induced surface

current density [6], namely:

$$\boldsymbol{E}_{\text{reac}} := L(\boldsymbol{J}_{\text{reac}}). \tag{3.1}$$

As a result of the linearity of such an operator, multiple decompositions of $\boldsymbol{J}_{\text{reac}}$ (and thus of $\boldsymbol{E}_{\text{reac}}$) could be used to break down the reaction field into easier to determine components and, subsequently, to apply the boundary conditions to solve the scattering problem.

Some analytical decompositions include the so-called natural modes of resonance (NMR) and characteristic modes of resonance (CMR) [6]. Also, the well-known numerical method of moments (MoM) is based on its decomposition in terms of a conveniently chosen set of basis functions.

3.1.1 The structure and antenna decomposition

In what follows, an alternative and more convenient decomposition will be considered instead. More specifically, the field scattered by an antenna can be decomposed into two terms commonly referred to as the *structural* and *antenna* components.

In particular, the structural component is here defined as the scattering response of the antenna (and its close surroundings) when conjugate matched[1] to its port impedance Z_A. Thus, by virtue of such a decomposition, it can be shown [7] that the so-called antenna component results simply related to the reflection coefficient towards the load attached to the antenna, namely through:

$$\begin{gathered}\boldsymbol{E}_{\text{scat}}(Z) = \overbrace{\boldsymbol{E}_{\text{scat}}(Z = Z_A^*)}^{\boldsymbol{E}_{\text{struct}}} - \alpha\, \Gamma(Z)\, \boldsymbol{E}_{\text{ant}}, \\ \alpha = \tfrac{I_{\text{conj}}}{I_{\text{m}}},\ \Gamma(Z) = \tfrac{Z - Z_A^*}{Z + Z_A^*},\end{gathered} \tag{3.2}$$

where Z is the impedance attached to the antenna terminals, I_{conj} the port current in reception when conjugate matched and I_{m} is the terminal current for the transmission situation represented by $\boldsymbol{E}_{\text{ant}}$.

Note that the *antenna* contribution represented via $\boldsymbol{E}_{\text{ant}}$ can be given in terms of the previously introduced radiation vector $\boldsymbol{F}$ for far-field problems as in (1.20). More generally, and of paramount importance for the third part of this thesis, the antenna mode contribution $\boldsymbol{E}_{\text{ant}}$ and the current I_{conj} could both be modeled using the tools introduced in Chapter 2.

On the other hand, as $\boldsymbol{E}_{\text{struct}}$ represents the contribution resulting from resonance modes that are typically not excited through the antenna port[2], the

[1] The structural component can also be referenced to different load conditions.

[2] – e.g. the contribution of the metallic structure of a car-mounted antenna when studying its scattering properties.

structural component is generally more difficult to characterize. Nonetheless, as shown in (3.2), such resonance modes[3] are independent of the loading conditions and, thus, can be computed once and for all.

3.1.2 The half-wave dipole case

At this point it is convenient to consider the case of thin half-wave dipole radiators. Such a geometry is of high relevance for scattering for one particular reason: their single resonance mode.

To be specific, and according to Sec. 3.1.1, the scattering due to the structural component is usually the most difficult to compute due to the multiple modes of resonance that can be induced by the incident radiation.

Nonetheless, in the case of such thin wires, the single resonance mode (approximated to a corresponding sinusoidal current density) is the only one that can be induced regardless of the mode of excitation. As a consequence, the tools of Chapter 2 entirely characterize the scattering operation mode of such antennas.

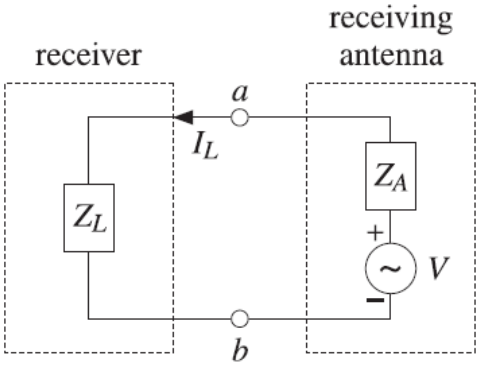

Figure 3.1: Circuit representation of an antenna in reception. $V = \mathcal{E}$. Extract [2], educational use. S. J. Orfanidis © 2016.

In particular, the scattering phenomena can be observed as a cascaded reception-transmission process and be modeled by the receive circuit representation of Fig. 3.1. More specifically, the equivalent source delivers an emf, given in terms of the incident field by

$$\mathcal{E} = \boldsymbol{l}_{\mathrm{e}}(\hat{\boldsymbol{r}}_{\mathrm{inc}}) \cdot \boldsymbol{E}_{\mathrm{inc}}, \tag{2.1}$$

to the internal antenna impedance in series with the external receiver load. In fact, in reception, the power delivered to the antenna impedance Z_A cor-

[3]– and the structural mode contribution to the total scattering for that matter.

responds to power being radiated back to the environment exactly as in transmission (see Fig. 2.1 for reference).

As a consequence, all receiving antennas scatter back to the environment part of the energy they collect and, more importantly, the scattered field is both: determined by the incident one and impacted by the receiver load Z_L.

To conclude, and based on the electric and field perspectives of Chapter 2, the far-zone field scattered by a thin half-wave dipole due to plane-wave excitation characterized by $\boldsymbol{E}_{\text{inc}}$ is given by[4]:

$$\boldsymbol{E}_{\text{scat}}(\boldsymbol{r}_{\text{obs}}) = \boldsymbol{l}_{\text{e}}(\hat{\boldsymbol{r}}_{\text{obs}}) \frac{\jmath\,\eta k}{Z_A + Z_L} \frac{\mathrm{e}^{-\jmath kr}}{4\pi r} \left[\boldsymbol{l}_{\text{e}}(\hat{\boldsymbol{r}}_{\text{inc}}) \cdot \boldsymbol{E}_{\text{inc}}\right], \tag{3.3}$$

where $\boldsymbol{r}_{\text{obs}} = r\,\hat{\boldsymbol{r}}_{\text{obs}}$ (the scattered field observation point) and the phase of $\boldsymbol{E}_{\text{inc}}$ should both be referenced to the scattering dipole. Additionally, recalling the reader, the effective length vector of such a dipole is given by:

$$\boldsymbol{l}_{\text{e}}(\hat{\boldsymbol{r}}) = -\hat{\boldsymbol{\theta}}\,\frac{2}{k}\frac{\cos\left(\frac{\pi}{2}\cos\theta\right)}{\sin\theta}. \tag{2.4}$$

Note that the far-zone scattered field by a dipole of (3.3) exhibits a geometry-specific double directional dependence (namely on $\hat{\boldsymbol{r}}_{\text{inc}}$ and $\hat{\boldsymbol{r}}_{\text{obs}}$). On the hand, its dependence on the observation distance r is conventional for far-field problems.

Thus, some authors [8] have introduced the notion of a distance independent far-zone electric field intensity[5] measure called the far-field pattern function $\breve{\boldsymbol{F}}$ and given by:

$$\breve{\boldsymbol{F}}_{\text{scat}}(\hat{\boldsymbol{r}}_{\text{inc}}, \hat{\boldsymbol{r}}_{\text{obs}}) := \frac{kr}{\mathrm{e}^{-\jmath kr}} \boldsymbol{E}_{\text{scat}}(\hat{\boldsymbol{r}}_{\text{inc}}, \boldsymbol{r}_{\text{obs}}), \tag{3.4}$$

where the double directional and distance dependencies were made explicit for clarity.

The author stresses the difference between the radiation vector (denoted $\boldsymbol{F}$) of Chapter 1 and the far-field pattern function of (3.4). To be specific, such vectorial quantities could be linked to each other as they characterize far-field radiation; although not via a straightforward linear relationship.

Thus, using the definition (3.4), the far-field pattern function for the scattering from such a dipole is:

$$\breve{\boldsymbol{F}}_{\text{scat}}(\hat{\boldsymbol{r}}_{\text{inc}}, \hat{\boldsymbol{r}}_{\text{obs}}) = \jmath\, \boldsymbol{l}_{\text{e}}(\hat{\boldsymbol{r}}_{\text{obs}}) \frac{k^2}{4\pi} \frac{\eta}{Z_A + Z_L} \left[\boldsymbol{l}_{\text{e}}(\hat{\boldsymbol{r}}_{\text{inc}}) \cdot \boldsymbol{E}_{\text{inc}}\right]. \tag{3.5}$$

[4]Note that real dipoles scatter negligibly when open-circuited. However, the expression here does not account for it because of the sinusoidal current approximation.

[5]– much like it was done with the directivity and gain to decouple the distance from the directional dependencies for the radiation density in Sec. 2.2.2.

Note that by setting a purely reactive load at the antenna terminals, i.e. $Z_L = \jmath X_L$, no energy is effectively extracted. Thus, under those circumstances, the fields surrounding the antenna are impacted by its presence but all captured energy is scattered back to the environment[6].

3.2 The total power scattered by an antenna

The previous section expanded on how the field scattered by an antenna can be decomposed into a structural component and an *antenna* component. More importantly, the connection between the latter and the equivalent circuit representation was highlighted as a means of modeling the field scattered by a dipole as a function of the load attached to its terminals. In what follows, a way to quantify the scattering behavior of an antenna in terms of a power-related cross section is introduced.

To begin with, recall that there is a far-field metric describing the capabilities of an antenna to extract and transfer energy from the environment to any attached arbitrary load, namely: the absorption cross section[7] σ_a. Accordingly, the so-called total scattering cross section σ_s describing its capabilities to extract and scatter energy can be defined.

Reminding the reader about the flux vector as a way to quantify the power contained at an infinitesimal surface element dS, the total power scattered by an antenna is given by:

$$P_{\text{scat}}(\hat{\boldsymbol{r}}_{\text{inc}}) := \oint_{S(V)} \boldsymbol{\mathcal{P}}_{\text{scat}}(\hat{\boldsymbol{r}}_{\text{inc}}, \boldsymbol{r}_{\text{obs}}) \cdot \hat{\boldsymbol{n}}\, dS, \tag{3.6}$$

where $\boldsymbol{\mathcal{P}}_{\text{scat}}$ is the flux of the scattered field and $S(V)$ is a closed integration surface containing the antenna. Moreover, in the case of a lossless antenna and medium, $P_{\text{scat}}(\hat{\boldsymbol{r}}_{\text{inc}})$ is independent of $S(V)$ provided it is in the far-field, thus, a sphere can be chosen for mathematical simplicity.

Particularly, based on (2.5) and (3.4), the radiation density $\mathcal{P}_{\text{scat}}$ (and so the flux $\boldsymbol{\mathcal{P}}_{\text{scat}}$) can be expressed in terms of the far-field pattern function as:

$$\boldsymbol{\mathcal{P}}_{\text{scat}}(\hat{\boldsymbol{r}}_{\text{inc}}, \boldsymbol{r}_{\text{obs}}) = \hat{\boldsymbol{r}} \overbrace{\frac{1}{2\eta\, k^2\, r^2} \left| \breve{\boldsymbol{F}}_{\text{scat}}(\hat{\boldsymbol{r}}_{\text{inc}}, \hat{\boldsymbol{r}}_{\text{obs}}) \right|^2}^{\mathcal{P}_{\text{scat}}(\hat{\boldsymbol{r}}_{\text{inc}}, \boldsymbol{r}_{\text{obs}})}. \tag{3.7}$$

To proceed, in the same way as the effective area was defined in Sec. 2.2.2, the total scattering cross section (TSCS) is defined as the ratio of the total

[6] what is convenient for the sake of designing a good controllable scatterer.

[7] recall that σ_a is related to the effective area A through a matching factor (2.14).

scattered power to the radiation density of the incident field of (2.5), i.e. [8]:

$$\sigma_s(\hat{\boldsymbol{r}}_{\text{inc}}) := \frac{P_{\text{scat}}(\hat{\boldsymbol{r}}_{\text{inc}})}{\mathcal{P}_{\text{inc}}} = \frac{1}{k^2|\boldsymbol{E}_{\text{inc}}|^2} \iint\limits_{\Omega(V)} \left|\breve{\boldsymbol{F}}_{\text{scat}}(\hat{\boldsymbol{r}}_{\text{inc}}, \hat{\boldsymbol{r}}_{\text{obs}})\right|^2 d\Omega, \tag{3.8}$$

where the radial symmetry of the flux vector and the spherical nature of V were used to replace the surface integral of (3.6) by an integral over the solid angle Ω [2, 5].

3.2.1 The extinction cross section

By the inclusion of the total scattering cross section σ_s, a metric that quantifies the net withdrawal of an antenna from its surroundings can be simply defined. More specifically, the hence-called extinction cross section σ_t corresponds to that area which multiplied by the incident radiation density quantifies the net power lost by the impinging wave[8]:

$$\sigma_t(\hat{\boldsymbol{r}}_{\text{inc}}, Z) = \sigma_a(\hat{\boldsymbol{r}}_{\text{inc}}, Z) + \sigma_s(\hat{\boldsymbol{r}}_{\text{inc}}, Z). \tag{3.9}$$

Note that, in (3.9), the dependence of all terms on the direction of the incident radiation and the loading condition was made explicit for clarity.

In particular, it might be tempting to think that there is a trade-off between the absorption and total scattering cross sections as a function of the terminal loading Z. Nonetheless, as clear by σ_t being a function of Z, reducing the amount of scattered power (low σ_s) does not necessarily make a good receiving antenna (high σ_a); and vice-versa for a good scatterer.

In order to show that such a trade-off with Z does not indeed exist, one might simply consider the extreme case of a short circuited half-wave dipole ($\sigma_t \neq 0$) versus its open circuit alternative ($\sigma_t = 0$).

3.2.2 The forward scattering theorem

In the current section an important theorem relating the extinction cross section and the field scattered by an antenna is presented.

More specifically, it has been shown in [9] that the extinction cross section of an antenna can be unequivocally determined by a single observation of its scattered field. Moreover, as the antenna must be located right in the line of sight between the source and observation points for it to be applicable, it is known as the forward scattering theorem.

[8]–justifying the apology to its *extinction*.

Following the notation of [8], the forward scattering theorem for an incident field with a single polarization along $\hat{\boldsymbol{p}}_{\text{inc}}$ reads:

$$\sigma_t(\hat{\boldsymbol{r}}_{\text{inc}}) = \frac{4\pi}{k^2}\Im\left\{\frac{\hat{\boldsymbol{p}}_{\text{inc}} \cdot \breve{\boldsymbol{F}}_{\text{scat}}(\hat{\boldsymbol{r}}_{\text{inc}}, \hat{\boldsymbol{r}}_{\text{inc}})}{\hat{\boldsymbol{p}}_{\text{inc}} \cdot \boldsymbol{E}_{\text{inc}}}\right\}, \tag{3.10}$$

where $\Im\{z\}$ refers to the imaginary part of the complex quantity z and $\hat{\boldsymbol{r}}_{\text{obs}}$ is equivalent to $\hat{\boldsymbol{r}}_{\text{inc}}$ given that they both point in the direction *through*[9] the antenna whose scattering is under study.

Plugging in (1.26) into (3.10), the extinction cross section of a dipole for incidence from the horizontal plane ($\theta_{\text{inc}} = \pi/2$) can be shown equivalent to:

$$\sigma_t\big(\theta_{\text{inc}} = \pi/2\big) = \frac{\lambda^2\,\eta}{\pi^2}\,\frac{R_A + R_L}{|Z_A + Z_L|^2}, \tag{3.11}$$

where, recalling the reader, η being the impedance of the medium corresponds to $120\pi\,\Omega$ in the vacuum.

In order to observe how the forward scattering theorem is useful in studying the interaction of σ_s and σ_a, consider Fig. 3.2 where the cross sections of a half-wave dipole[10] are shown under different loading conditions.

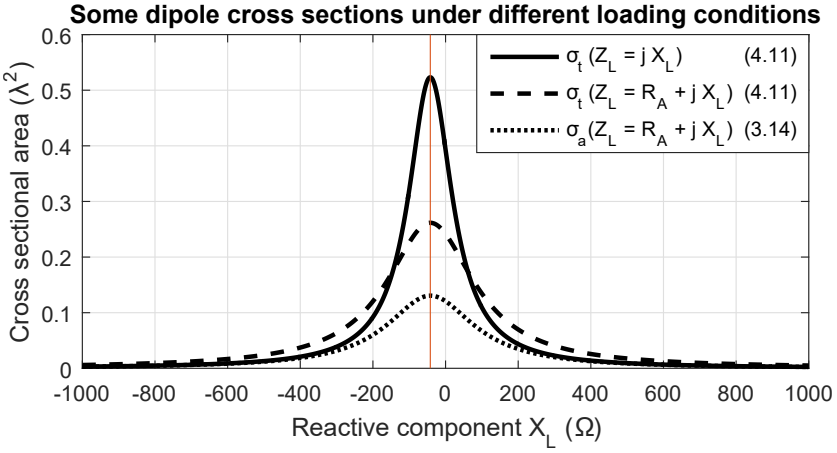

Figure 3.2: Total scattering and absorption cross sections of a dipole under different loading conditions versus the reactive component of Z_L.

Thus, Fig. 3.2 evaluates two loading conditions: the purely reactive one and the case where the $R_L = R_A$; both versus the reactive component of the attached load X_L.

[9] i.e. $\hat{\boldsymbol{r}}_{\text{inc}}$ points inwards whereas $\hat{\boldsymbol{r}}_{\text{obs}}$ points outwards.

[10] – whose antenna impedance Z_A is equivalent to $73 + \jmath\,42\,\Omega$ [5].

Note that the cross section is maximized for $X_L = -42\,\Omega$ (at the red line crossing) in all cases as this value brings the antenna to resonance. Additionally, it is observed that the net power extracted from the wave is maximized in resonance when the load's resistance is zero[11] (continuous curve at the red line crossing).

Nonetheless, the extinction cross section when conjugate matched is reduced to exactly half of the corresponding purely reactive case (dashed vs. continuous curves at the red line crossing).

Finally, through (2.14) and (3.9), it can be shown that $\sigma_a = \sigma_s$ for $R_L = R_A$ regardless of X_L and that, indeed, these are maximized whenever $X_L = -X_A$. A result that is in agreement with the dipole equivalent circuit representation for scattering of Sec. 3.1.2.

3.3 The radar cross section

So far, the characterization of antennas as scatterers has focused on the field scattered by an antenna and on power considerations relating the scattered and absobed energy; both from the perspective of the antenna itself. More specifically, the inclusion of the forward scattering theorem allowed to connect its scattered field and net extracted power in a very keen way.

Nonetheless, a description of the energy captured by a scattering antenna as a secondary source of fields is appropriate at this point. In particular, recall that the scattered field exposes a double directional dependence that is hidden in the total scattering cross section[12].

In the rest of the current chapter, and borrowing on tools used in the radar community to describe *targets*, the radar cross section (RCS) will be adopted as a component of the so-called modified link budget. Such a modified link budget studies the unobstructed transmitter-receiver link solely through a scatterer described in terms of the so-called radar cross section.

To begin with, recall from Sec. 2.2.2 that, the absorption cross section σ_a measures the capture area of an antenna when extracting power from the incident wave for specific loading conditions.

In a similar way, the radar cross section σ_b measures, from the observer's perspective (i.e. direction), the area that a *target* would be required to have if such a target were isotropically scattering the energy captured from its incident field. Thus, the radar cross section is defined as:

$$\sigma_b(\hat{\boldsymbol{r}}_{\text{inc}}, \hat{\boldsymbol{r}}_{\text{obs}}) := \frac{P^{\text{iso}}_{\text{scat}}(\hat{\boldsymbol{r}}_{\text{inc}}, \hat{\boldsymbol{r}}_{\text{obs}})}{\mathcal{P}_{\text{inc}}}, \tag{3.12}$$

[11] i.e. when all energy is scattered back to the environment.

[12] – whose dependence on $\hat{\boldsymbol{r}}_{\text{obs}}$ is hidden due to the integration process (3.8).

where $\mathcal{P}_{\text{inc}}$ is the radiation density of the field incident at the *target* and $P^{\text{iso}}_{\text{scat}}(\hat{\boldsymbol{r}}_{\text{inc}}, \hat{\boldsymbol{r}}_{\text{obs}})$ is, again from the observer's viewpoint, the net power "isotropically" scattered as a reaction by such a target[13]. The latter given by:

$$P^{\text{iso}}_{\text{scat}}(\hat{\boldsymbol{r}}_{\text{inc}}, \hat{\boldsymbol{r}}_{\text{obs}}) := 4\pi r^2\, \mathcal{P}_{\text{scat}}(\hat{\boldsymbol{r}}_{\text{inc}}, \boldsymbol{r}_{\text{obs}}).$$

Expressing the radiation density of the scattered field in terms of the far-field pattern function as in (3.7), $P^{\text{iso}}_{\text{scat}}$ can be shown independent of the observation distance r, which was one reason for introducing it in the first place. Thus, through (3.7) and (3.12), the RCS becomes purely an antenna metric[14] equivalent to:

$$\sigma_b(\hat{\boldsymbol{r}}_{\text{inc}}, \hat{\boldsymbol{r}}_{\text{obs}}) = \frac{\lambda^2}{\pi} \frac{\left|\breve{\boldsymbol{F}}_{\text{scat}}(\hat{\boldsymbol{r}}_{\text{inc}}, \hat{\boldsymbol{r}}_{\text{obs}})\right|^2}{|\boldsymbol{E}_{\text{inc}}|^2}. \tag{3.13}$$

Based on (3.5), for the particular case of a half-wave dipole [10], the radar cross section reads:

$$\sigma_b\big(\theta_{\text{inc}}, \theta_{\text{obs}}\big) = \frac{\lambda^2\, \eta^2}{\pi^3} \frac{\cos^2\left(\frac{\pi}{2}\cos(\theta_{\text{obs}})\right)}{\sin^2(\theta_{\text{obs}})} \frac{1}{\left|Z_A + Z_L\right|^2} \frac{\cos^2\left(\frac{\pi}{2}\cos(\theta_{\text{inc}})\right)}{\sin^2(\theta_{\text{inc}})}. \tag{3.14}$$

Finally, it is important to highlight that the RCS of a resonant dipole ($Z_L = -\jmath\, X_A$) for horizontal incidence and observation (i.e. $\sigma_b \approx\ 0.86\,\lambda^2$) is larger than its TSCS for horizontal incidence (i.e. $\sigma_s \approx\ 0.52\,\lambda^2$).

The latter seemingly counter-intuitive result is a consequence of the fact that $P_{\text{scat}}(\hat{\boldsymbol{r}}_{\text{inc}}) \leq P^{\text{iso}}_{\text{scat}}(\hat{\boldsymbol{r}}_{\text{inc}}, \hat{\boldsymbol{r}}^{\text{max}}_{\text{scat}})$ with $\hat{\boldsymbol{r}}^{\text{max}}_{\text{scat}}$ corresponding to the direction of maximum scattering[15].

Thus, in this case the convenient assumption of isotropic scattering in (3.12) makes it seem as if the target were larger than it actually is. As a matter of fact, σ_b and σ_s meet with equality for isotropic scatterers.

3.4 The modified link budget

As presented before, the definition of the RCS allowed to remove the dependence with the observer's distance and obtain a purely directional metric in the realm of power for the scattering from an antenna.

Particularly, the link sustained through the process of scattering can be decomposed into three stages; one of which is new with respect to the link

[13] note that $P^{\text{iso}}_{\text{scat}}(\hat{\boldsymbol{r}}_{\text{inc}}, \hat{\boldsymbol{r}}_{\text{obs}})$ is only meaningful to the observer as it does not indeed quantify the total power scattered by the *target* whatsoever.

[14] – in the sense that it can be described in terms of a directional pattern.

[15] see the definition of the TSCS in (3.8) to recall on the role of P_{scat}.

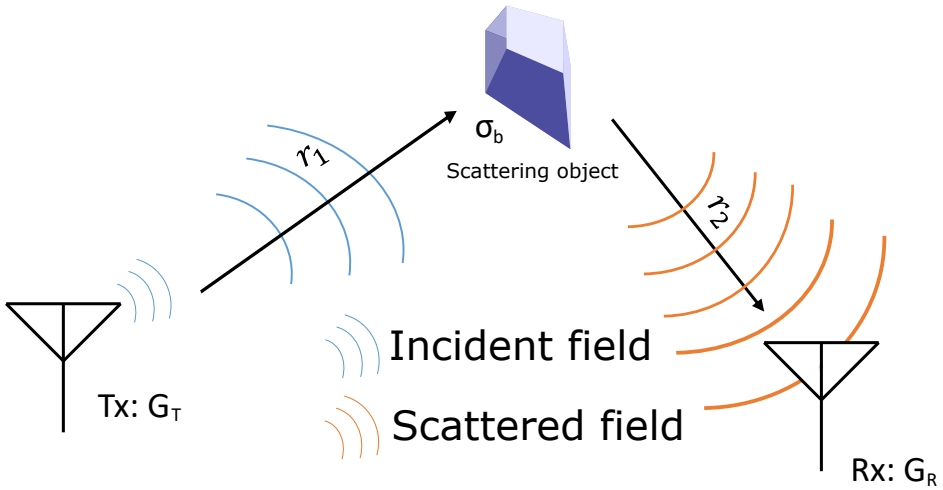

Figure 3.3: Sketch of a transmitter-receiver link through a scatterer as a secondary source and the components of the modified link budget.

budget of Sec. 2.3. One way to introduce the scatterer's impact is by (what can be called) the scattering effective area of the receiving antenna A_R^{scat}, i.e.:

$$A_R^{\text{scat}} := \frac{\sigma_b}{4\pi r^2} A_R, \tag{3.15}$$

where the factor multiplying A_R can be seen as a gain in the radiation density incident to the receiving antenna.

Based on (2.16) and (3.15), the modified link budget can be expressed as:

$$P_R = P_T\, G_T\, G_R \underbrace{\overbrace{\left(\frac{\lambda}{4\pi r_1}\right)^2}^{\text{Free space path loss}} \quad 4\pi \frac{\sigma_b(\hat{\boldsymbol{r}}_{\text{inc}}, \hat{\boldsymbol{r}}_{\text{scat}})}{\lambda^2} \left(\frac{\lambda}{4\pi r_2}\right)^2}_{\text{Effective loss of the scattered link}}, \tag{3.16}$$

with its components as shown in Fig. 3.3 and exposing the double wave-front expansion process in parenthesis.

It must be noted that (3.16) accounts for the power received exclusively through the link presented in Fig. 3.3. Therefore, the contribution of the direct transmitter-to-receiver link should be superimposed in the fields domain by taking into account the impact of the constructive and destructive interference produced by the two different paths. The latter will be expanded in Sec 5.1 dealing with propagation environments in a more general sense.

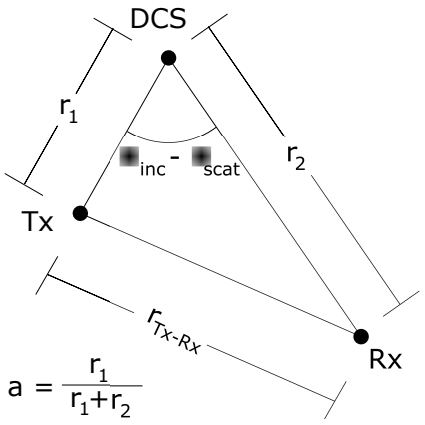

Figure 3.4: Alternative representation of the constitutive components of the modified link budget of (3.17).

An alternative representation

Let us define $r_{\text{TX-RX}}$ as the transmitter-receiver distance and a as a scalar from zero to one given by $a = {}^{r_1}/_{r_1+r_2}$ as shown in Fig. 3.4. Thus, the modified link budget of (3.16) can be re-expressed as:

$$P_R = \overbrace{P_T G_T G_R \left(\frac{\lambda}{4\pi r_{\text{TX-RX}}}\right)^2}^{\text{Direct Tx-Rx path receive power}} \overbrace{\frac{\sigma_b(\hat{\boldsymbol{r}}_{\text{inc}}, \hat{\boldsymbol{r}}_{\text{scat}})}{4\pi r_{\text{TX-RX}}^2} [\, g(a, \hat{\boldsymbol{r}}_{\text{inc}}, \hat{\boldsymbol{r}}_{\text{scat}})]^2}^{\text{Gain with respect to direct Tx-Rx path}} \tag{3.17}$$

where $g(a, \hat{\boldsymbol{r}}_{\text{inc}}, \hat{\boldsymbol{r}}_{\text{obs}})$ is defined for the particular case of purely horizontal propagation as:

$$g(a, \hat{\boldsymbol{r}}_{\text{inc}}, \hat{\boldsymbol{r}}_{\text{scat}}) = \left(\frac{1}{a(1-a)} - 2\Big(1 + \cos(\phi_{\text{inc}} - \phi_{\text{scat}})\Big)\right).$$

From (3.17), the connection to the direct-path link budget is made evident. As can be observed, in order to maintain constant the gain of the relayed link with respect to the direct link, the RCS is required to grow with the square of the distance between the receiver and transmitter. Also, in agreement with (3.16), such an expression shows that the scattering antenna should be placed as close as possible to either the transmitter (a approaching 0) or the receiver (a approaching 1).

Additionally, Fig. 3.5 shows the Contour plot of $|g(a, \hat{\boldsymbol{r}}_{\text{inc}}, \hat{\boldsymbol{r}}_{\text{scat}})|^2$ in dB as given by (3.17). Note that, by setting a very small or large (i.e. a either close to zero or close to one), $g(a, \hat{\boldsymbol{r}}_{\text{inc}}, \hat{\boldsymbol{r}}_{\text{scat}})$ can be made approximately angle independent.

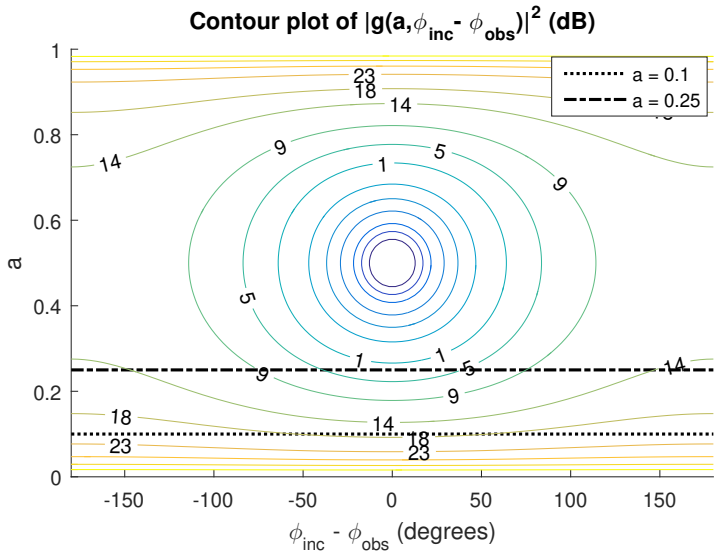

Figure 3.5: Contour plot of $|g(a, \hat{\boldsymbol{r}}_{\text{inc}}, \hat{\boldsymbol{r}}_{\text{scat}})|^2$ in dB.

Finally, even though (3.17) shows a loss with the fourth power of distance, it is implicitly assumed there that both r_1 and r_2 grow with $r_{\text{TX-RX}}$. Nonetheless, as illustrated through (3.16), a distance-related loss of 20 dB per decade with r_1 or r_2 is achieved if the respective-contrary is fixed.

Chapter 4

Antenna arrays

So far, single-port antennas have been studied as conductive bodies with the possibility to resonate and radiate energy to the environment. Additionally, the important property of linearity, resulting into the so-called superposition principle, has been highlighted.

The latter was used to analyze their behavior in transmission, reception and scattering modes. In particular, due to the far-zone approximation, it has also been shown that a directional characterization or *pattern* suffices to completely describe antennas in all such operation modes.

Nonetheless, recall from Chapter 1 that the antenna patterns are related to the spatial Fourier transform of the induced current distribution. Consequently, as single-port antennas are often excited through a single mode of resonance (and therefore exhibit a unique current distribution), no control of their directional properties can be achieved by dynamically loading them[1].

In this chapter, the arrangement of multiple antennas is illustrated as a mean of introducing a control to the overall current distribution and, therefore, to the directional patterns. The linearity of the fields on such antenna currents becomes central to the characterization of antenna arrays in the far-field through the steering vector (also known as array manifold).

To conclude, the existence of EM coupling among the antenna elements is discussed and described through the impedance matrix. Noting that an antenna array can be seen as a multi-port network, the admittance matrix of the loaded array is established by the end of the chapter.

In particular, the linear approximation of such an admittance matrix on the loads is also presented as it is a tool exploited on both of the subsequent *parts* of this document.

[1]– see the RCS of a single dipole of (3.14) as an example.

4.1 The steering vector

Recall that all derived far-field antenna metrics can be traced on their roots to the previously introduced radiation vector; which is given in terms of the source current density by:

$$\boldsymbol{F}(\hat{\boldsymbol{r}}) := \int_V \boldsymbol{J}_0(\boldsymbol{r}')\mathrm{e}^{\jmath\,\boldsymbol{k}\cdot\boldsymbol{r}'}\,d^3\boldsymbol{r}',\ \boldsymbol{k} = k\hat{\boldsymbol{r}}. \tag{1.19}$$

Thus, in the case of an arrangement of multiple identical elements, the array far-field characterization can be entirely realized in terms of the radiation vector. Thus, consider that the current distribution of an array $\boldsymbol{J}(\boldsymbol{r})$ can be decomposed into the sum of a spatially-shifted elementary one, i.e.:

$$\boldsymbol{J}(\boldsymbol{r}) = \sum_{n=1}^{N} I_n\,\boldsymbol{J}_0(\boldsymbol{r}-\boldsymbol{r}_n), \tag{4.1}$$

where N is the number of elements, $\boldsymbol{r}_n$ is the location of the n^{th} element with respect to a common reference, I_n is the input current at the n^{th} element and $\boldsymbol{J}_0(\boldsymbol{r})$ is the (identical) current distribution of the array elementary unit normalized to such an input current.

Subsequently, plugging (4.1) into (1.19), the radiation vector for such an arrangement can be expressed by virtue of the superposition principle as:

$$\boldsymbol{F}(\hat{\boldsymbol{r}}) = \overbrace{\sum_{n=1}^{N} I_n\mathrm{e}^{\jmath\,\boldsymbol{k}\cdot\boldsymbol{r}_n}}^{A(\hat{\boldsymbol{r}})}\ \overbrace{\int_V \boldsymbol{J}_0(\boldsymbol{r}')\mathrm{e}^{\jmath\,\boldsymbol{k}\cdot\boldsymbol{r}'}\,d^3\boldsymbol{r}'}^{\boldsymbol{F}_0(\hat{\boldsymbol{r}})},\ \boldsymbol{k} = k\hat{\boldsymbol{r}}, \tag{4.2}$$

where $A(\hat{\boldsymbol{r}})$ is a direction dependent scalar function known as the array factor.

More specifically, the array factor corresponds to the linear combination of the array input currents $\boldsymbol{I} \in \mathbb{C}^N$ with the so-called steering vector $\tilde{\boldsymbol{a}}(\hat{\boldsymbol{r}})$, namely:

$$\tilde{\boldsymbol{a}}(\hat{\boldsymbol{r}})\big|_n := \mathrm{e}^{\jmath\,k\,\boldsymbol{r}\cdot\boldsymbol{r}_n}. \tag{4.3}$$

Note from (4.3) that, if degrees of freedom exist at $\boldsymbol{I}$ through some parameter $\boldsymbol{x}$, the net radiation vector is explicitly described by:

$$\boldsymbol{F}(\hat{\boldsymbol{r}}|\boldsymbol{x}) = \overbrace{\boldsymbol{I}^{\intercal}(\boldsymbol{x})\,\tilde{\boldsymbol{a}}(\hat{\boldsymbol{r}})}^{A(\hat{\boldsymbol{r}}|\boldsymbol{x})}\ \boldsymbol{F}_0(\hat{\boldsymbol{r}}), \tag{4.4}$$

where it is shown, explicitly, that the directional properties of the array can be dynamically modified if $\boldsymbol{I}$ can be controlled through $\boldsymbol{x}$.

It must be stressed that $\boldsymbol{x}$ could represent any physical quantity that impacts on the input current vector $\boldsymbol{I}$. Nonetheless, in this thesis, $\boldsymbol{x}$ corresponds to electronically controllable loads attached to the antenna ports.

Note also that, in spite of the linearity of the radiation vector on $\boldsymbol{I}$, the input currents are not independent of each other[2] when set in terms of the respective port voltages. Such interdependence is known as mutual coupling and, as detailed in Sec. 4.3, its characterization can be realized in terms of the so-called array impedance matrix.

4.2 The modified length vector

Before deepening into the array impedance matrix, let us consider the impact of arraying multiple antennas on the effective length vector of Sec. 2.1.1.

Reminding the reader of the electrical perspective given to antennas in Chapter 2, the effective length vector works as an interface between circuit quantities and field quantities for both transmission and reception modes.

Thus, the modified length vector is defined here as the array (multi-antenna) extension of the effective length vector over a single direction of polarization, through:

$$\boldsymbol{l}_{\mathrm{m}}^{\mathrm{p}}(\hat{\boldsymbol{r}}) := \tilde{\boldsymbol{a}}(\hat{\boldsymbol{r}})\, l_{\mathrm{e,p}}(\hat{\boldsymbol{r}}), \tag{4.5}$$

where the extra subscript refers to the fact that the polarization of the effective length vector is taken over p. It must be stressed that $\boldsymbol{l}_{\mathrm{m}}^{\mathrm{p}}(\hat{\boldsymbol{r}}) \in \mathbb{C}^N$ (where N is the number of elements) is, thus, the respective modified length vector.

> The modified length vector $\boldsymbol{l}_{\mathrm{m}}^{\mathrm{p}}(\hat{\boldsymbol{r}})$ corresponds to the steering vector as effectively impacted by the pattern of the array elementary unit.

In fact, from (4.2) and the work of Chapter 2, the induced emf *vector* for a single p-polarization array in reception can be expressed as:

$$\boldsymbol{\mathcal{E}} = \boldsymbol{l}_{\mathrm{m}}^{\mathrm{p}}(\hat{\boldsymbol{r}}_{\mathrm{inc}}) E_{\mathrm{inc,p}}. \tag{4.6}$$

Also, the p-component of the net field radiated by such an array can be expressed in terms of the modified length vector as:

$$E_{\mathrm{p}}(\boldsymbol{r}) = -\jmath\, k\eta \frac{\mathrm{e}^{-\jmath kr}}{4\pi r}\, \boldsymbol{I}^{\intercal} \boldsymbol{l}_{\mathrm{m}}^{\mathrm{p}}(\hat{\boldsymbol{r}}), \tag{4.7}$$

[2]– for all transmission, reception and scattering modes.

where $\boldsymbol{I} \in \mathbb{C}^N$ is the vector of input currents to the N antenna terminals.

Observe that, in spite of only characterizing the p-component of the radiated field, the total field can be recovered from (4.7) as long as only a single polarization is required.

4.3 Mutual coupling

Let us now reconsider the linear decomposition of the array current distribution. Recall that, for the input current at the n$^{\text{th}}$ element port referred to as I_n, the expression (4.1):

$$\boldsymbol{J}(\boldsymbol{r}) = \sum_{n=1}^{N} I_n \boldsymbol{J}_0(\boldsymbol{r} - \boldsymbol{r}_n), \tag{4.1}$$

represents the current density as the linear combination of a elementary one.

At this point, recall that the method used in Chapter 1 to study radiation from antennas assumes the source current distribution is known a priori. In practice, nonetheless, there is no real distinction between sources and their reaction on the near surroundings[3]. On the other hand, such reactions become sources of fields depicting the nature of a coupled system that cannot be analyzed independently anymore.

As a consequence, the coefficients $I_n \, \forall \, n$ in (4.1) cannot all be simply fixed without considering the coupling among the antennas themselves. A straightforward way to characterize this dependence is via the impedance matrix that relates the currents and voltages at the array ports [5], as follows.

The array impedance matrix

The array impedance matrix comes from looking at the antenna array as a linear N-port network where voltages and currents can be defined; namely through:

$$\boldsymbol{V} = \boldsymbol{Z}\,\boldsymbol{I}, \tag{4.8}$$

where $\boldsymbol{V} \in \mathbb{C}^N$ and $\boldsymbol{I} \in \mathbb{C}^N$ correspond to the vector of port voltages and currents, respectively. As an example, for a 2-element array, the previous system of equations can be expanded as:

$$\begin{aligned} V_1 &= Z_{1,1}\, I_1 + Z_{1,2}\, I_2, \\ V_2 &= Z_{2,1}\, I_1 + Z_{2,2}\, I_2, \end{aligned}$$

[3] i.e. or neighboring antenna elements for what we are concerned about here.

where $Z_{i,i}$ is known as the self-impedance of the i$^{\text{th}}$ element and $Z_{i,j}$ is known as the mutual-impedance of the j$^{\text{th}}$ element towards the i$^{\text{th}}$ element.

The elements that compose $\boldsymbol{Z}$ can be obtained one by one through the evaluation of specific conditions, e.g. the combination of short and open circuit configurations on the different array elements. Particularly, the induced emf method [5] is widely used as a way to compute the open circuit voltage due to a current at a neighboring element and solve (4.8) for $\boldsymbol{Z}$.

Even more, for the specific case of linear wire radiators, i.e. the ones of interest for the current thesis, analytical expressions have been reported in the literature to compute the components of $\boldsymbol{Z}$ [5].

4.4 Admittance matrix of a loaded array

Recall that the introduced steering vector allows to compute both the radiation vector and the modified length vector of an antenna array. Besides, given that all metrics of Chapters 2 and 3 were based on these quantities, a far-field characterization of the circuit-field interface of arrays in all operation modes is readily available.

One variation with respect to the single antenna case of Chapters 2 and 3 comes from the multidimensional nature of the respective circuit quantities, namely: the antenna port voltage and current vectors. Nonetheless, for the sake of circuit analysis, the single element description holds in the multi-antenna case if the dimensionality of the involved operations is properly accounted for.

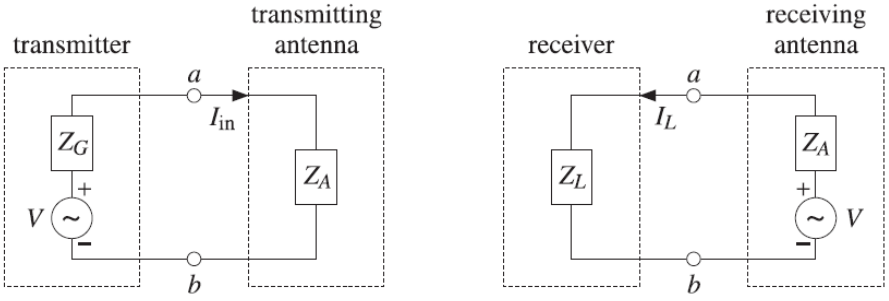

Figure 4.1: Circuit representation of a single antenna in transmission (left) and reception (right) modes.
Extract [2], educational use. S. J. Orfanidis © 2016.

Specifically, consider the circuit representation in Fig. 4.1 (or Fig. 2.1 of Chapter 2). Note that, except for the direction of the loop current, the

only difference in the circuit for both modes is the component to which the voltage source is assumed to belong. In general, denoting by $Z(= Z_L = Z_G)$ the external impedance as seen by the antenna port, the loop current can be generalized by[4]:

$$\boldsymbol{I} = \pm \overbrace{\left(\mathbf{Z}_{\mathrm{A}} + \mathrm{diag}(\boldsymbol{z})\right)^{-1}}^{\boldsymbol{Y}(\boldsymbol{z})} \boldsymbol{V}, \tag{4.9}$$

where $\mathbf{Z}_{\mathrm{A}}$ is the array impedance matrix, $\boldsymbol{V} \in \mathbb{C}^N$ corresponds to the external source for transmission mode ($\boldsymbol{z} = \boldsymbol{z_G} \in \mathbb{C}^N$), $\boldsymbol{V} = \boldsymbol{\mathcal{E}} \in \mathbb{C}^N$ is the induced emf for reception mode ($\boldsymbol{z} = \boldsymbol{z_L} \in \mathbb{C}^N$), $\mathrm{diag}(\boldsymbol{z}) \in \mathbb{C}^{N\times N}$ refers to a diagonal matrix with $\boldsymbol{z}$ on its main diagonal and $\boldsymbol{Y}(\boldsymbol{z}) \in \mathbb{C}^{N\times N}$ is the so-called admittance matrix of the $\boldsymbol{z}$-loaded antenna array.

Note also that $\boldsymbol{I}$, as of (4.9), operates with the + sign on both transmission and reception modes given that the polarization of $\boldsymbol{V}$ accounts for the conventional current directions of Fig. 2.1.

On the other hand, recall from Sec. 3.1.2, that the dipole scattering is characterized as simultaneous reception and transmission. Thus, when studying scattering from an array of dipoles, the fact that the current points on opposite directions for such operation modes needs to be accounted for with the - sign in (4.9).

Admittance matrix approximation

As mentioned, (4.9) allows to fully characterize mutual coupling and the impact of loading antenna arrays in transmission, reception and scattering[5] modes.

More importantly, such an expression exposes their mathematical dependence on the loads characterized through $\boldsymbol{z}$; which correspond to the available degrees of freedom both for ESPAR antennas and digitally controllable scatterers.

As a matter of fact, the inverse dependence of the admittance matrix on $\boldsymbol{z}$ is inconvenient for the optimization of different system metrics; specially with looks at its computational complexity. Thus, the rest of the section introduces a first-order approximation of the system admittance matrix that is given use in the second part of this manuscript.

To begin with, we shall note that $\boldsymbol{Y}(\boldsymbol{x}) = \left(\mathbf{Z}_{\mathrm{A}} + \boldsymbol{X}\right)^{-1}$, with $\boldsymbol{X} := \mathrm{diag}(\boldsymbol{x})$, is dominated by $\mathbf{Z}_{\mathrm{A}}^{-1}$ when $\|\boldsymbol{X}\|_F \ll \|\mathbf{Z}_{\mathrm{A}}\|_F$; with $\|\boldsymbol{Q}\|_F$ standing for the Frobenius norm of matrix $\boldsymbol{Q}$. This can be observed by re-expressing

[4]– already accounting for the multi-antenna nature of the system under consideration.

[5]– at least the *antenna* contribution, see Sec. 3.1.1.

the admittance matrix for non-singular $\mathbf{Z}_\mathrm{A}$ as:

$$\left(\mathbf{Z}_\mathrm{A} + \boldsymbol{X}\right)^{-1} = \underbrace{\left(\mathbb{I}_N + \mathbf{Z}_\mathrm{A}^{-1}\boldsymbol{X}\right)^{-1}}_{\boldsymbol{A}} \mathbf{Z}_\mathrm{A}^{-1},$$

where matrix $\boldsymbol{A} \to \mathbb{I}_N$ for $\|\mathbf{Z}_\mathrm{A}^{-1}\boldsymbol{X}\|_F \to 0$. Even more, matrix $\boldsymbol{A}$ could be approximated via its 1st-order Taylor expansion on $\boldsymbol{X}$ as:

$$\boldsymbol{A} \approx \boldsymbol{A}_1 := \mathbb{I}_N - \mathbf{Z}_\mathrm{A}^{-1}\boldsymbol{X}. \tag{4.10}$$

Moreover, its approximation error can be expressed as:

$$\|\boldsymbol{A} - \boldsymbol{A}_1\|_F = \|\mathbf{Z}_\mathrm{A}^{-1}\boldsymbol{X}\|_F \, \epsilon(\mathbf{Z}_\mathrm{A}^{-1}\boldsymbol{X}), \tag{4.11}$$

where $\epsilon(\boldsymbol{Q})$ is a matrix function converging to zero when $\|\boldsymbol{Q}\|_F$ approaches zero. Thus, the smaller $\|\mathbf{Z}_\mathrm{A}^{-1}\boldsymbol{X}\|_F$ the smaller the approximation error of (4.10).

Hence, when it is the case that the error can be considered small[6], the admittance matrix can be approximated as:

$$\boldsymbol{Y}(\boldsymbol{x}) \approx \mathbf{Z}_\mathrm{A}^{-1} - \mathbf{Z}_\mathrm{A}^{-1}\,\mathrm{diag}(\boldsymbol{x})\,\mathbf{Z}_\mathrm{A}^{-1}, \tag{4.12}$$

from a sufficiently small $\|\mathbf{Z}_\mathrm{A}^{-1}\mathrm{diag}(\boldsymbol{x})\|_F$.

To conclude, the normalized root mean square (RMS) approximation error can be more concretely defined as:

$$\varepsilon_\mathrm{RMS} = \sqrt{\mathbb{E}_{\boldsymbol{x}}\{\varepsilon^2(\boldsymbol{x})\}}, \tag{4.13}$$

where $\varepsilon(\boldsymbol{x})$ is the normalized approximation error is given by:

$$\varepsilon(\boldsymbol{x}) := \frac{\left\| \boldsymbol{Y}(\boldsymbol{x}) - \left(\mathbb{I}_N - \mathbf{Z}_\mathrm{A}^{-1}\,\mathrm{diag}(\boldsymbol{x})\right)\mathbf{Z}_\mathrm{A}^{-1} \right\|_F}{\left\|\boldsymbol{Y}(\boldsymbol{x})\right\|_F},$$

and the expectation of (4.13) is to be evaluated over a distribution of $\boldsymbol{x}$ considered of relevance for the specific problem under consideration.

[6]– which can be seen as a problem-specific consideration.

Chapter 5

Lighting up the conventional signal model

Earlier, the characterization of antennas in transmission, reception and scattering modes was introduced. Additionally, and central to this work, the construction of multi-antenna *architectures* as means of adding controllability to their directional behavior was also presented.

Before allowing ourselves to complete the picture of the much anticipated link-level system model, an overview of the role played by the propagation environment is required. More specifically, the link budgets of Chapter 2 and Chapter 3 represent the free-space propagation case. In order to characterize more realistic environments, the phenomena known as large scale and small scale fading must be conceptually reviewed.

Likewise, the roots of small scale fading as essentially directional will be exposed to show why multi-antenna architectures make sense and, more importantly, how the control of their directional properties come into play in ESPAR and digitally controllable scatterers. As a preamble, multi-antenna architectures become particularly attractive when considering them in relation to multi-path propagation[1] in order to convey more information and robustness to the link.

Subsequently, the so-called geometry-based channel models characterizing the environment from the antenna perspective will be presented. The chapter closes with the link-level system model in terms of the derived antenna and channel metrics.

[1] initially considered detrimental as it is the leading cause of small-scale fading.

5.1 The wireless environment

It must be stressed that the characterization of wireless environments is a vast topic in itself. Nonetheless, as this project lies essentially on the devices these interact with, this section will briefly introduce the most relevant environmental phenomena: namely, large and small scale fading.

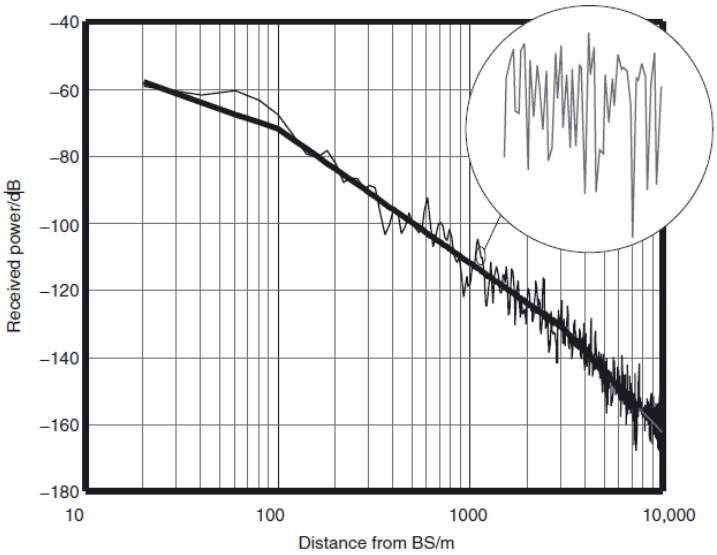

Figure 5.1: Received power vs. distance showing the large scale (thick curve) and small scale (magnified curve) fading phenomena [11].

5.1.1 Large scale fading

Relying on the notion of far-field propagation of Chapter 1, the phenomenon of large scale fading will be introduced in what follows. More specifically, large scale fading is a phenomenological description of intricate macroscopic interactions (relative to λ) and, therefore, it is motivated by the difficulty of modeling realistic propagation environments, e.g. Fig. 5.1.

For simplicity, consider the radiation from an isotropic source of fields. Thus, based on (2.8) and Fig. 5.2, it can be seen that its radiation density decreases as a result of the wavefront expansion with the propagation distance. Hence, as evidenced through the free-space link budget[2] of (2.16), the received power decays with the square of the propagation distance in the absence of obstacles.

[2]– as well as its modified version of Sec. 3.4 for scattering problems.

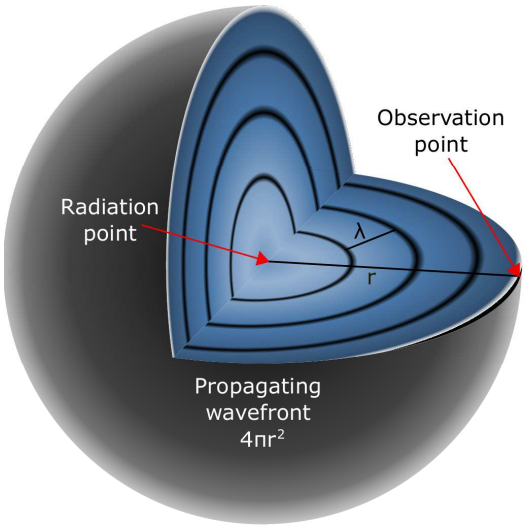

Figure 5.2: Free-space wavefront expansion with the propagation distance.

Nonetheless, large blockages between the location of radiation and observation cause the net receive power to fall, on the distance, with an exponent larger than two. As a result, the generalized link budget reads:

$$P_R = P_T\, G_T(\hat{\boldsymbol{r}}_T)\, G_R(\hat{\boldsymbol{r}}_R) \overbrace{\left(\frac{\beta(\lambda)}{r^{\alpha}}\right)}^{L(r)}, \tag{5.1}$$

where β is a function of the operation wavelength, α is known as the path loss exponent and the matching coefficients of (2.16) have been removed for simplicity of presentation. In general $\alpha \geq 2$, although smaller values have also been observed in very specific conditions such as tunnels and canyons.

As a matter of fact, the *path loss* function $L(r)$ in (5.1) is often characterized through a log-normally distributed random variable [11], i.e.

$$L_{dB}(r) = \beta_{dB} - 10\,\alpha \log_{10}(r) + X,\;\; X \sim N(0, \sigma^2_{\text{LS}}), \tag{5.2}$$

whose variance can be experimentally established. In particular, extensive measurement campaigns characterizing α, β and σ^2_{LS} over a wide range of propagation environments have been conducted.

The log-normally distributed random variable in (5.2) is commonly explained by the chained large-scale interactions with the environment and the central limit theorem on the logarithmic representation of the received power.

Finally note that, in order to account for large scale fading on scattering mode as of Sec. 3.4, the double wavefront expansion of (3.16) should be replaced by two path loss factors as the one in (5.1).

5.1.2 Small scale fading

Small scale fading, on the other hand, refers to the rapid phase-related fluctuations in the received power with the distance (see Fig. 5.1). Such a phenomenon is explained by the existence of multiple interactions of the radiated fields with the environment, as *perceived* by the observer.

More specifically, the radiation process can be seen (via the geometrical-optics approximation) as rays that emanate from the transmitter and pervade its space around. Subsequently, in the presence of a densely populated environment, such rays interact with obstacles through reflection, diffraction, transmission and scattering, among others [11]. As a consequence, the surrounding space is filled by such multiple propagating waves.

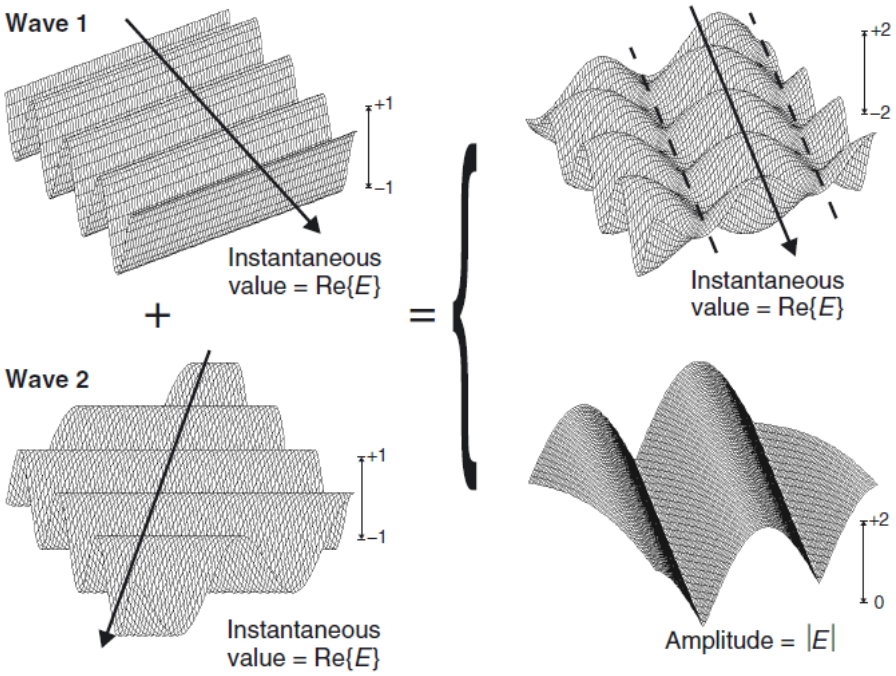

Figure 5.3: Total field resulting from two propagating waves to expose the small scale fading phenomenon. Extract [11], educational use.

Consider the total field resulting from two propagating waves in Fig. 5.3. Note that, if only one wave is present, the field's strength (magnitude) is almost constant over small displacements; i.e. it decreases monotonically with $1/r$ as shown in (1.20) for far-field radiation. Nonetheless, when considering the interference of both waves at the bottom-right of Fig. 5.3, the resulting field is identically zero at some wavelength-apart locations of space.

Therefore, the small-scale appellation is justified on that such interactions are observed in the sub-wavelength scale. Moreover, in light of the sought directional controllability, it can be seen how eliminating the contribution from one direction of incidence in the previous example would be beneficial.

In order to characterize such a phenomenon, consider that the induced emf for an antenna in reception is, thus, given by (2.1) and the superposition principle:

$$\mathcal{E} = \sum_{k=1}^{K} \boldsymbol{l}_{\mathrm{e}}(\hat{\boldsymbol{r}}_{\mathrm{inc},k}) \cdot \boldsymbol{E}_{\mathrm{inc},k}, \tag{5.3}$$

where K is the number of incident waves (or rays under under the geometrical-optics approximation) and $\boldsymbol{l}_{\mathrm{e}}(\hat{\boldsymbol{r}}_{\mathrm{inc}})$ is the effective length vector of such a receiving antenna.

Let us now contemplate an isotropic antenna able to sense the resulting field with no direction of preference. Moreover, consider an environment with multiple polarization-matched incident waves, which results from multiple interactions with the space surrounding the antenna. Under those circumstances, the induced emf reduces to:

$$\mathcal{E} = l_{\mathrm{e}}^{\mathrm{p}} \sum_{k=1}^{K} E_{\mathrm{inc},k}^{\mathrm{p}},$$

where the superscript p refers to the component along the polarization direction. Noting that the components $E_{\mathrm{inc},k}^{\mathrm{p}}$ can be linearly related to the field radiated by the transmitting antenna through $E_{\mathrm{inc},k}^{\mathrm{p}} = \tilde{h}_k E_{\mathrm{rad}}^{\mathrm{p}}$, the previous expression can be written as:

$$\mathcal{E} = l_{\mathrm{e}}^{\mathrm{p}}\, E_{\mathrm{rad}}^{\mathrm{p}} \sum_{k=1}^{K} \tilde{h}_k. \tag{5.4}$$

By virtue of the central limit theorem, the sum channel coefficient h can be statistically characterized in terms of independent Gaussian random variables for its real and imaginary components:

$$h = \sum_{k=1}^{K} \tilde{h}_k = X + \jmath Y, \tag{5.5}$$

where $X \sim N(\mu_X, \sigma_{\mathrm{SS}}^2)$, $Y \sim N(\mu_Y, \sigma_{\mathrm{SS}}^2)$ and $h_{\mathrm{LOS}} = \mu_X + \jmath\, \mu_Y$ is the so-called line-of-sight component.

More specifically, the environment is said to be non-line-of-sight (NLOS) when the K incident waves tend to cancel each other ($h_{\mathrm{LOS}} = 0$). In addition,

when that is the case, $|h|$ corresponds to a Rayleigh distributed random variable whose only parameter is σ^2_{SS}. On the other hand, when $h_{\text{LOS}} \neq 0$, the environment is known as line-of-sight (LOS) and $|h|$ is Rice distributed.

5.2 The signal model

Having considered the dependence of the channel coefficient h with distance, the link-level system model for general environments will now be presented.

Particularly, note that the previously introduced channel coefficient is impacted both by large scale and small scale fading. Nonetheless, in the conventional link between a pair of transmitting and receiving antennas, the large scale dependence with distance is often accounted for in the channel coefficients as done in (5.4).

5.2.1 SISO

Thus, based on (2.2) and (5.3), the single input single output (SISO) model for the voltage developed at the receiver load, as a function of the generator's voltage at the transmitter side, can be written shortly as:

$$v_L = \overbrace{\sum_{k=1}^{K} \tilde{h}_k \, l_{\text{e}}^{\text{p}}(\hat{\boldsymbol{r}}_{\text{inc},k}) \, l_{\text{e}}^{\text{p}}(\hat{\boldsymbol{r}}_{\text{rad},k})}^{h} \; v_G, \tag{5.6}$$

where, again, K refers to the number of rays that compose the transmitter-receiver link and $\tilde{h}_k$ are the coefficients that represent all environmental interactions as well as proportionality constants for the k^{th} ray (e.g. accounting for impedance and polarization mismatch). Moreover, $l_{\text{e}}^{\text{p}}(\hat{\boldsymbol{r}})$ is the component of the effective length vector along the single direction of polarization for the identical transmitter and receiver antennas[3].

Noting the dimensionless nature of h, the paradigmatic SISO signal model can be expressed as:

$$y = hs + n, \tag{5.7}$$

with s and y referred to as the input and output (dimensionless) *signals* and n representing the background noise.

Additionally, the average signal to noise ratio (SNR) ρ is defined as:

$$\rho := \mathbb{E}\left\{ \frac{|hs|^2}{|n|^2} \,\middle|\, h \right\} = |h|^2 \, \frac{E_S}{N_0}, \tag{5.8}$$

[3]In the case of dual-polarized antennas the representation becomes slightly more intricate, specially for the multi-antenna case that follows.

where $E_S = \mathbb{E}\{|s|^2\}$ is known as the signal energy and $N_0 = \mathbb{E}\{|n|^2\}$ is the energy of the additive white Gaussian noise (AWGN).

Therefore, relying on the linearity property so emphasized since Chapter 1, the precise input-output relationship has been revealed on grounds of electromagnetism.

Particularly, following the same process, the SISO model in (5.7) will be extended to the multi-antenna scenario and controllable scattering in the next section and second part of the current manuscript, respectively.

5.2.2 MIMO

To begin with, recall that the use of dynamically tunable loads is proposed in this work as a mean of controlling the directional properties of antennas.

Reminding the reader about Sec. 4.2, the field radiated by an antenna array can be expressed in terms of the modified length vector $\boldsymbol{l}_{\mathrm{m}}^{\mathrm{p}}(\hat{\boldsymbol{r}})$ and the current vector. At the same time, the induced emf vector at a receiving antenna array can be expressed in terms of $\boldsymbol{l}_{\mathrm{m}}^{\mathrm{p}}(\hat{\boldsymbol{r}})$ and the incident field.

Therefore, relying on Sec. 5.2.1, the SISO system model can be readily extended to the (identical transmitter-receiver) multi-antenna scenario as:

$$\boldsymbol{V}_L = diag(\boldsymbol{z_L})\, \boldsymbol{Y}(\boldsymbol{z_L}) \sum_{k=1}^{K} \tilde{h}_k\, \boldsymbol{l}_{\mathrm{m}}^{\mathrm{p}}(\hat{\boldsymbol{r}}_{\mathrm{inc},k}) \left[\boldsymbol{l}_{\mathrm{m}}^{\mathrm{p}}(\hat{\boldsymbol{r}}_{\mathrm{rad},k})\right]^{\intercal} \boldsymbol{Y}(\boldsymbol{z_G})\, \boldsymbol{V}_G, \tag{5.9}$$

where $\boldsymbol{V}_G$ and $\boldsymbol{V}_L \in \mathbb{C}^N$ are the generator (input) and load (output) voltage vectors, $\boldsymbol{z_G}$ and $\boldsymbol{z_L} \in \mathbb{C}^N$ are the generator and receiver load vectors, $\boldsymbol{l}_{\mathrm{m}}^{\mathrm{p}}(\hat{\boldsymbol{r}})$ are the p-polarized modified length vectors of Sec. 4.2, and $\boldsymbol{Y}(\boldsymbol{z})$ is the admittance matrix for a loaded array of Sec. 4.4.

> Although (5.9) characterizes mutual coupling through the admittance matrix, this is only exhaustive for antennas with a single mode of resonance [12]; such as the thin dipoles considered in this project.

In particular, for arbitrary element geometries, the impact of coupling must be also accounted for via the so-called embedded antenna patterns[4] [13]. More specifically, the embedded antenna patterns alter the effective length vector in (4.5) and, therefore, the modified length vector $\boldsymbol{l}_{\mathrm{m}}^{\mathrm{p}}(\hat{\boldsymbol{r}})$.

Noting the transmit-receive symmetry of (5.9), and assuming isotropic antennas for the transmitting and receiving ends[5], the previous expression can

[4]– these account for modes of resonance that are not naturally excited through the feeding port and, thus, are not characterized via the conventional antenna pattern.

[5]– reducing the modified length vector to the steering vector, see (4.5).

be rewritten to account for different transmitter and receiver arrays through:

$$\boldsymbol{V}_L = diag(\boldsymbol{z_L})\,\boldsymbol{Y}_R(\boldsymbol{z_L})\overbrace{\sum_{k=1}^{K}\tilde{h}_k\,\tilde{\boldsymbol{a}}_R(\hat{\boldsymbol{r}}_{\mathrm{inc},k})\,\tilde{\boldsymbol{a}}_T^{\mathrm{H}}(-\hat{\boldsymbol{r}}_{\mathrm{rad},k})}^{\boldsymbol{H}}\,\boldsymbol{Y}_T(\boldsymbol{z_G})\,\boldsymbol{V}_G, \tag{5.10}$$

where $\boldsymbol{V}_L \in \mathbb{C}^{N_R}$, $\boldsymbol{V}_G \in \mathbb{C}^{N_T}$, the subscripts R and T indicate that such quantities are related to the receiver and transmitter arrays, $\tilde{\boldsymbol{a}}(\hat{\boldsymbol{r}})$ is the array steering vector, and $\boldsymbol{H} \in \mathbb{C}^{N_R \times N_T}$ is the MIMO channel matrix in terms of its geometry-based decomposition with N_R and N_T elements at the receiver and transmitter sides, respectively.

Additionally, the directions of radiation $\hat{\boldsymbol{r}}_{\mathrm{rad},k}$ have been flipped in (5.10) to write the steering vector in conventional Hermitian notation; see (4.3).

> Observe that, $\tilde{\boldsymbol{h}} \in \mathbb{C}^K$ is arbitrarily defined as it accounts for phenomenological environmental interactions, making it invariant up to a constant scalar multiplication. As a consequence, without loss of generality, uninformative constant scalar factors can be absorbed by it.

Thus, if mutual coupling is further neglected ($\boldsymbol{Z}_A = z_A\,\mathbb{I}_{N\times N}$), the expression for isotropic antennas gives the well known MIMO signal model[6]:

$$\boldsymbol{y} = \boldsymbol{H}\boldsymbol{s} + \boldsymbol{n}, \tag{5.11}$$

where $\boldsymbol{s} \in \mathbb{C}^{N_T}$ is the input vector and $\boldsymbol{y}, \boldsymbol{n} \in \mathbb{C}^{N_R}$ are the output and additive white Gaussian noise (AWGN) vectors at the receiver side.

Finally, the system signal to noise ratio (SNR) is defined as:

$$\rho := \mathbb{E}\left\{ \frac{|\boldsymbol{H}\boldsymbol{s}|^2}{|\boldsymbol{n}|^2} \,\middle|\, \boldsymbol{H} \right\} = \|\boldsymbol{H}\|_F^2\,\frac{E_S}{N_R\,N_T\,N_0}, \tag{5.12}$$

where the uncorrelated input vector $\boldsymbol{s}$ is conventionally normalized to the number of transmitter elements, i.e.

$$\mathbb{E}\{\boldsymbol{s}\boldsymbol{s}^{\mathrm{H}}\} = \frac{E_S}{N_T}\,\mathbb{I}_{N_T\times N_T},$$

the covariance of the AWGN vector is $\mathbb{E}\{\boldsymbol{n}\boldsymbol{n}^{\mathrm{H}}\} = N_0\,\mathbb{I}_{N_R\times N_R}$ and $\|\boldsymbol{H}\|_F^2$ stands for the square Frobenius norm of the channel matrix.

[6]– although (5.11) was derived assuming arrays of isotropic antennas, it is still valid for arbitrary geometries by replacing the steering vectors with the modified length vectors as in (5.9). However, the impact of $\boldsymbol{z_G}$ and $\boldsymbol{z_L}$ is not accounted for in (5.11).

Part II

The ESPAR antenna

Chapter 6

Introduction

The first part of the current manuscript presented the fundamentals on electromagnetism in order to reveal the roots of the well-known multiple-input multiple-output system model. In the second part, the focus is placed on a particular transceiver architecture; the so-called Electronically Steerable Parasitic Array Radiator antenna.

To begin with, ESPAR can be seen as a re-configurable antenna architecture whose directional properties can be dynamically modified. Notably, it has brought attention owing to its compactness and cost compared to conventional multiple antenna architectures; prominently due to its single radio frequency (RF) front-end. In fact, the principle under which it operates was proposed by Harrington [14] around four decades ago. Nevertheless, it gained significant attention since the advent of multiple antenna systems when Ohira and Gyoda [15, 16] named it in the early 2000s.

More specifically, ESPAR consists in the arrangement of multiple closely-spaced radiating elements all of which, except for one, are provided solely with controllable reactive loads. The fundamental reason for compactly spacing the elements is the interest in feeding them via mutual coupling (justifying their *passive* or *parasitic* denomination); as opposed to conventional systems where multiple RF front-ends are assumed to be available. Thus, such an architecture requires only one of the array elements, so-called active element, to be fed by a complete RF front end [14].

In spite of its conception as a re-configurable antenna, the multi-element structure of ESPAR was later-on shown capable of achieving spatial multiplexing over the so-called beam-space domain [17]. More specifically, spatial streams are realized by encoding information onto a set of beams or patterns through the parasitic loads; thus referred to as beam-space modulation. However, because of its single RF front-end, a single observation of the fields can be obtained at a time in reception. The latter makes ESPAR an inherently

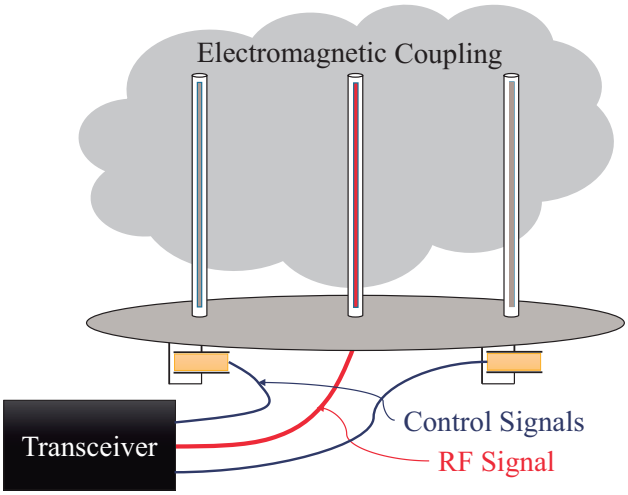

Figure 6.1: A pictorial representation of a 3 element monopole-based ESPAR. Active and parasitic elements in red and gray, respectively.

asymmetric device for spatial multiplexing[1].

Although multiple-active multiple-passive (MAMP) variants of ESPAR can be found in the literature [18, 19], this work concentrates on the initial proposal with a single RF front-end. Moreover, the use of reactive loads is adhered to, based on the need to control the induced parasitic currents while keeping a high radiation efficiency.

One key aspect of study in the current project is the computational complexity associated to the problem of reactance optimization. Particularly, the indirect observability of the passive elements through the active element manifests itself via a non-linear dependence on the controllable loads. The latter does not lend itself to exploiting the many existing linear techniques of conventional arrays and, more importantly, it results in the increase of such a computational complexity.

Finally, given that model-based optimization techniques require the availability of indirectly observable parameters, the problem of parameter estimation has also received particular attention. More specifically, the array impedance matrix and the channel to every element are such unknown and challenging to estimate parameters.

[1] i.e. given that information might be conveyed via several *tunable* loads but only retrieved through a single RF front-end.

State of the art

In its early beginnings, Harrington advocated the use of the ESPAR concept with the purpose of beam-reconfigurability in mind [14], with other authors extending its applications beyond that one in the years to follow.

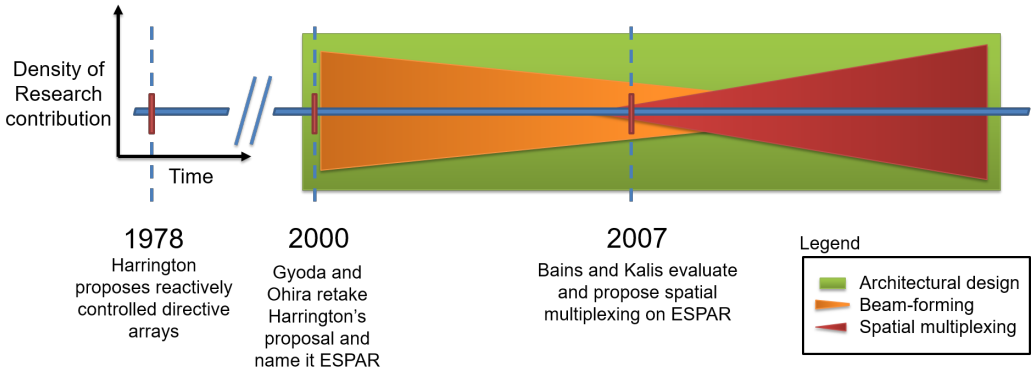

Figure 6.2: A rough representation of ESPAR in the research.

Hence, from the early 2000s, there has been considerable research interest on the benefits of ESPAR calling for its compactness and reduced cost. In particular, active research on architectural considerations led to the refinement of the monopole based architecture by Ojiro, Schlub *et al.* [20][21], the further miniaturization by Liu, Gu *et al.* [22][23][24] and the planar instead of bulky architecture by Luther, Ouyang, *et al.* [25][26][27][28]; although most of the focus in the research community relies on the use of a dipole-based architecture (with the exception of the antenna community).

Since the beginning of the last decade, a significant effort has been devoted to the problem of finding the reactance loadings that achieve beam/null-forming based on availability of either a target direction or a training sequence towards which the receive signal is correlated. The latter is proposed through the use of different reactance optimization methods such as: a Hamiltonian approach [29], a sequential perturbation algorithm [30], a stochastic for cross-correlation coefficient maximization (MCCC) [31][32], a genetic algorithm [33], among others proposed by Ohira *et al.*.

Additionally, the use of the Simultaneous Perturbation Stochastic Approximation (SPSA) method was proposed by Barousis *et al.* [34][35]; calling particular attention due to its complexity-performance trade-off when considering the non-linearity of ESPAR.

Nonetheless, the hype for beam-forming on ESPAR seemed to decline around 2008 in favor of the already much appealing topic of spatial multiplexing. The latter could be naturally explained by an effort of researchers

to leverage, via ESPAR, a better performance-cost relation with respect to conventional multi-RF front-end architectures.

In this regard, since 2007, more researchers were seemingly inspired by spatial multiplexing as result of two publications: one from Bains *et al.* [36] showing a similar capacity for an ESPAR and a conventional array, and another publication from Kalis *et al.* [17] proposing a technique to spatially multiplex Q-PSK symbols on ESPAR through the so-called beam-space modulation.

Subsequently, Bains proposed the implementation of a virtually rotating ESPAR for spatial de-multiplexing at the receiver side [37]. Later on, Alrabadi proposed the decomposition of the far-field pattern into a quasi-orthogonal basis [38] in order to excite certain transmission modes by the appropriate setting of the reactive loads for M-PSK modulation [39].

Afterwards, the use of fully complex (unlike the purely reactive) loads was proposed by Han *et al.* in order to achieve 16-QAM beam-space modulation [40]. Furthermore, Barousis *et al.* proposed an alternative pattern decomposition using the well-known Gram-Schmidt method [41] and, Vasileiou *et al.*, an adaptive channel-based decomposition [42]. The latter in order to better condition the problem of achievable-rate maximization. Additionally, Ryu, Lee *et al.* have proposed the use of ESPAR on multicarrier (OFDM) transmissions for spatial-frequency multiplexing [43][44].

It must be highlighted that, apart from beamforming and spatial multiplexing, alternative applications have also been proposed for ESPAR. In particular, a tremendous amount of work has been done on localization and direction of arrival (DOA) estimation.

More specifically, Ohira *et al.* worked on what was called the Reactance Domain MUltiple SIgnal Classification (RD-MUSIC) algorithm [45] and even shown experimental results obtained in a controlled environment (anechoic chamber) [46, 47]. Moreover, they also suggested an ESPAR architecture to implement the DOA estimation via a rotational invariant technique (ESPRIT) [48].

Apart from them, Qian proposed the use of compressed sensing techniques with the same goal in mind [49, 50]. More recently, Rzymowski, Plotka *et al.* [51, 52, 53] have experimentally demonstrated Received Signal Strength (RSS-based) DOA estimation; therefore avoiding the need to rely on phase information.

What's more, some security-enhancing applications that exploit its low cost and pattern adaptability have been suggested in the literature.

An overview of some of the most significant contributions, and categorized according to the discussed work directions in chronological order, can be found in Appendix G.

Chapter 7

System model

We will now redirect our attention to the mathematical description of ESPAR as a particular conductor-air interfacing device.

First recall that, as a result of the reciprocity principle, such a description can be realized either in transmission or reception. In particular, and for reasons of convenience, the characterization of ESPAR will be carried out in transmission in what follows.

Thus, the current chapter begins by introducing the architecture considered throughout this work. Subsequently, in light of the intrinsic reliance of ESPAR on mutual coupling, relevant impedance-matching aspects are given consideration before heading to the actual model derivation.

The chapter ends with the anticipated system model in terms of the so-called equivalent weight vector[1]. In fact, the linear approximation of such an equivalent weight vector as a function of the reactive loads will also be presented. The latter, as it plays a fundamental role in the low computational complexity algorithms introduced of Chapter 8.

7.1 The considered architecture

As aforementioned, a reactively-loaded variant of the single RF front-end ESPAR will be considered throughout this work. Moreover, as also stressed along the *Fundamentals* part, the architecture is based on thin half-wave dipoles for the multiple reasons exposed there.

Recall the role of mutual coupling as the inherent feeding mechanism of parasitic elements in ESPAR. Also, recall that mutual coupling is particularly strong in the near vicinity of antennas, a region for which an intuition has not been built along this document.

[1] in relation to the weighting or beam-forming vector in the array processing literature.

Nonetheless, dealing with vertically-oriented thin dipoles, we might as well expect a rotational symmetry of the fields along the azimuth for a fixed elevation angle (ϕ and θ in Fig. 1.4, respectively).

In fact, the mutual impedance between two $\hat{\boldsymbol{z}}$-oriented dipoles centered on the $z = 0$ plane [2, 5] is shown in Fig. 7.1. In fact, their mutual coupling is independent of ϕ and, more importantly, depends only on their separation distance.

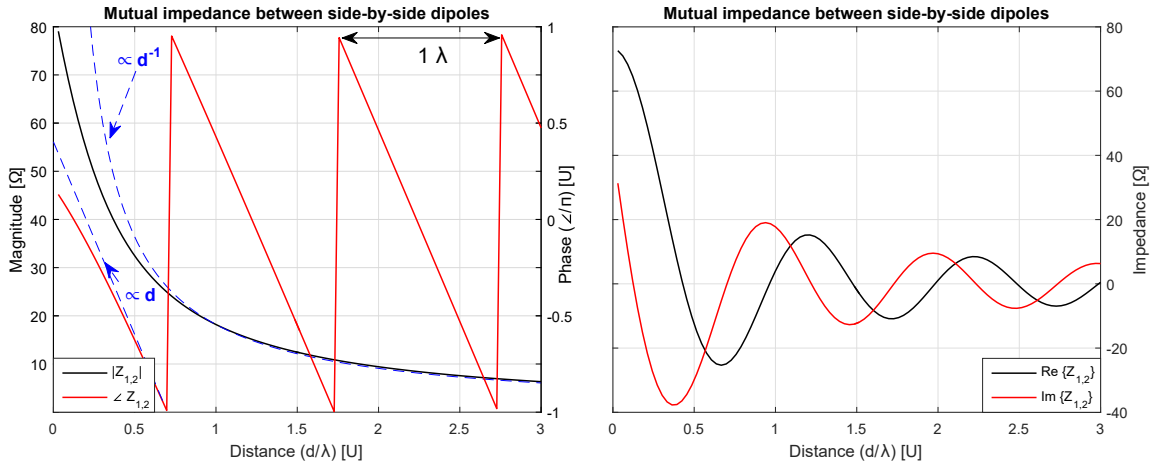

Figure 7.1: Mutual coupling between side-by-side half-wave dipoles versus inter-element distance, through magnitude-phase (left plot) and real-imaginary (right plot) representations.

Note, through the magnitude-phase representation on the left plot of Fig. 7.1, that the phase of the impedance *rotates* 2π for every displacement of λ and, additionally, its magnitude falls with $\sim d^{-1}$ for $d \gtrapprox \lambda/2$, which corresponds to the limit of the far-field region for a half-wave dipole[2].

It is hinted, from Fig. 7.1, that parasitic elements should be as close as possible to the active element to increase energy transfer (recalling that the mutual impedance corresponds to a trans-impedance). Thus, the most natural architecture for a dipole-based ESPAR (and the one that has been considered the most in the literature) corresponds to a uniform circular array of parasitic elements with the active element in its center.

The uniform circular array (UCA)

Let us now introduce formally the architecture under consideration. In particular, the uniform circular array is able to exploit the omni-directional prop-

[2]– such a behavior represents, in fact, far-field propagation as conveyed by the far-zone approximation of the Green function, see (1.16).

erties of wire radiators by allowing to steer, with relative *fairness*, towards any direction in the horizontal plane; as explained by its highly rotationally-symmetric structure. Moreover, as aforementioned, compactness is desirable as it allows to more-evenly distribute energy among array elements.

Nonetheless, as it was stressed in Sec. 5.2.2, mutual coupling is only partially-characterized by the impedance matrix if different modes of resonance may be excited through coupling[3]. In fact, for realistic (i.e. not infinitesimally-thin) dipoles, such considerations become pertinent below a certain distance of separation.

Particularly, as supported on other grounds such as spatial correlation of the fields [54] and angular resolution[4], an UCA radius of $R = \lambda/4$ is assumed.

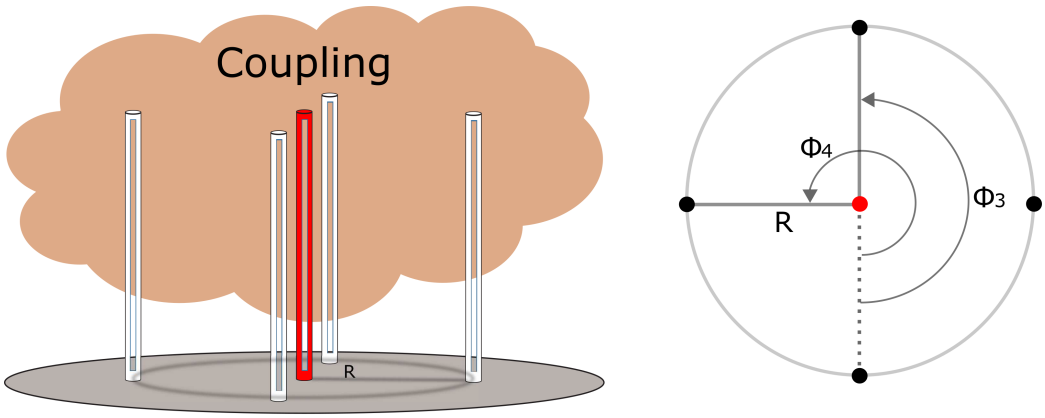

Figure 7.2: Side view (left) and top view (right) of the N=5 element ESPAR architecture with the circular arrangement considered in the current work. The central element corresponds to the active one and $R = \lambda/4$ to the UCA radius.

More specifically, the architecture of Fig. 7.2 with $N = 5$ elements is the one considered the most in this work. Additionally, changing N will always mean modifying the number and relative location of the parasitic elements (in order to preserve UCA's *uniformity*).

Finally, in connection with the characterization of arrays of Chapter 4, the steering vector for the architecture of Fig. 7.2 is given by:

$$\tilde{\boldsymbol{a}}(\hat{\boldsymbol{r}})\big|_i = \begin{cases} 1, & i = 1 \\ \exp\left(\jmath \frac{2\pi}{\lambda} R \sin(\theta)\cos(\phi - \phi_i)\right), & i \neq 1 \end{cases} \tag{7.1}$$

[3]– i.e. if the shape of the elementary current distribution is modified by compactness.
[4]the more compact the array the broader its main beam from Sec. 1.1.

where $\phi_i \ \forall i = 1, 2, \ldots, N-1$ is the azimuth location of the i$^{\text{th}}$ element in the horizontal plane and, additionally, ϕ and θ are defined with respect to the spherical coordinate system of Fig. 1.4 in Chapter 1.

7.2 Matching considerations

Coming back to ESPAR's reliance on mutual coupling, the focus is now aimed at the impact of modifying the parasitic loads on the impedance mismatch.

To begin, consider an ESPAR in transmission as a mean of determining its input impedance. Particularly, by input impedance it is referred to the impedance measured at the active element port for a set of parasitic loads.

> Note that $\boldsymbol{z}$ is defined in (4.9) as the impedance seen by the array ports. As a result, in the case of ESPAR, $\boldsymbol{z}$ accounts for the generator and parasitic elements impedance through their respective array indices.

To be specific, the ESPAR input impedance can be computed through Thevenin's theorem setting $\boldsymbol{V} = \hat{\boldsymbol{u}}_1 \, v$, where v is an ideal voltage source at the active element[5] (whose series impedance $\boldsymbol{z}|_1$ is consequently zero), with $\hat{\boldsymbol{u}}_1 \in \mathbb{R}^N$ being:

$$\hat{\boldsymbol{u}}_1 := \left[1, 0, \ldots, 0\right]^{\intercal}. \tag{7.2}$$

Therefore, the input impedance of ESPAR is given by the source voltage over the induced current at the active element, namely:

$$z_A(\boldsymbol{x}) := \frac{v}{\hat{\boldsymbol{u}}_1^{\intercal} \boldsymbol{I}} = \frac{1}{\left[\hat{\boldsymbol{u}}_1^{\intercal} \, \boldsymbol{Y}(\boldsymbol{z}) \, \hat{\boldsymbol{u}}_1\right]}, \ \boldsymbol{z} = \jmath \begin{bmatrix} 0 \\ \boldsymbol{x} \end{bmatrix}; \tag{7.3}$$

showing that, as a result of mutual coupling, its input impedance depends on the reactive load vector $\boldsymbol{x}$.

As a matter of fact, one implication of (7.3) is that the total power extracted by the antenna is a function of the reactive loads **for a fixed source voltage**. Additionally, as a mean of ensuring maximum power transfer to the antenna, it is commonly assumed the availability of an adaptive circuit [55, 56] enforcing conjugate matching; i.e. $z_G = z_A^*$ where z_G is the source impedance.

It is conventional to express the transmit power as the square norm of the input signal. Thus, in order to express all directional and energy dependencies on $\boldsymbol{x}$ in the very same factor, the so-called equivalent weight (or beam-forming) vector will be introduced in what follows.

[5]– by convention, in this work, the first vector component indexes the active element.

7.3 The equivalent weight vector

Let us begin by considering an $N\times 1$ multiple-input-single-output (MISO) system such as the one of Sec. 5.2.2.

More specifically, the equivalent weight vector can be derived from (5.10) by noticing that isotropic and omni-directional (i.e. as in dipoles) radiation are equivalent conditions if restricted to horizontal propagation.

Therefore, the system model for a dipole receiver and dipole-based ESPAR transmitter can be written directly in terms of the steering vector as:

$$v_L = \frac{z_L}{z_L + z_{\text{dip}}} \overbrace{\sum_{k=1}^{K} \tilde{h}_k \, \tilde{\boldsymbol{a}}_T^{\text{H}}(-\hat{\boldsymbol{r}}_{\text{rad},k})}^{\boldsymbol{h}^{\text{H}}} \boldsymbol{Y}(\boldsymbol{z}_G)\, \boldsymbol{V}_G,$$

where z_L and z_{dip} are the receiver and dipole impedance, $\boldsymbol{h} \in \mathbb{C}^N$ is the channel vector from every element at the transmitter array to the single dipole receiver, $\boldsymbol{V}_G \in \mathbb{C}^N$ is the source voltage vector, $\boldsymbol{z}_G \in \mathbb{C}^N$ the source impedance vector and horizontal propagation is assumed.

Moreover, absorbing constant scalar factors into $\tilde{h}_k$ and setting $\boldsymbol{V}_G = \hat{\boldsymbol{u}}_1\, v$ as done in Sec. 7.2, the previous model can be re-expressed shortly as:

$$v_L = \boldsymbol{h}^{\text{H}} \boldsymbol{Y}(\boldsymbol{z_G})\, \hat{\boldsymbol{u}}_1\, v, \tag{7.4}$$

where it must be stressed that the source generator is not ideal (i.e. its impedance $\boldsymbol{z}_G|_1 = z_G$ is different from $0\,\Omega$).

Note that, for the particular case of ESPAR, $\boldsymbol{z}_G$ represents the impedance seen by all (active and parasitic) elements in the array. Thus, $\boldsymbol{Y}(\boldsymbol{z_G})$ does not only depend on the reactive load vector $\boldsymbol{x} \in \mathbb{R}^{N-1}$ but, on the other hand, it also depends on the generator's impedance z_G (i.e. as $\boldsymbol{z_G}|_1 = z_G$).

Nonetheless, in order to decouple the impact of z_G from $\boldsymbol{Y}(\boldsymbol{z_G})$, the Woodbury matrix identity (also known as matrix inverse lemma) can be used on (4.9), by noticing $\boldsymbol{z_G} = \boldsymbol{z} + \hat{\boldsymbol{u}}_1\, z_G$, to show that:

$$\boldsymbol{Y}(\boldsymbol{z} + \hat{\boldsymbol{u}}_1\, z_G) = \boldsymbol{Y}(\boldsymbol{z})\, \frac{z_A(\boldsymbol{x})}{z_G + z_A(\boldsymbol{x})},\ \boldsymbol{z} = \jmath \begin{bmatrix} 0 \\ \boldsymbol{x} \end{bmatrix}, \tag{7.5}$$

where $z_A(\boldsymbol{x})$ is the input impedance of (7.3) as a function of $\boldsymbol{x} \in \mathbb{R}^{N-1}$.

Additionally, recall from Sec. 7.2, that the power extracted by the source is not constant with respect to $\boldsymbol{x}$. Consequently, as a mean of fixing the transmit power with the square signal norm $|s|^2$, a load-dependent compensation factor is applied to the source, namely:

$$v(\boldsymbol{x}) = \sqrt{\Re\{z_A(\boldsymbol{x}) + z_G\}}\, s, \tag{7.6}$$

where s is the dimensionless transmit signal.

By the inclusion of (7.5) and (7.6) into (7.4) under the conjugate-matched assumption of Sec. 7.2, the input-output signal model for ESPAR in transmission can be written as:

$$y = \boldsymbol{h}^{\mathrm{H}} \overbrace{\left[\frac{1}{\sqrt{\Re\{\hat{\boldsymbol{u}}_1^{\intercal}\boldsymbol{Y}(\boldsymbol{z})\,\hat{\boldsymbol{u}}_1\}}}\boldsymbol{Y}(\boldsymbol{z})\,\hat{\boldsymbol{u}}_1\right]}^{\boldsymbol{w}(\boldsymbol{x})} s + n,\ \boldsymbol{z} = \jmath\begin{bmatrix}0\\ \boldsymbol{x}\end{bmatrix}, \tag{7.7}$$

with s and y referring to the input and output (dimensionless) *signals* and n representing the background noise.

Consequently, the equivalent weight vector in (7.7) is explicitly defined in terms of the array impedance matrix $\mathbf{Z}_{\mathrm{ESPAR}}$ as:

$$\boldsymbol{w}(\boldsymbol{x}) := \frac{1}{\sqrt{\Re\{\hat{\boldsymbol{u}}_1^{\intercal}(\mathbf{Z}_{\mathrm{ESPAR}}+\boldsymbol{X})^{-1}\hat{\boldsymbol{u}}_1\}}}(\mathbf{Z}_{\mathrm{ESPAR}}+\boldsymbol{X})^{-1}\hat{\boldsymbol{u}}_1, \tag{7.8}$$

where $\hat{\boldsymbol{u}}_1 \in \mathbb{R}^N$ is the unit-norm vector of (7.2) and $\boldsymbol{X} \in \mathbb{C}^{N\times N}$ is a matrix with the $N-1$ parasitic load values in its main diagonal, i.e.:

$$\hat{\boldsymbol{u}}_1 := \begin{bmatrix}1\\0\\\vdots\\0\end{bmatrix},\ \boldsymbol{X} := \mathrm{diag}\left(\jmath\begin{bmatrix}0\\\boldsymbol{x}\end{bmatrix}\right) = \begin{bmatrix}0 & 0 & \dots & 0\\ 0 & \jmath x_1 & \dots & 0\\ \vdots & \vdots & \ddots & 0\\ 0 & 0 & 0 & \jmath x_{N-1}\end{bmatrix} \tag{7.9}$$

Additionally, the average signal to noise ratio (SNR) ρ is defined as:

$$\rho := \mathbb{E}\left\{\frac{|\boldsymbol{h}^{\mathrm{H}}\boldsymbol{w}s|^2}{|n|^2}\,\middle|\,\boldsymbol{h}\right\} = \boldsymbol{w}^{\mathrm{H}}\boldsymbol{h}\boldsymbol{h}^{\mathrm{H}}\boldsymbol{w}\,\frac{E_S}{N_0}, \tag{7.10}$$

where $E_S = \mathbb{E}\{|s|^2\}$ is the signal energy and $N_0 = \mathbb{E}\{|n|^2\}$ is the energy of the additive white Gaussian noise (AWGN).

To conclude, note that the inverse of $\mathbf{Z}_{\mathrm{ESPAR}} + \boldsymbol{X}$ (i.e. the system admittance matrix) entirely determines the behavior of $\boldsymbol{w}$ as a function of $\boldsymbol{x} \in \mathbb{R}^{N-1}$ in (7.8).

As a matter of fact, the non-linear behavior of the equivalent weight vector on $\boldsymbol{x}$ and its reliance on $\left(\mathbf{Z}_{\mathrm{ESPAR}} + \boldsymbol{X}\right)^{-1}$ motivate the study of its approximation based on Sec. 4.4. Consequently, $\boldsymbol{w}$ will be revised in what follows by taking a closer look at the interaction of $\mathbf{Z}_{\mathrm{ESPAR}}$ and $\boldsymbol{X}$.

Linear approximation of the equivalent weight vector

Recall from Sec. 4.4, that the admittance matrix can be approximated as a function of $\boldsymbol{x}$ by:

$$\boldsymbol{Y}(\boldsymbol{x}) = \left(\mathbf{Z}_{\mathrm{A}} + \mathrm{diag}(\boldsymbol{x})\right)^{-1} \approx \mathbf{Z}_{\mathrm{A}}^{-1} - \mathbf{Z}_{\mathrm{A}}^{-1}\,\mathrm{diag}(\boldsymbol{x})\,\mathbf{Z}_{\mathrm{A}}^{-1}, \tag{4.12}$$

where $\boldsymbol{x} \in \mathbb{C}^N$ is the impedance seen by every array port and the approximation error can be quantified through:

$$\varepsilon_{\mathrm{RMS}} = \sqrt{\mathbb{E}_{\boldsymbol{x}}\left\{ \frac{\left\| \boldsymbol{Y}(\boldsymbol{x}) - \left(\mathbb{I}_N - \mathbf{Z}_{\mathrm{A}}^{-1}\,\mathrm{diag}(\boldsymbol{x})\right)\mathbf{Z}_{\mathrm{A}}^{-1} \right\|_F^2}{\left\| \boldsymbol{Y}(\boldsymbol{x}) \right\|_F^2} \right\}}. \tag{4.13}$$

It is argued in Sec. 4.4 that $\varepsilon_{\mathrm{RMS}}$ is related to the square Frobenius norm of $\mathbf{Z}_{\mathrm{A}}^{-1}\,\mathrm{diag}(\boldsymbol{x})$. In fact, as proved in Appendix A, such a norm is directly proportional to the norm of the vector $\boldsymbol{x}$ for the circularly symmetric architecture under consideration. As a consequence, the approximation error could be constrained by fixing the norm of the reactive load vector.

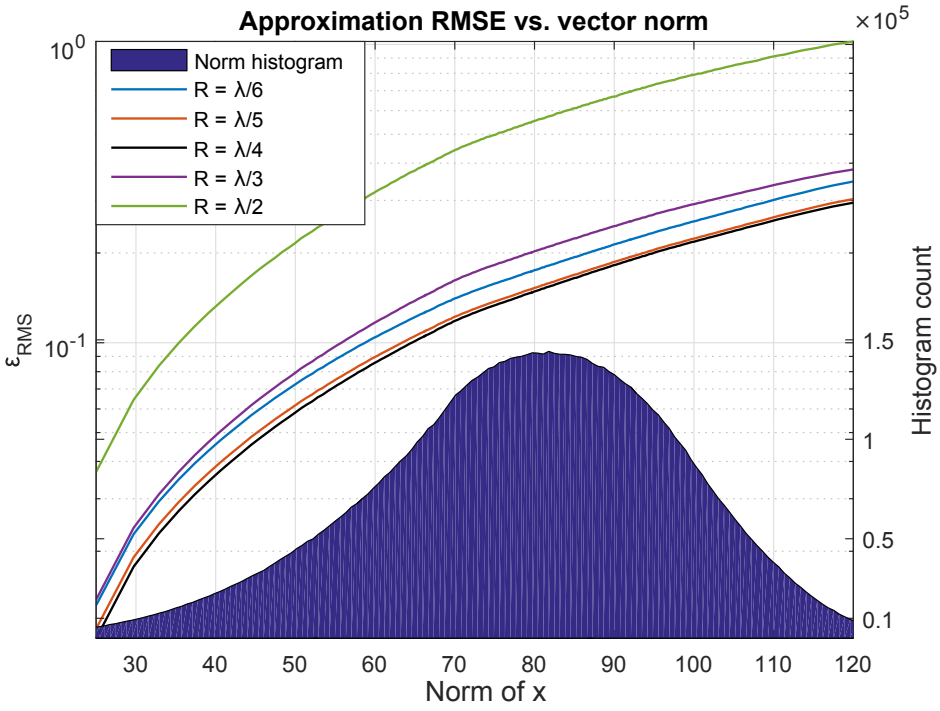

Figure 7.3: Root means square approximation error of the ESPAR admittance matrix vs. norm of $\boldsymbol{x}$ for different values of R (see Fig. 7.2). Histogram of $|\boldsymbol{x}|$ shown in blue for reference.

In particular, Fig. 7.3 shows the approximation error versus the norm of $\boldsymbol{x}$ for different values of the UCA radius. The evaluation set of $\boldsymbol{x}$ was drawn from a component-wise independent, identically and uniformly distributed random vector $\mathrm{U}(-70, 70)$ whose norm distribution is shown in blue.

Observe that the approximation error is minimum for $R = \lambda/4$ among all considered values for the radius. Additionally, as aforementioned, it is observed that the approximation error is monotonically reduced with the norm of $\boldsymbol{x}$.

Returning to the linearization of interest, observe in (7.8) that $\boldsymbol{w}$ is both aligned to $(\mathbf{Z}_{\mathrm{ESPAR}} + \boldsymbol{X})^{-1}\hat{\boldsymbol{u}}_1$ and inversely proportional to a square root factor that depends on $\boldsymbol{x}$. Additionally, it turns out that such a square root factor depends exclusively on the first component of the admittance matrix but, also, it keeps the orientation of $\boldsymbol{w}$ unchanged; suggesting a higher error tolerance than $(\mathbf{Z}_{\mathrm{ESPAR}} + \boldsymbol{X})^{-1}\hat{\boldsymbol{u}}_1$ for beam-forming problems.

Consequently, the equivalent weight vector in (7.8) is approximated as:

$$\boldsymbol{w} \approx \frac{1}{\sqrt{\Re\{\hat{\boldsymbol{u}}_1^{\intercal}\mathbf{Z}_{\mathrm{ESPAR}}^{-1}\hat{\boldsymbol{u}}_1\}}}\left(\mathbb{I}_N - \mathbf{Z}_{\mathrm{ESPAR}}^{-1}\boldsymbol{X}\right)\mathbf{Z}_{\mathrm{ESPAR}}^{-1}\hat{\boldsymbol{u}}_1, \tag{7.11}$$

where $\sqrt{\Re\{\hat{\boldsymbol{u}}_1^{\intercal}(\mathbf{Z}_{\mathrm{ESPAR}} + \boldsymbol{X})^{-1}\hat{\boldsymbol{u}}_1\}}$ has been approximated via an order zero Taylor expansion, i.e. by taking the first term of (4.12).

By reordering and substituting variables, (7.11) can be expressed as:

$$\boldsymbol{w}(\boldsymbol{x}) \approx \boldsymbol{a}_{\mathrm{ap}} + \boldsymbol{B}_{\mathrm{ap}}\,\boldsymbol{x}, \tag{7.12}$$

where the relation between $\boldsymbol{X} \in \mathbb{C}^{N\times N}$ and $\boldsymbol{x} \in \mathbb{R}^{N-1}$ in (7.9) was used. Furthermore, vector $\boldsymbol{a}_{\mathrm{ap}} \in \mathbb{C}^N$ and matrix $\boldsymbol{B}_{\mathrm{ap}} \in \mathbb{C}^{N\times(N-1)}$ are given by:

$$\boldsymbol{a}_{\mathrm{ap}} := \frac{1}{\sqrt{\Re\{\hat{\boldsymbol{u}}_1^{\intercal}\mathbf{Z}_{\mathrm{ESPAR}}^{-1}\hat{\boldsymbol{u}}_1\}}}\,\mathbf{Z}_{\mathrm{ESPAR}}^{-1}\,\hat{\boldsymbol{u}}_1,$$

$$\boldsymbol{B}_{\mathrm{ap}} := -\jmath\,\frac{1}{\sqrt{\Re\{\hat{\boldsymbol{u}}_1^{\intercal}\mathbf{Z}_{\mathrm{ESPAR}}^{-1}\hat{\boldsymbol{u}}_1\}}}\,\mathbf{Z}_{\mathrm{ESPAR}}^{-1}\,\mathrm{diag}\big(\mathbf{Z}_{\mathrm{ESPAR}}^{-1}\hat{\boldsymbol{u}}_1\big)\boldsymbol{T},$$

where $\boldsymbol{T} \in \mathbb{R}^{N\times(N-1)}$ is a matrix extracting the last $N-1$ columns from the matrix on its left.

Therefore, the approximation (7.12) suggests that $\boldsymbol{w}$ approaches a complex valued vector affine function of the reactive load vector $\boldsymbol{x} \in \mathbb{R}^{N-1}$ under a condition on $\|\boldsymbol{x}\|$, namely the one required to keep $\varepsilon_{\mathrm{RMS}}$ *low*[6].

[6]Loosely speaking, *low* is relative to the performance of the algorithm to be presented later, whose operation depends on such a linearity.

Chapter 8

ESPAR as a reconfigurable antenna

The previous chapter introduced the system model of ESPAR through the so-called equivalent weight vector. In addition, the linear approximation of the equivalent weight vector was presented.

This chapter deals with the use of ESPAR as a re-configurable antenna. By *re-configurable antenna* it is meant that the radiation properties of ESPAR are modified based on channel conditions but, in a sense, the antenna array is observed as a conventional single port radiator, unlike Chapter 9 where spatial multiplexing was studied.

In what follows, two different approaches are considered: a computationally complex stochastic optimization and a low-complexity convex optimization. The former is based on the non-linear equivalent weight vector derived in Sec. 7.3 unlike the latter, which is based on its presented linear approximation. As it is often the case, these optimization methods exhibit a complexity-performance trade-off deserving attention.

The chapter concludes by presenting how to deal with the unavailability of channel state information (CSI) and impedance matrix information. Notably, the strategy varies with the considered optimization method. In particular, the least-mean-square and recursive-least-square methods are proposed to solve the low-complexity convex optimization variant, without the need of explicitly estimating the CSI and impedance matrix themselves. In what follows, it will be referred to as *genie-aided* for a receiver provided with perfect CSI and impedance matrix information.

8.1 Reactive load optimization

Given the system model of (7.7), coherent combination of the per-element receive signals can be realized through the set of reactive loads $\boldsymbol{x}$, namely by conjugate matching $\boldsymbol{w}(\boldsymbol{x})$ to the CSI in $\boldsymbol{h}$.

Note that there is no need to apply a constraint on the norm of $\boldsymbol{w}(\boldsymbol{x})$ given that, in the current work, only passive (i.e. reactive) parasitic loads are considered. Consequently, the goal of achieving coherent combination (also called spatial adaptation) can be expressed as the optimization problem:

$$\begin{aligned} \max_{\boldsymbol{x}} \quad & \left|[\boldsymbol{w}(\boldsymbol{x})]^{\mathrm{H}}\boldsymbol{h}\right|^2 \\ \text{s.t.} \quad & \Im\{\boldsymbol{x}\} = \mathbf{o}, \end{aligned} \tag{8.1}$$

with $\boldsymbol{w}(\boldsymbol{x})$ from (7.8) and referring to $\boldsymbol{x} \in \mathbb{R}^{N-1}$ as the set of reactive loads.

In what follows the aforementioned methods to solve (8.1) are introduced.

8.1.1 SPSA-based optimization

As studied by Ohira *et al.* in [32] and by Barousis *et al.* in [19], a good alternative in terms of its relatively fast convergence and resilience against multi-modality in the cost function is the SPSA method (standing for Simultaneous Perturbation Stochastic Approximation).

More specifically, SPSA can be considered a stochastic gradient descent algorithm. Unlike other methods, what it does is to calculate the approximation of the cost function gradient[1] at a location updated according to a Bernoulli distributed random vector (also called *perturbation*).

Being an iterative minimization algorithm, SPSA is able to approach a local minimum with barely two evaluations of the cost function per step, regardless of the number of optimization variables. For the specific implementation details, the reader is referred to [19, 32].

In order to solve (8.1), the following cost function was proposed in [57]:

$$L(\boldsymbol{x}) = 1 - \frac{|\boldsymbol{w}^{\mathrm{H}}(\boldsymbol{x})\,\boldsymbol{h}|}{\|\boldsymbol{w}(\boldsymbol{x})\|\|\boldsymbol{h}\|}, \tag{8.2}$$

where the dependency of $\boldsymbol{w}$ on $\boldsymbol{x}$ was made explicit for clarity.

In (8.2), perfect CSI (i.e. $\boldsymbol{h}$) and the impedance matrix $\mathbf{Z}_{\mathrm{ESPAR}}$ are assumed to be known (or to be previously estimated during a training phase) and the double vertical bars represent the common ℓ^2 norm to make sure the second term lies within -1 and 1.

[1] Technically, it is calculating the direction of a secant line, but it is referred to as *gradient* because the step size used for the secant line computation simulates the smoothing of the cost function.

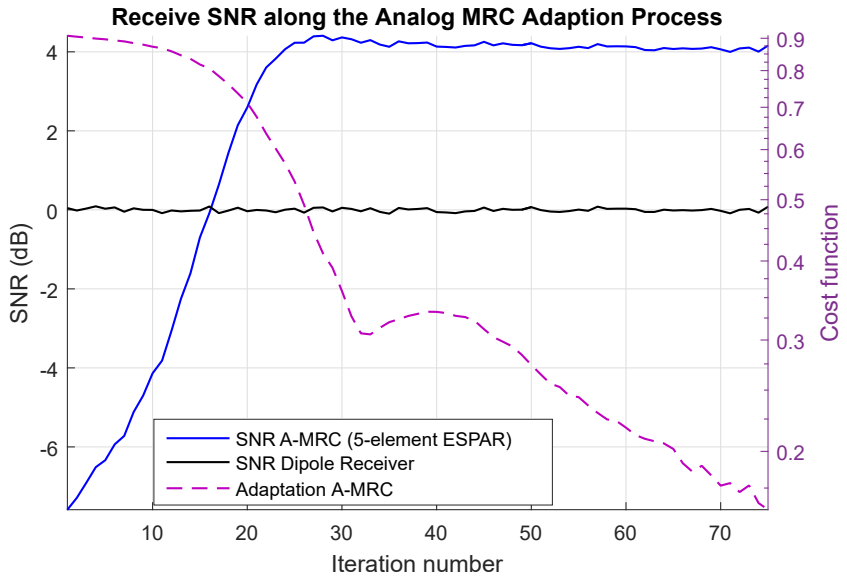

Figure 8.1: Adaptation of SPSA on a single channel realization (single dipole equivalent SNR computation for the same channel shown for comparison).

Particularly, Fig. 8.1 shows the performance of the SPSA algorithm for the cost function in (8.2) on a specific channel realization. The used SPSA parameters are given by (following the notation of [19]):

$$\begin{aligned} \beta(m) &= 100 \exp\left(-{}^{m}/_{25}\right) \\ \tau(n) &= 400 \exp\left(-{}^{n}/_{25}\right) \\ M_{\mathtt{opt}} = 40,\ \text{tot-iters} &= 40,\ \text{tol} = 1 \times 10^{-6}, \end{aligned} \tag{8.3}$$

As observed in Fig 8.1, the resulting SNR improvement using SPSA corresponds to several decibels with respect to a single dipole receiver for the evaluated channel realization.

It must be stressed that, in Fig 8.1, the iteration number refers to the outermost loop, each of them, containing 40 local iterations as shown in (8.3). Thus, with the considered SPSA parameters, a worst-case of around 3×10^3 evaluations of the cost function are required to solve (8.1).

8.1.2 Low complexity optimization

Based on the linearized equivalent weight vector of Sec. 7.3, the problem of coherently combining the incident waves can be expressed having in mind the signal model in (7.7). In fact, as such a linear approximation is valid under a

sufficiently low ε, a convex constraint on the norm of $\boldsymbol{x}$ shall be incorporated into the considered optimization problem to keep ε under control.

Particularly, the latter can be readily achieved based on the discussion of Sec. 7.3 and the equality in (A.3) as:

$$\begin{aligned} \boldsymbol{x}^* := \arg\max_{\boldsymbol{x}} \quad & \left|(\boldsymbol{a}_{\text{ap}} + \boldsymbol{B}_{\text{ap}}\,\boldsymbol{x})^{\text{H}}\boldsymbol{h}\right|^2 \\ \text{s.t.} \quad & \boldsymbol{x}^{\intercal}\boldsymbol{x} \leq c^2, \end{aligned} \tag{8.4}$$

where c is a constraint on the norm of $\boldsymbol{x}$ to be determined based on the algorithm's linearization error tolerance.

It should be highlighted that, although alternative formulations to (8.4) can be more appropriate to account for implementation constraints[2], the selected problem is regarded as more relevant for the model linearization under consideration.

In particular, the quadratic cost function in (8.4) implies that its solution is contained within the boundaries of the constraint, which is directly related to the approximation error as given by (4.11) and (4.13) when constrained to the conventional ℓ_2 norm.

As such, the optimization problem of (8.4) is convex and can be analytically solved by the method of Lagrange multipliers along the Karush-Kuhn-Tucker (KKT) conditions. Let us denote its Lagrangian by:

$$\mathcal{L}(\boldsymbol{x}) = \left|(\boldsymbol{a}_{\text{ap}} + \boldsymbol{B}_{\text{ap}}\,\boldsymbol{x})^{\text{H}}\boldsymbol{h}\right|^2 + \mu\,(c^2 - \boldsymbol{x}^{\intercal}\boldsymbol{x}), \tag{8.5}$$

where $\mu \in \mathbb{R}$ is the multiplier associated to the inequality constraint. Moreover, the KKT conditions:

$$\begin{aligned} \mu\,(c^2 - \boldsymbol{x}^{\intercal}\boldsymbol{x}) &= 0 \qquad \text{(Complementarity)} \\ \mu &\geq 0, \end{aligned} \tag{8.6}$$

are required to obtain the solution to (8.4).

To begin with, the stationary points of (8.5) are determined by solving[3]:

$$\nabla_{\boldsymbol{x}}\mathcal{L} = \Re\{\boldsymbol{B}_{\text{ap}}^{\text{H}}\boldsymbol{h}\boldsymbol{h}^{\text{H}}\boldsymbol{a}_{\text{ap}}\} + \big(\Re\{\boldsymbol{B}_{\text{ap}}^{\text{H}}\boldsymbol{h}\boldsymbol{h}^{\text{H}}\boldsymbol{B}_{\text{ap}}\} - \mu\,\mathbb{I}_{N-1}\big)\boldsymbol{x} = \mathbf{o}. \tag{8.7}$$

Therefore, the critical value of $\boldsymbol{x}$ (denoted $\tilde{\boldsymbol{x}}$) can be expressed as:

$$\tilde{\boldsymbol{x}} = \underbrace{\Big(\mu\,\mathbb{I}_{N-1} - \Re\{\boldsymbol{B}_{\text{ap}}^{\text{H}}\boldsymbol{h}\boldsymbol{h}^{\text{H}}\boldsymbol{B}_{\text{ap}}\}\Big)^{-1}}_{\boldsymbol{M}}\Re\{\boldsymbol{B}_{\text{ap}}^{\text{H}}\boldsymbol{h}\boldsymbol{h}^{\text{H}}\boldsymbol{a}_{\text{ap}}\}. \tag{8.8}$$

[2]– e.g. the problem constraining the ℓ_∞ norm of the solution $\|\boldsymbol{x}\|_\infty = \max_i |\boldsymbol{x}_i|$.

[3]Even though the cost function in (8.4) has intermediate complex variables, the gradient of its Lagrangian can be expressed as a real valued function given that $\boldsymbol{x}$ has been defined as belonging to $\mathbb{R}^{N-1}$.

Note that, $\Re\{\boldsymbol{B}_{\text{ap}}^{\text{H}}\boldsymbol{h}\boldsymbol{h}^{\text{H}}\boldsymbol{B}_{\text{ap}}\}$ can be analyzed by defining the vector $\boldsymbol{v} := \boldsymbol{B}_{\text{ap}}^{\text{H}}\boldsymbol{h}$ and taking the outer product of $\boldsymbol{v}$ with itself, namely:

$$\Re\{\boldsymbol{v}\boldsymbol{v}^{\text{H}}\} = \Re\{\boldsymbol{v}\}\Re\{\boldsymbol{v}\}^{\intercal} + \Im\{\boldsymbol{v}\}\Im\{\boldsymbol{v}\}^{\intercal},$$

showing that $\Re\{\boldsymbol{B}_{\text{ap}}^{\text{H}}\boldsymbol{h}\boldsymbol{h}^{\text{H}}\boldsymbol{B}_{\text{ap}}\}$ has up to (and in practice not less than) two real eigenvalues different from zero.

As a consequence, for $\boldsymbol{M}$ to be well-defined and by complementarity on μ as of (8.6), the norm constraint in (8.4) should be met with equality. Thus, $\boldsymbol{x}^{\intercal}\boldsymbol{x}$ should be strictly equal to c^2.

In other words, when $\mu > 0$ (for a unique solution), the matrix $\boldsymbol{M}$ is full-rank[4], symmetric and, therefore, it can be expressed as:

$$\boldsymbol{M} = \boldsymbol{Q}\big(\mu\,\mathbb{I}_{N-1} - \boldsymbol{\Lambda}\big)^{-1}\boldsymbol{Q}^{\intercal}, \tag{8.9}$$

where $\boldsymbol{Q}\boldsymbol{\Lambda}\boldsymbol{Q}^{\intercal}$ is the eigen decomposition of $\Re\{\boldsymbol{B}_{\text{ap}}^{\text{H}}\boldsymbol{h}\boldsymbol{h}^{\text{H}}\boldsymbol{B}_{\text{ap}}\}$, $\boldsymbol{Q} \in \mathbb{R}^{(N-1)\times(N-1)}$ and $\boldsymbol{\Lambda} \in \mathbb{R}^{(N-1)\times(N-1)}$. Note that μ must also be different from every component of $\boldsymbol{\Lambda}$ for $\boldsymbol{M}$ to be well-defined.

Also, given that $\Re\{\boldsymbol{B}_{\text{ap}}^{\text{H}}\boldsymbol{h}\boldsymbol{h}^{\text{H}}\boldsymbol{a}_{\text{ap}}\}$ in (8.7) belongs to the complex span of $\boldsymbol{v}$ as just defined, it is shown in Appendix B that (8.8) can be re-expressed as:

$$\boldsymbol{x}^* = \boldsymbol{Q}_R \begin{bmatrix} \frac{1}{\mu-\lambda_1} & 0 \\ 0 & \frac{1}{\mu-\lambda_2} \end{bmatrix} \boldsymbol{Q}_R^{\intercal}\Re\{\boldsymbol{B}_{\text{ap}}^{\text{H}}\boldsymbol{h}\boldsymbol{h}^{\text{H}}\boldsymbol{a}_{\text{ap}}\} \tag{8.10}$$

where $\boldsymbol{Q}_R$ corresponds to a tall matrix formed by the eigenvectors associated to λ_1 and λ_2, the non-zero real eigenvalues of $\Re\{\boldsymbol{B}_{\text{ap}}^{\text{H}}\boldsymbol{h}\boldsymbol{h}^{\text{H}}\boldsymbol{B}_{\text{ap}}\}$.

Finally, the norm constraint gives us the solution for μ via the 4^{th} order polynomial equation:

$$\Re\{\boldsymbol{B}_{\text{ap}}^{\text{H}}\boldsymbol{h}\boldsymbol{h}^{\text{H}}\boldsymbol{a}_{\text{ap}}\}^{\intercal}\boldsymbol{Q}_R \begin{bmatrix} \frac{1}{\tilde{\mu}-\lambda_1} & 0 \\ 0 & \frac{1}{\tilde{\mu}-\lambda_2} \end{bmatrix}^2 \boldsymbol{Q}_R^{\intercal}\Re\{\boldsymbol{B}_{\text{ap}}^{\text{H}}\boldsymbol{h}\boldsymbol{h}^{\text{H}}\boldsymbol{a}_{\text{ap}}\} = c^2. \tag{8.11}$$

Moreover, notice the dependence of (8.10) on the so-mentioned eigenvalues. As it can be seen, a rough approximation to the solution of $\boldsymbol{x}$ can be obtained for $\lambda_1 \simeq \lambda_2$ as:

$$\boldsymbol{x}^* \approx \frac{c}{\|\Re\{\boldsymbol{B}_{\text{ap}}^{\text{H}}\boldsymbol{h}\boldsymbol{h}^{\text{H}}\boldsymbol{a}_{\text{ap}}\}\|}\Re\{\boldsymbol{B}_{\text{ap}}^{\text{H}}\boldsymbol{h}\boldsymbol{h}^{\text{H}}\boldsymbol{a}_{\text{ap}}\}, \tag{8.12}$$

from the fact that, when this condition is met, $\boldsymbol{x}^*$ becomes progressively aligned to $\Re\{\boldsymbol{B}_{\text{ap}}^{\text{H}}\boldsymbol{h}\boldsymbol{h}^{\text{H}}\boldsymbol{a}_{\text{ap}}\}$. Consequently, under those circumstances, the

[4]—with a high probability given the dependence of $\boldsymbol{M}$ on $\boldsymbol{h}$

only role of μ is that of fixing the norm of the solution as it is guaranteed in (8.12).

In brief, the solution to (8.4) can be obtained in terms of $\boldsymbol{h}\boldsymbol{h}^{\mathrm{H}}$ according to (8.10) with $\boldsymbol{Q}\boldsymbol{\Lambda}\boldsymbol{Q}^{\intercal} := \Re\{\boldsymbol{B}_{\mathrm{ap}}^{\mathrm{H}}\boldsymbol{h}\boldsymbol{h}^{\mathrm{H}}\boldsymbol{B}_{\mathrm{ap}}\}$ and μ obtained from one of the roots of (8.11), i.e. the one that maximizes (8.4). Moreover, when $\lambda_1 \simeq \lambda_2$, the simpler expression of (8.12) can be used instead.

Overall, an analytic solution to the problem of coherent combination of (8.4) for a genie-aided receiver[5] was presented in (8.10). In particular, such a proposal relied on the linear approximation of the system model as a function of the reactive load vector.

Moreover, the obtained solution was further approximated in (8.12), translating to two different ways to compute the loads that accomplish beamforming. The latter, drawing a complexity-performance trade-off is summarized in Big O notation in Table 8.1. Particularly, m and p in the SPSA-based proposal refer to the number of iterations for the outermost and innermost nested loop cycles, respectively.

Table 8.1: Comparison of the computational complexity of the proposed solutions and the non-linear SPSA-based proposal of Sec. 8.1.1.

	Method		
	Non-linear SPSA of Sec. 8.1.1	**Exact solution of** (8.10) **and** (8.11)	**Approximate solution of** (8.12)
Bottleneck	Doubly nested matrix inverse ($mp \approx 1600$)	Eigen Value Decomposition and quartic roots	Vector norm computation
Computational complexity	$\mathcal{O}(mpN^3)$	$\mathcal{O}(N^3)$	$\mathcal{O}(N)$

8.2 CSI and impedance matrix estimation

As mentioned earlier, such solutions rely on the aid of the so-called genie to supply both the actual CSI and array impedance matrix.

It must be pointed out that, although estimated with the aid of pilot symbols in conventional systems, such full CSI (i.e. $\boldsymbol{h}$) in (7.7) characterizes the channel towards every element (active or not). The latter signifies that, in order to obtain the required CSI through a single RF front-end, N times

[5]– i.e. with perfect knowledge of $\boldsymbol{h}$ and $\mathbf{Z}_{\mathrm{ESPAR}}$.

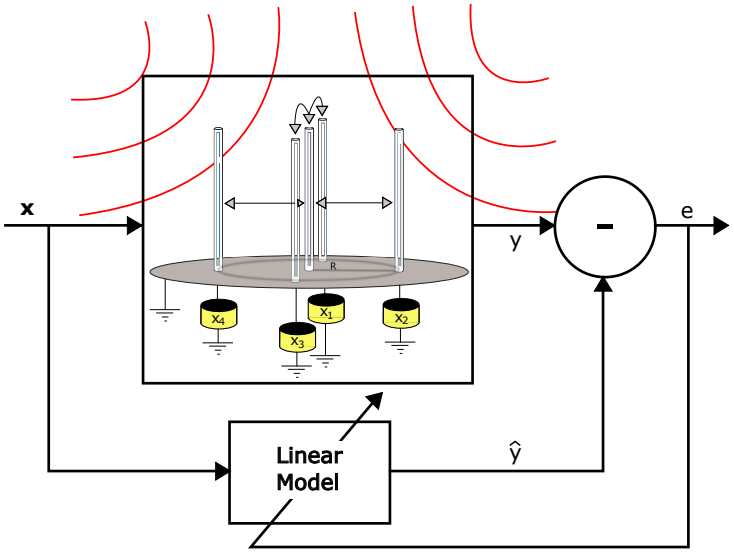

Figure 8.2: Representation of the ESPAR forward modeling problem. The architecture is being fed by the incident waves (on red) and $\boldsymbol{x}$ refers to the set of reactive loads.

more pilot symbols are required to obtain such an estimate compared to conventional multiple RF front-end systems.

Furthermore, estimating $\boldsymbol{h}$ through a single RF front-end as in (7.7) presumes knowledge of $\mathbf{Z}_{\text{ESPAR}}$, propagating any estimation error of $\mathbf{Z}_{\text{ESPAR}}$ to $\boldsymbol{h}$. Even more, the characterization of $\mathbf{Z}_{\text{ESPAR}}$ requires either to rely on simplified models or its estimation in a controlled environment, such as an anechoic chamber [58]. As a consequence, the estimation of these parameters should not be disregarded in practical implementations and it motivated its study in this project.

The rest of the current section develops on two methods that circumvent the need of the *genie* to solve the proposed convex optimization problem of Sec. 8.1.2 by allowing to quickly (in terms of the demanded amount of pilot symbols) characterize the response of ESPAR, further exploiting the proposed linearization.

Particularly, as it will be shown, a characterization of the combined impact of $\boldsymbol{h}$ and $\mathbf{Z}_{\text{ESPAR}}$ is what is required to carry out such an optimization.

Linearized-model parameter estimation

Let us begin by reordering the system model (7.7). The base band received signal at the single RF front-end can be considered a function of the reactive

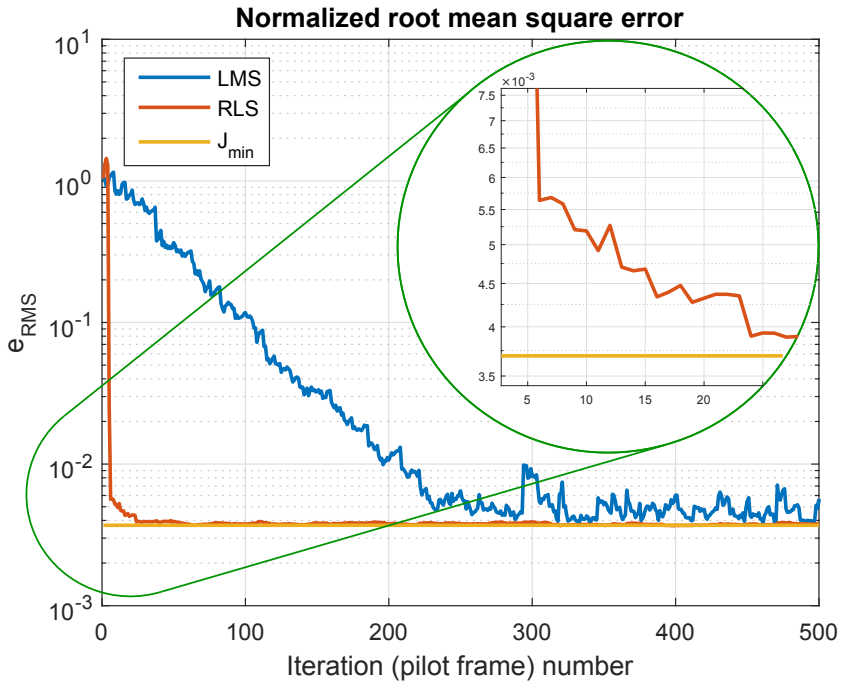

Figure 8.3: RMS error of (8.17) over both the LMS (blue) and RLS (red) methods on a specific channel realization for the purpose of convergence speed comparison. Minimum is also shown in yellow for reference.

load vector $\boldsymbol{x}$ and expressed as:

$$y = s\,\boldsymbol{h}^{\intercal}\overline{\boldsymbol{w}}(\boldsymbol{x}) + n, \tag{8.13}$$

where $\overline{\boldsymbol{w}}$ stands for the complex conjugate of $\boldsymbol{w}$ and the dependence of $\boldsymbol{w}$ on $\boldsymbol{x}$ through (7.8) was made explicit for clarity. Consequently, and according to (7.12), the noiseless received signal can be approximated as a linear function of the load vector as:

$$\hat{y} = \boldsymbol{g}^{\mathrm{H}}\boldsymbol{x}_{\mathrm{e}}, \qquad \boldsymbol{x}_{\mathrm{e}} := \begin{bmatrix} 1 \\ \boldsymbol{x} \end{bmatrix}, \tag{8.14}$$

where introducing $\boldsymbol{x}_{\mathrm{e}} \in \mathbb{R}^N$ allows to capture an affine dependence on the set of reactive loads. Note that s has been set to one in (8.14) without loss of generality. This factor can be presumed known a priori for pilot symbol time-slots and be compensated for.

Moreover, by observation of the linear approximation in (7.12) and (8.14), $\boldsymbol{g}$ can be written as (under the norm constraint allowing for the linear approximation to take place):

$$\boldsymbol{g} = \begin{bmatrix} \boldsymbol{a}_{\mathrm{ap}}^{\intercal} \\ \boldsymbol{B}_{\mathrm{ap}}^{\intercal} \end{bmatrix} \overline{\boldsymbol{h}}, \tag{8.15}$$

with $\boldsymbol{a}_{\text{ap}}$ and $\boldsymbol{B}_{\text{ap}}$ given by (7.12). Observe that $\boldsymbol{g}$ captures information both about the propagation environment and the ESPAR impedance matrix $\mathbf{Z}_{\text{ESPAR}}$ as effectively impacting the behavior of the received signal. More importantly, through (8.15), the solutions (8.10) and (8.12) to the spatial processing optimization problem presented in Sec. 8.1.2 are given exclusively in terms of $\boldsymbol{g}$.

In light of the latter, the problem at hand can be posed as one of forward modeling, i.e. that of Fig. 8.2, in particular:

$$\boldsymbol{g} = \arg\min_{\tilde{\boldsymbol{g}}} e\big(y, \hat{y}(\tilde{\boldsymbol{g}})\big), \tag{8.16}$$

where $e\big(y, \hat{y}(\tilde{\boldsymbol{g}})\big)$ is a cost function chosen according to any estimation method. Indeed, ESPAR is successfully characterized when e is minimized according to some measure with respect to the parameters of the linear model.

The methods of least mean squares (LMS) and recursive least squares (RLS) have been studied in this project as a mean of estimating $\boldsymbol{g}$. Consequently, Appendix C and Appendix D are devoted to deepening on the details for the problem under consideration.

Table 8.2: Complexity of LMS vs. RLS per update step

	Method	
	LMS Appendix C	**RLS** Appendix D
Bottleneck	Dot product	Vector linear transformation
Computational complexity	$\mathcal{O}(N)$	$\mathcal{O}(N^2)$

Nonetheless, for the sake of brevity, observe in Table 8.2 a summary of their computational complexity.

For the purpose of convergence speed comparison, the normalized error:

$$e_{\text{RMS}}(\boldsymbol{g}) := \sqrt{\frac{\mathbb{E}_{\boldsymbol{x}}\{|y - \hat{y}(\boldsymbol{g})|^2\}}{\mathbb{E}_{\boldsymbol{x}}\{|y|^2\}}}, \tag{8.17}$$

is shown along the adaptation process in Fig. 8.3 for LMS and RLS over a single channel realization.

As observed in Fig. 8.3, $J_{\min}$ corresponds to the minimum estimation error of $\boldsymbol{g}$ from (C.3) (i.e. with the covariance matrix and cross-correlation vector estimated from a large sample set). The difference in convergence speed is evidently significant, RLS converges close to $J_{\min}$ in less than 10 iterations, whereas LMS requires around 20 times that amount of iterations.

8.3 Proposed receiver algorithm

Based on the work of this chapter, and particularly of the low-complexity convex optimization for spatial adaptation, Algorithm 1 shows the pseudo-code of the four possible alternative proposals. To be specific, such alternatives result from the combination of the two estimation methods (i.e. LMS and RLS) and the two solutions of Sec. 8.1.2 (i.e. exact and approximate).

Algorithm 1 General structure of receiver's algorithm for spatial adaptation

Initialize $\boldsymbol{g}$, c
while reception **do**
  if pilot symbol **then**
    pick $\boldsymbol{x}_{\text{temp}}(n)$ from dictionary and set it as loads
    obtain $y(n)$
    set $\boldsymbol{x}_{\text{e}}(n)$ based on $\boldsymbol{x}_{\text{temp}}(n)$ through (8.14)
% **Updating $\boldsymbol{g}$**
    if LMS **then**
      compute $e(n) = y(n) - \boldsymbol{g}^{\text{H}}(n)\boldsymbol{x}_{\text{e}}(n)$
      update $\boldsymbol{g}(n+1) = \boldsymbol{g}(n) + \eta\, \boldsymbol{x}_{\text{e}}(n)\overline{e}(n)$
    else if RLS **then**
      compute $\boldsymbol{q}$ through (D.5)
      compute $\alpha(n) = y(n) - \boldsymbol{g}^{\text{H}}(n-1)\boldsymbol{x}_{\text{e}}(n)$
      update $\boldsymbol{g}(n) = \boldsymbol{g}(n-1) + \boldsymbol{q}\,\overline{\alpha}(n)$
      update $\boldsymbol{R}^{-1}_{\lambda,xx}$ through (D.6)
    end if
% **Updating $\boldsymbol{x}^*$**
    if approximate solution **then**
      compute $\boldsymbol{x}^*$ through (8.12) and (8.15)
    else if exact solution **then**
      compute $\boldsymbol{Q}$ and $\boldsymbol{\Lambda}$ for $\Re\{\boldsymbol{B}^{\text{H}}_{\text{ap}}\boldsymbol{h}\boldsymbol{h}^{\text{H}}\boldsymbol{B}_{\text{ap}}\}$ with (8.15)
      find $\tilde{\mu}_i\, \forall\, i$ through (8.11) and (8.15)
      compute $\mathcal{X} = \{\boldsymbol{x}^*(\tilde{\mu}_i)\, \forall\, i\}$ from (8.10) and (8.15)
      select $\boldsymbol{x}^* = \arg\max_{\boldsymbol{x}\in\mathcal{X}} \left|\boldsymbol{g}^{\text{H}}\boldsymbol{x}_{\text{e}}(n,\boldsymbol{x})\right|$
    end if
  else if unknown data symbol **then**
    set $\boldsymbol{x}^*$ as loads
    obtain $y(n)$
    decode unknown data
  end if
end while

8.4 Obtained performance

As a means of evaluating the performance of the proposed algorithms, a Monte-Carlo simulation tool was implemented.

Two different environments were considered, namely: a non-directional so-called Clarke's channel model and an A1 non-line of sight (NLOS) WINNER scenario for directional propagation.

The Clarke's environment is implemented as 30 angular uniformly distributed and equally powerful incident rays at the ESPAR receiver[6]. On the other hand, the WINNER A1 NLOS propagation environment is simulated as indicated in its documentation[7]. Both of the here simulated environments assume horizontal incidence at the ESPAR receiver side.

Additionally, 4-QAM single-carrier modulation and minimum distance detection is simulated in all cases. The performance results of the SPSA-based optimization algorithm proposed in Sec 8.1.1 will also be illustrated. In particular, to the authors knowledge, strict optimallity over the non-linear has not yet been demonstrated in the literature, which is the reason why researchers have relied on heuristic alternatives [35].

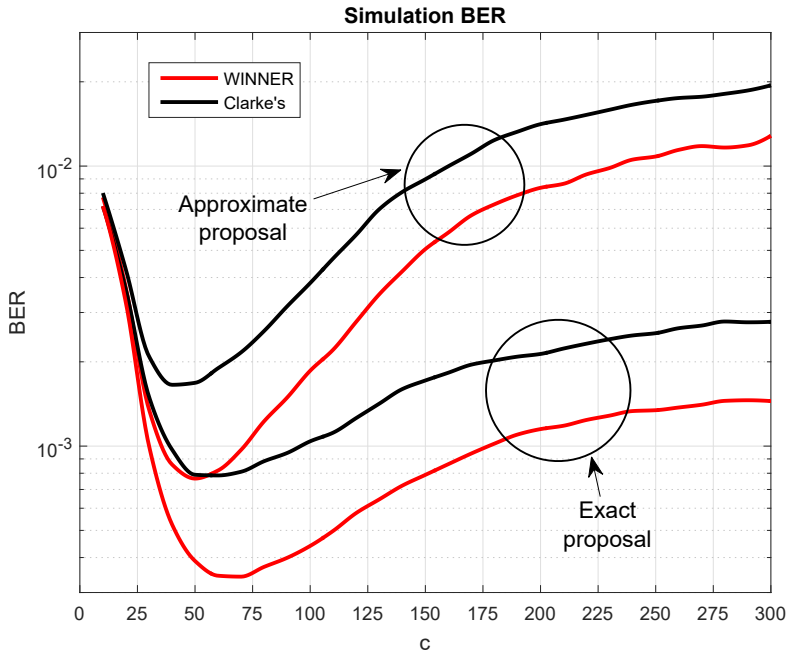

Figure 8.4: BER vs. norm constraint for the exact and approximate algorithms over the Clarke's and WINNER channel models. SNR = 6 dB.

[6]– i.e. with a uniform angular power spectrum

[7]WINNER II Deliverable D1.1.2 V1.1, 2007.

To begin with, in order to study the sensitivity of the convex algorithms of Sec. 8.1.2 on c, as well as conclude on the allowed linearization error, Fig. 8.4 shows the BER with respect to the vector norm for 6 dB of SNR.

To be specific, Fig. 8.4 shows that the best balance between linearization error and beamforming capability (restricted when the vector norm is too small) is obtained for $c \approx 50\Omega$, which ultimately corresponds to 7-10% of linearization error according to Fig. 7.3.

As a consequence, the norm constraint of (8.4) was set to $c = 50\Omega$ for all cases, as it was found to balance the linearization and beam-forming performance.

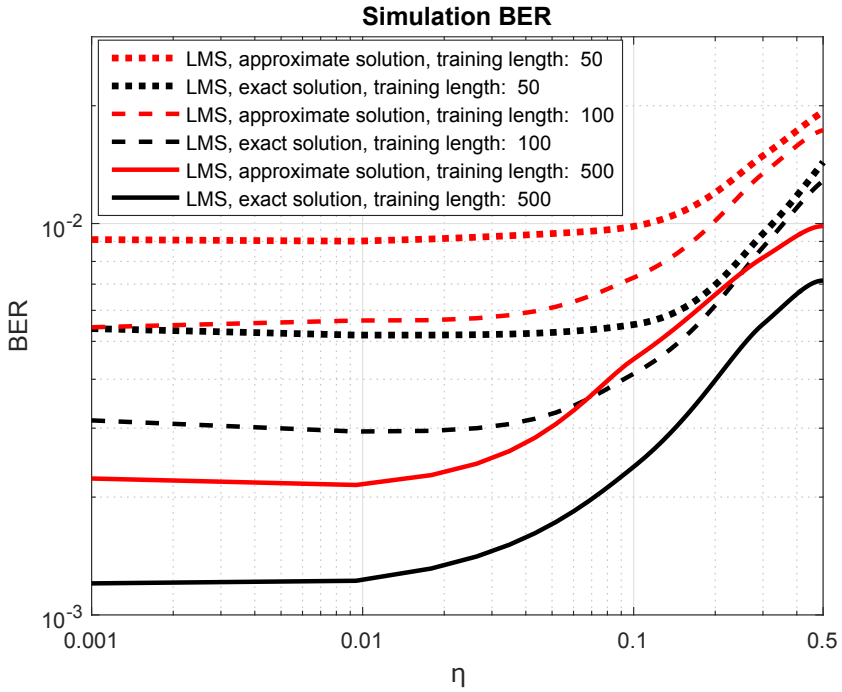

Figure 8.5: BER performance vs. LMS step size η for 100 and 500 samples of training length. Clarke's channel model and SNR = 6 dB.

Subsequently, it was found that the performance of the LMS-based algorithms is highly sensitive to the variation of the step-size η above 3×10^{-2}. As observed in Fig. 8.5, values of η of the order of $\sim 10^{-3}$ perform better almost independently of the training length.

Consequently, throughout the rest of the simulation results, η is set to 0.01 not to unnecessarily increase the convergence time for the LMS-based algorithms. On the other hand, as time-varying channels are out of the scope of this work, a value of $\lambda = 0.98$ is used for the RLS-based alternatives.

Table 8.3: Computational complexity and expected convergence speed of the proposed algorithms.

		Convergence speed	
		Lower (LMS)	**Higher (RLS)**
Computational complexity	**Lower** $\mathcal{O}(N)$	**Proposal 1** LMS with approximate solution	
	Medium $\mathcal{O}(N^2)$		**Proposal 3** RLS with approximate solution
	Higher $\mathcal{O}(N^3)$	**Proposal 2** LMS with exact solution	**Proposal 4** RLS with exact solution

As summary, the algorithms are classified in Table 8.3 in terms of their convergence speed and computational complexity. In fact, it is observed in Fig. 8.6 that, as expected, the LMS method falls behind RLS as regards convergence speed. In particular, the LMS method performs similar to RLS for around ten times as many pilot symbols.

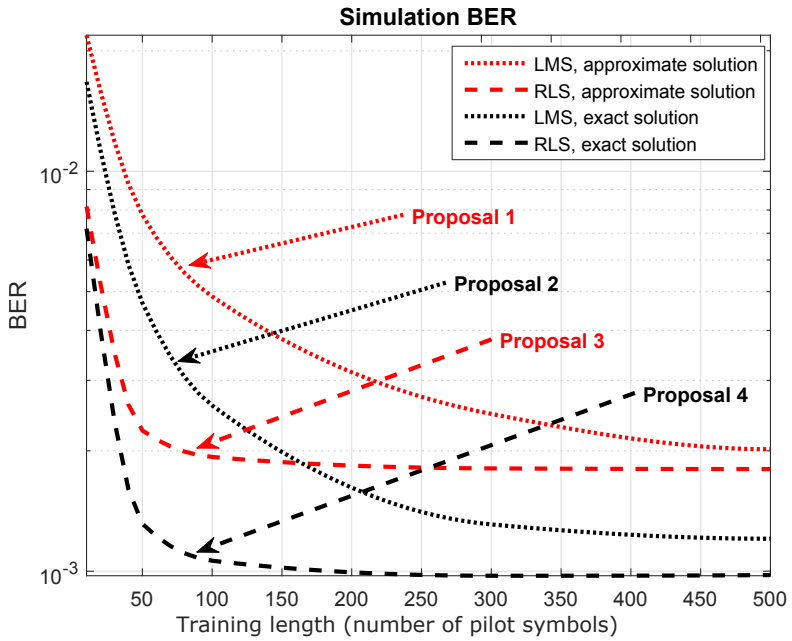

Figure 8.6: Convergence speed evaluation via BER with an SNR of 6 dB. Clarke's channel model. $\lambda = 0.98$ for RLS and $\eta = 0.01$ for LMS.

Then, setting the amount of pilot symbols (i.e. training length) to 50 on RLS and 500 on LMS for fairness on their degree of convergence, the BER performance vs. SNR is shown for the Clarke's environment in Fig. 8.7.

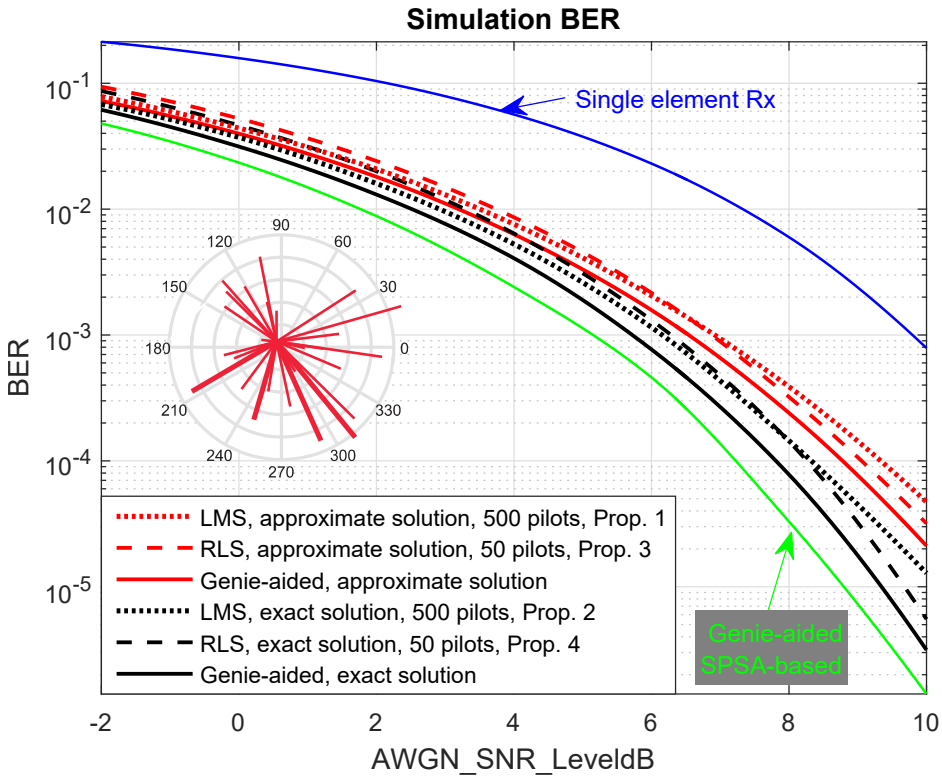

Figure 8.7: Performance comparison of RLS vs. LMS via BER over Clarke's environment. A realization of such an environment is shown for reference. $\lambda = 0.98$ for RLS and $\eta = 0.01$ for LMS. Genie-aided SPSA-based of Sec. 8.1.1 shown as reference.

Note that the performance of the RLS-based proposals is very similar to that of the LMS-based ones under these circumstances. In spite of the latter, note that the RLS-based algorithms approach more closely the performance of the genie-aided receiver.

In order to study the behavior of the proposed algorithms over directional environments, their performance was also evaluated over the A1 NLOS indoor office WINNER scenario in Fig. 8.8.

Based on Fig. 8.7 and Fig. 8.8, it is evident that the performance of the proposals (both in absolute BER terms and relative to one another) is very similar under such different environments. Overall, a small improvement on the BER is observed in directional channels as explained by the ability of

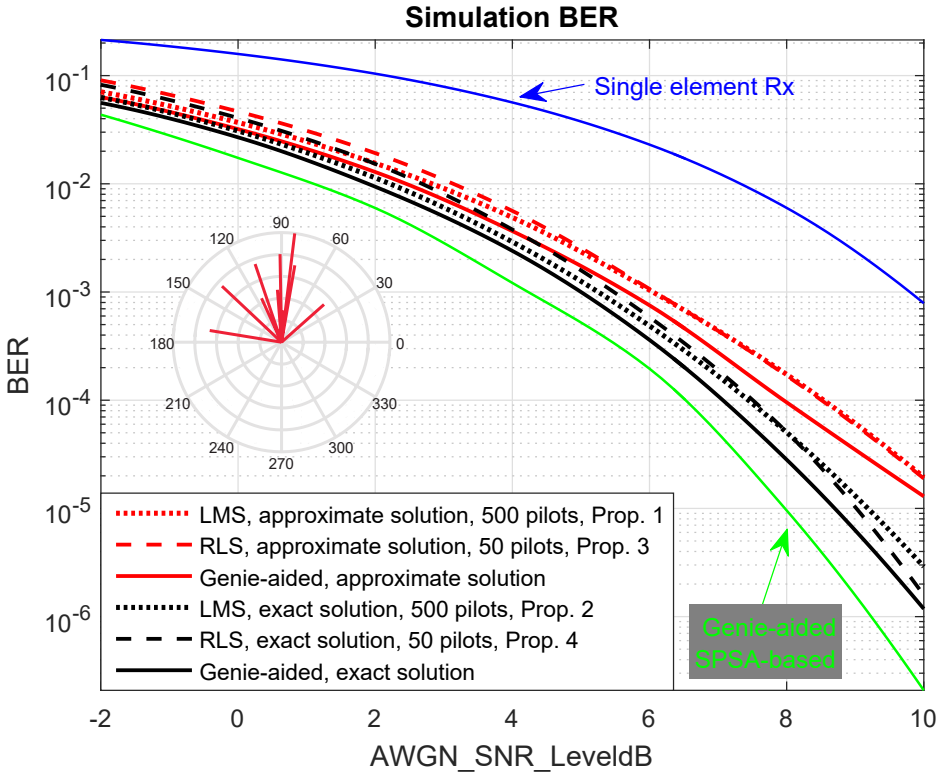

Figure 8.8: Performance comparison of RLS vs. LMS via BER over A1 NLOS WINNER environment. A realization of such an environment is shown for reference. $\lambda = 0.98$ for RLS and $\eta = 0.01$ for LMS. Genie-aided SPSA-based of [57] shown as reference.

ESPAR to extract a higher gain over limited angle spread environments.

To proceed, and as a means of evaluating the potential gains of increasing its number of elements, the performance of a 7-element ESPAR with the same evenly distributed circular architecture and radius as Fig. 7.2 was simulated.

As it can be observed in Fig. 8.9, the 7-element array gives a closer performance for the approximate and exact solutions (both for the genie-aided and RLS-based algorithms) compared to the 5-element counterpart as explained by the smaller λ_1/λ_2 in Table 8.4 (recall that the approximate and exact solutions coincide in the limit when $\lambda_1/\lambda_2 = 1$).

As it is shown in the smaller plot of the same figure, the more dense 7-element array gives $c = 80\Omega$ as optimal norm (unlike the 5-element ESPAR where a value of $c = 50\Omega$ was given use). Recall that such a norm does not interact with the AWG noise n in (7.7). Thus, the optimal norm is independent of SNR as of (8.4).

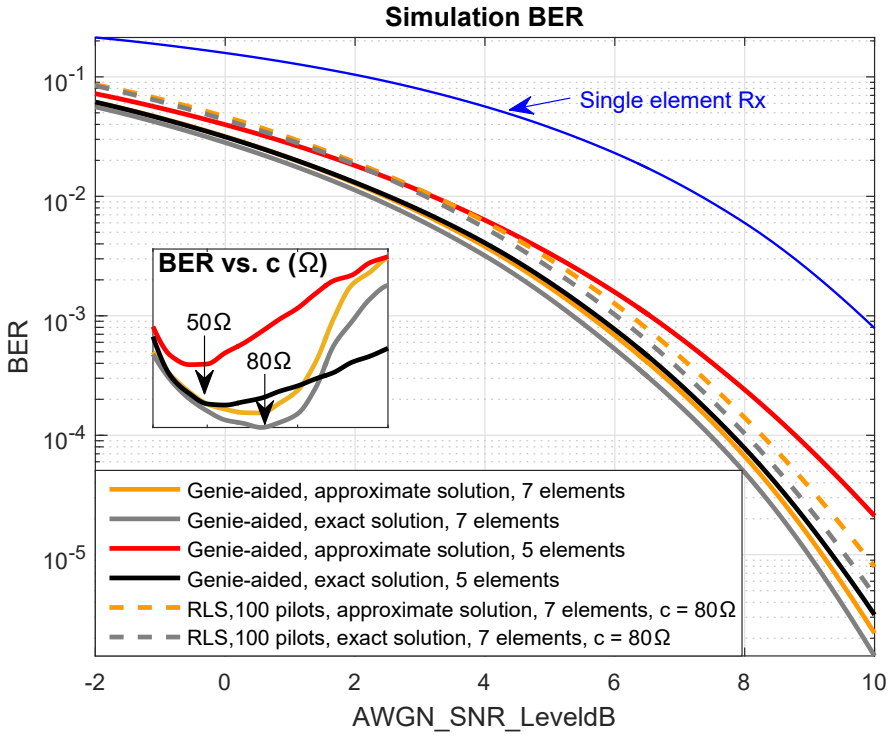

Figure 8.9: RLS performance comparison for 5 and 7 element ESPAR via BER vs. SNR over Clarke's environment. SNR = 6 dB for subplot.

Moreover, as it can be observed in Fig. 8.9, the proposal 3 over a 7-element ESPAR (dashed yellow curve) of complexity $\mathcal{O}(N^2)$ performs close to the exact-solution genie-aided of complexity $\mathcal{O}(N^3)$ over a 5-element ESPAR (continuous black curve). As such, a computational complexity reduction could be achieved using a 7-element instead of 5-element array, i.e. as $7^2 < 5^3$. Naturally, due to the increase on information to estimate, the latter comes at the expense of a two-fold increase in the convergence time.

Table 8.4: Average λ_1/λ_2 over considered Clarke's and WINNER environments on 5-element and 7-element ESPAR

λ_1/λ_2	**Architecture**	
Channel model \ Number of elements	**5-element** ESPAR	**7-element** ESPAR
Clarke's	10.13	4.67
WINNER	19.41	5.13

Chapter 9

Spatial demultiplexing using ESPAR

The Electronically Steerable Parasitic Array Radiator has also been proposed as a mean of achieving low-cost spatial multiplexing with a single radio frequency (RF) front end [17, 36].

Specifically, spatial multiplexing (SM) is a technique that consists in accessing the spatial domain of wireless environments in order to profit from its richness as a means of simultaneously conveying multiple streams of information that coincide in time and frequency, using multiple radiating elements. Although it is not always the case, it is often assumed a perfect control of the array currents in conventional multi-RF architectures, ignoring both electromagnetic coupling and spatial correlation of the fields.

Even-though ESPAR was originally conceived as a reactively controlled directive array [14], it was shown around a decade ago to be capable of achieving inexpensive spatial multiplexing. Additionally, in spite of its compactness, it inherently accounts for mutual coupling between radiating elements.

Particularly, in transmission, the so-called beamspace modulation [17] can be seen as a form of spatial multiplexing in which multiple streams of information are simultaneously encoded onto a set orthogonal radiation patterns. Indeed, as the array feeding is mediated via mutual coupling, not any arbitrary distribution of currents is achievable by the use of purely reactive loads.

On the other hand, in reception, while variable loads can be simultaneously controlled, they cannot all be probed at the same time. The latter makes ESPAR an inherently asymmetric device in the sense that information can be conveyed via several loads but only retrieved through a single RF front end.

The current chapter expands on the impact of the oversampling rate on

capacity and proposes an algorithm for the reactance optimization, based on channel state information at the receiver side.

A comparison with a multiple-element multiple-RF front end array (ME-MRF) of identical geometry (that of Fig. 7.2) is drawn to study the ability of ESPAR to perform control on the induced currents.

To sum up, the challenge of ESPAR for SM in reception can be summarized as a) a constrained set of achievable currents due to its control mechanism through the use of purely reactive loads, and b) the SNR degradation problem that is explained in more detail in the following section.

Let us begin by emphasizing that ESPAR is provided with a single RF front end. The latter means that, by controlling the set of reactive loads in reception, the radiation properties of the array are controlled, but at most a single simultaneous *spatial sample* can be retrieved. In connection with the model in (7.7), this can be represented by:

$$y = \boldsymbol{w}^{\mathrm{H}} \boldsymbol{H} \boldsymbol{s} + n, \tag{9.1}$$

where $\boldsymbol{w}$ corresponds to the equivalent weight vector in (7.8), $\boldsymbol{s}$ corresponds to the transmit vector at the ME-MRF transmitter array with $\mathbb{E}(\boldsymbol{s}\boldsymbol{s}^{\mathrm{H}}) = {}^{E_S}/_{N_T}\, \mathbb{I}_{N_T}$ and n corresponds to AWGN with $\mathbb{E}(n) = N_0$.

Like (7.7), the model in (9.1) shows that the received signal at the active element is the projection of the signal experienced at every element of the ESPAR array (represented by $\boldsymbol{H}\boldsymbol{s}$) onto the equivalent weight vector $\boldsymbol{w}$.

9.1 Oversampling and SNR degradation

Given that (9.1) corresponds to the scenario where only a single sample is obtained per symbol time, it has been suggested [59] to oversample the received signal[1] in order to effectively extract multiple samples per effective one symbol time.

The practical implementation of such a signal oversampling can be represented by the shortening of the matched filter at the receiver side. Its implications are, nonetheless, detrimental to the system performance.

In particular, the signal energy captured during the shorter matched filter time-lapse is reduced by a factor equivalent to the oversampling rate. On the other hand, given the uncertainty principle in signal processing [60], the shortening of the matched filter results in a widening of its capture spectrum.

The latter implies that the noise energy captured during the shorter matched filter extent is equal to the corresponding longer one. As a con-

[1] Specially, given the fast response of the varactor devices used as controllable loads.

sequence of the reduction in the captured signal energy with respect to the noise, the SNR is reduced by the oversampling rate [19, 59].

In short, the operation achieved by signal oversampling can be expressed shortly in matrix notation, which allows to rewrite the system model as:

$$\boldsymbol{y} = \frac{1}{\sqrt{N_S}}\boldsymbol{W}^{\mathrm{H}}(\boldsymbol{x})\boldsymbol{H}\boldsymbol{s} + \boldsymbol{n}, \tag{9.2}$$

$$\boldsymbol{W}(\boldsymbol{x}) := \begin{bmatrix}\boldsymbol{w}(\boldsymbol{x}_1) & \boldsymbol{w}(\boldsymbol{x}_2) & \dots & \boldsymbol{w}(\boldsymbol{x}_{N_S})\end{bmatrix}, \tag{9.3}$$

where $\boldsymbol{y} \in \mathbb{C}^{N_S}$ and $\boldsymbol{n} \in \mathbb{C}^{N_S}$ with N_S representing the oversampling rate and $\mathbb{E}(\boldsymbol{n}\boldsymbol{n}^{\mathrm{H}}) = N_0\,\mathbb{I}_{N_S}$.

Moreover, observe that $\boldsymbol{x} = [\boldsymbol{x}_1^{\intercal}, \dots, \boldsymbol{x}_{N_S}^{\intercal}]^{\intercal}$ is the vector of reactive loads for the N_S sub-slots of time and that, through $\boldsymbol{x}$, $\boldsymbol{W}(\boldsymbol{x})$ gives a total of $(N-1)\times N_S$ degrees of freedom.

9.2 Capacity

Based on (9.2), the capacity of a system with ESPAR at the receiver side and a channel-ignorant ME-MRF transmitter can be shown to be:

$$C(\boldsymbol{x}) = \log_2 \det\left(\mathbb{I}_{N_S} + \frac{E_S}{N_T N_S N_0}\boldsymbol{W}^{\mathrm{H}}(\boldsymbol{x})\boldsymbol{H}\boldsymbol{H}^{\mathrm{H}}\boldsymbol{W}(\boldsymbol{x})\right), \tag{9.4}$$

showing that the oversampling rate has a similar role as the number of antenna elements on ME-MRF systems, i.e. constraining the multiplexing gain.

Nonetheless, unlike the number of receive antenna elements in ME-MRF, increasing the oversampling rate results in a corresponding increase of the SNR degradation, which negatively impacts the capacity.

The latter suggests that there is a value of N_S that maximizes the capacity given environment-related conditions, namely: channel richness and SNR.

Note also that, in the high SNR regime, the capacity for ESPAR in reception can be shortly expressed as:

$$C_{\text{High SNR}}(\boldsymbol{x}) = N_S \log_2\left(\frac{E_S}{N_T N_S N_0}\right) + \log_2 \det\left(\boldsymbol{W}^{\mathrm{H}}(\boldsymbol{x})\boldsymbol{H}\boldsymbol{H}^{\mathrm{H}}\boldsymbol{W}(\boldsymbol{x})\right), \tag{9.5}$$

where it is clearly shown the separability of the SNR and $\boldsymbol{W}$.

As a preamble, the definition of $\boldsymbol{W}$ as a function of the reactive loads in (9.3) is relaxed in what follows as a way to study the impact of the SNR degradation (determined by N_S) alone. Subsequently, these results will be used to evaluate the impact of the structure of $\boldsymbol{W}$ and N_S on capacity.

Therefore, the system eigen-decomposition[2] is enforced through $\boldsymbol{W}$ (i.e.

[2]– given by $\boldsymbol{H}\boldsymbol{H}^{\mathrm{H}} = \boldsymbol{Q}\boldsymbol{\Lambda}\boldsymbol{Q}^{\mathrm{H}}$ with eigen-values λ_n $\forall n$.

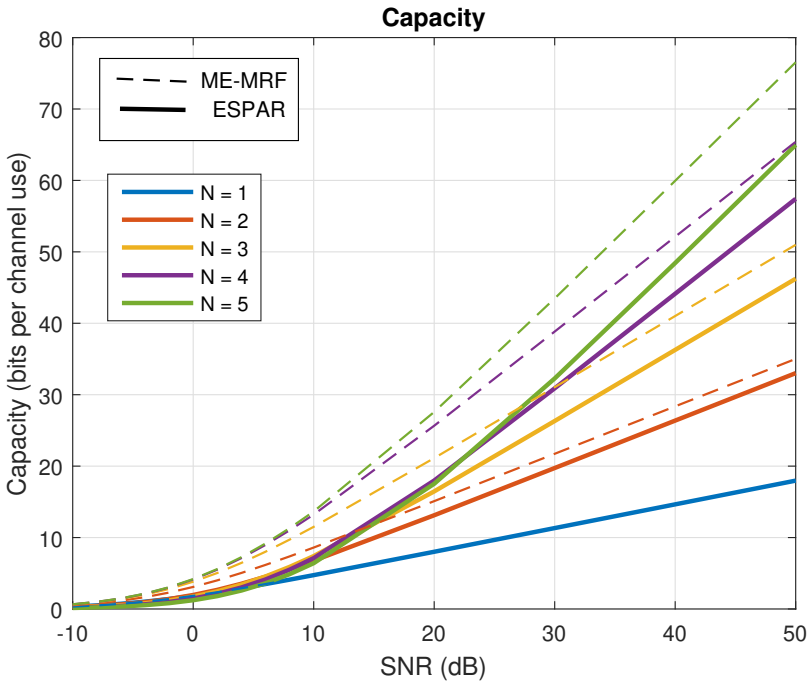

Figure 9.1: Ergodic capacity of ME-MRF and ESPAR for relaxed constraint on $\boldsymbol{W}$. N corresponds to N_S for ESPAR and to the number of eigen vectors used at post processing for ME-MRF. Receiver architecture given by Fig. 7.2 and ME-MRF UCA transmitter with $N_T = 5$ for all cases.

setting $\boldsymbol{W} = \boldsymbol{Q}$) to access the eigen-modes of the channel, giving:

$$C(\boldsymbol{W}{=}\boldsymbol{Q}) = \sum_{n=1}^{N_S} \log_2 \left(1 + \frac{E_S}{N_T N_S N_0} \lambda_n\right). \tag{9.6}$$

In fact, as hinted by (9.6), Fig. 9.1 shows that the impact of the oversampling rate on capacity corresponds to an SNR shift with respect to conventional ME-MRF reception.

In particular, the evaluated environment corresponds to $K = 40$ paths with uniformly-distributed angles (and uniform angular power spectrum) both at the transmitter and receiver sides, also called Clarke's in Chapter 8.

As observed in Fig. 9.1, the oversampling rate could be upper-bounded to two without performance loss below 10 dB of SNR. This can be explained by the fact that, at low SNR, the SNR degradation overcomes the multiplexing gain. On the contrary, at high SNR, there is benefit from increasing the oversampling rate despite the SNR degradation.

Additionally, based on (9.6), the region for which an oversampling rate of two gives a higher capacity than one can be found.

If we take λ_1 and λ_2 to be the highest decreasingly-ordered eigenvalues of $\boldsymbol{H}\boldsymbol{H}^{\mathrm{H}}$, it can be shown that $C(N_S = 2) \geq C(N_S = 1)$ if the SNR is above a certain threshold. This region is given by:

$$\frac{E_S}{N_T N_0} \geq \left(\frac{\lambda_1}{\lambda_2} - 1\right)\frac{2}{\lambda_1}. \tag{9.7}$$

Recall that, based on Fig. 9.1, the performance loss associated to upper-bounding the oversampling rate to two is negligible for low SNR. The latter means that, if $\boldsymbol{W}$ could be arbitrarily set, (9.7) would determine the capacity-achieving N_S on low SNR.

In fact, the region represented by such inequality can be expressed as a function of the strongest eigenvalue and the spread of the two strongest eigenvalues, as shown in Fig. 9.2.

The arrows in Fig. 9.2 mean that the region of each eigenvalue spread extends from their corresponding lower-bound towards $+\infty$ SNR. Moreover, the region related to $\lambda_1/\lambda_2 = 1$ is unbounded and, therefore, an oversampling

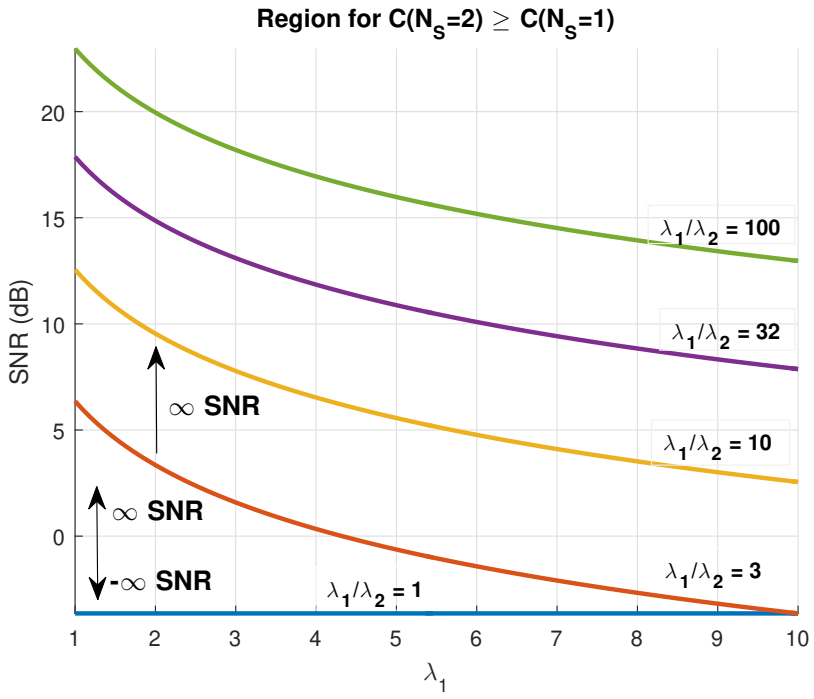

Figure 9.2: Region representing the conditions to be met to obtain $C(N_S{=}2) \geq C(N_S{=}1)$ for different eigen-spreads.

rate of two is capacity achieving for any SNR, if such a condition on the eigen-spread is met.

9.3 SPSA-based achievable rate maximization

Given the complexity of analytically studying the impact on capacity of $\boldsymbol{W}$ as a function of $\boldsymbol{x}$, an optimization algorithm is used in the current section for achievable rate maximization. In particular, the latter will allow to draw conclusions based on the results of Sec. 9.2.

In fact, such an optimization could be used to maximize the achievable rate based on channel state information (CSI).

Based on (9.5), the impact of the specific set of reactive loads $\boldsymbol{x}$ synthesizing $\boldsymbol{W}$ on capacity for the high SNR regime is given by:

$$L(\boldsymbol{x}) = \log_2 \det\left(\boldsymbol{W}^{\mathrm{H}}(\boldsymbol{x})\boldsymbol{H}\boldsymbol{H}^{\mathrm{H}}\boldsymbol{W}(\boldsymbol{x})\right), \tag{9.8}$$

where the dependence of $\boldsymbol{W}$ on the reactive loads $\boldsymbol{x}$ was made explicit.

It must be noted that the sets of reactive loads are expressed shortly as $\boldsymbol{x} \in \mathbb{C}^{N_S(N-1)}$ and that the computational complexity per-evaluation of (9.8) is related to N_S $N\times N$-sized matrix inverses plus the computation of the determinant of an $N_S\times N_S$-sized matrix.

Given (9.8), the SPSA method [19] introduced in Chapter 8 is used to maximize and evaluate the ability of $\boldsymbol{W}$ to approach the capacity of Sec. 9.2, i.e. with respect to the optimum $\boldsymbol{W}$.

The used SPSA parameters, according to the notation in [19], are:

$$\begin{aligned} \beta(m) &= 120\,\exp\left(-{}^{m}\!/_{20}\right) \\ \tau(n) &= 120\,\exp\left(-{}^{n}\!/_{20}\right) \\ M_{\texttt{opt}} = 50,\ \text{tot-iters} &= 50,\ \text{tol} = 1\times 10^{-6}. \end{aligned} \tag{9.9}$$

There is an interest in using SPSA in spite of its non-guaranteed optimality due to the unavailability of the gradient of (9.8) and its low computational complexity with respect to other methods [19]. Moreover, the results of such an algorithm are, nonetheless, informative. Thus, the so-mentioned problem can be shortly stated as:

$$\begin{aligned} \boldsymbol{x}^* := \arg\max_{\boldsymbol{x}} \quad & \log_2 \det\left(\boldsymbol{W}^{\mathrm{H}}(\boldsymbol{x})\boldsymbol{H}\boldsymbol{H}^{\mathrm{H}}\boldsymbol{W}(\boldsymbol{x})\right) \\ \text{s.t.} \quad & \Im(\boldsymbol{x}) = \mathbf{o} \end{aligned} \tag{9.10}$$

Particularly, Fig. 9.3 shows the ergodic capacity of (9.4) obtained by employing SPSA to approach (9.10). Additionally, the capacity obtained in Sec. 9.2 (hence-called Relaxed $\boldsymbol{W}$ capacity) is shown for reference.

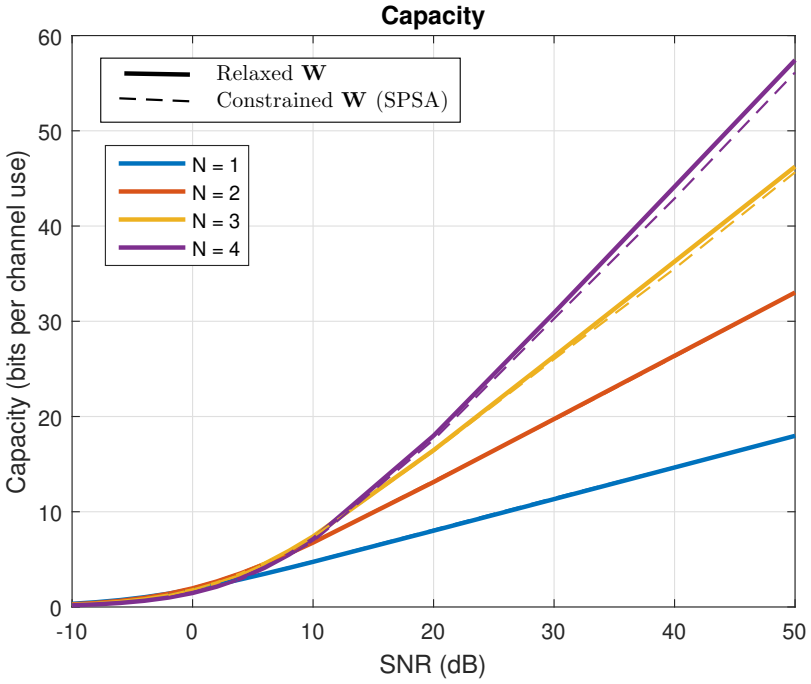

Figure 9.3: Ergodic capacity for constrained (via SPSA on (9.9)) and relaxed (through the eigen-mode access of Sec. 9.2) $\boldsymbol{W}$ vs. SNR for ESPAR. $N_T = 5$ for all cases.

It can be observed that SPSA is able to find a set of purely reactive loads that gives a rate close to the capacity obtained in Sec. 9.2.

The curves in Fig. 9.1 and Fig. 9.3 also suggest that the biggest detriment on capacity for ESPAR on reception compared to ME-MRF is due to the oversampling SNR degradation.

As opposed to what could be expected, the structure on $\boldsymbol{W}$ being restricted to a set of purely reactive loads does not translate into the unattainability of the space of matrices in $\mathbb{C}^{N\times N_S}$ reaching the capacity of Sec. 9.2.

9.4 Discussion

Given that the algorithm of the previous section can be seen as one of achievable rate maximization, such an algorithm can be used to find a set of reactive loads for a given channel estimate $\boldsymbol{H}$.

Taking into consideration the restriction of purely reactive loads, it is shown that by the use of the simultaneous perturbation stochastic approximation method (SPSA), it is possible to closely approach capacity subject

to the unavoidable SNR degradation due to oversampling.

Even more, it can be shown that, for the case of $N_S = N_T = 1$, the SPSA algorithm of Sec. 9.3 converges to the SPSA-based algorithm for coherent combination of Sec. 8.1.1 as a particular case.

Furthermore, the adoption of the presented SPSA algorithm is proposed as a mean of finding the set of loads that maximize the achievable rate.

In spite of its computational complexity, it must be reminded that at low SNR (see Fig. 9.1 and Fig. 9.3) there is little gain by increasing N_S over two, which also bounds the required computational complexity. Particularly, the computational complexity for $N_S = 2$ is similar to the one required for $N_S = 1$ except for the extra 2×2-sized matrix determinant computation.

Finally, in light of the results in Fig. 9.3, the inequality of (9.7) can be used to determine if $N_S = 2$ indeed increases the achievable rate given the specific conditions.

Part III

Digitally controllable scatterers

Chapter 10

Introduction

Wireless environments are challenging due to the abundant phenomena they are subject to. In particular, small scale fading due to multi-path propagation can turn good coverage into zero reception with a displacement of less than a wavelength. On the other hand, large scale fading translates into a restricted communication range and multiple coverage holes. Thus, multi-hop communication schemes through dedicated devices, i.e. relays, was proposed since many decades ago [61] and it is still a topic of active research [62].

Decode-and-forward (DAF) relays were proposed as a means of propagation loss and shadowing compensation. As a matter of fact, any conventional half-duplex transceiver can be employed as a DAF relay with very little modification. Nonetheless, from a network perspective, the coordination overhead and DAF time decoupling introduce significant latency.

Alternatively, amplify-and-forward (AAF) relays cope with such a latency issue in time-constrained applications [63] by avoiding the data decoding stage. As a consequence, AAF relays can be seen as antenna collocated full-duplex devices with an intermediate active amplifying stage. Given that AAF relays do not require extra time frames, coverage and even channel richness can be improved with minor modification to the rest of the network [64].

Nonetheless, cross-talk in AAF relays between transmit and receive elements becomes an issue due to a potential lack of stability. Therefore, due to its closed-loop architecture, stability entails a stringent limit on performance that is to be continuously monitored in practical implementations [63]. The latter makes AAF inconvenient when directional adaptation is critical on interference and energy efficiency grounds in light of the sensible stability.

Recently, nonetheless, such an ancient idea of improving wireless networks by means of relays has been renovated through the concept of low-cost smart mirrors. As a consequence, nowadays' scientific literature is full of appellatives such as intelligent reflecting surfaces [65] (IRS), large intelligent

surfaces [66] (LIS), reconfigurable intelligent surfaces [67] (RIS), passive relaying arrays [68] (PRA), among others.

The underneath idea behind these is to add a control to the characteristics of the radio channel. Even-though such an idea is in a sense revolutionary, a large part of the scientific literature is concentrated on algorithmic and signal processing aspects. Nonetheless, the comprehension of the involved electromagnetic and propagation specificities has not been fully addressed.

More specifically, the term *Digitally Controllable Scatterers* (DCS) is adopted in this project as a way to refer to such a concept. In fact, DCS correspond to the arrangement of a massive amount of inexpensive antenna elements with the objective of capturing and scattering energy in a controllable manner. Such a control method varies widely in the literature [67]; among which PIN-diode and varactor based are popular.

In this context, the project investigates an impedance controlled DCS, although the addressed fundamentals are of a much wider applicability. As a matter of fact, by characterizing DCS in terms of the elements' observed impedance, it is possible to study multiple variants. Nonetheless, with energy efficiency considerations in mind, the current project focuses on the passive and non-dissipative purely reactive alternative.

It is well known from the radar community that, while a mirror is a large reflecting surface with its reflected energy decreasing with the 2^{nd} power of distance, a scatterer is usually considered a near-point object with the scattered energy falling with the 4^{th} power of the distance [5].

Additionally, to the author's knowledge, there is no consolidated concern in the literature about the nature of DCS as scatterers or as mirrors. Although most authors seem to use both terms interchangeably, the common characterization implies they are regarded as scatterers in the sense determined by the radar community.

More notably, the authors of [67] departed from a generalization of the two-ray channel model to argue that DCS would not necessarily obey a path-loss dependence with the fourth power of distance. On the other hand, the authors of [69] concluded there that such a strong power law is probably unavoidable for a practical DCS-like architecture. Nevertheless, no reference to the crucial role of the array near-field region was found as a way to explain such discrepancies.

Consequently, as one contribution of this project, a view that unifies the previous seemingly opposite scattering/reflection dual perspectives is obtained. The latter, as a mean to identify scenarios and show the strong potential behind the DCS concept. In particular, it is shown how physical area and distance aspects become of paramount importance for the operation of such devices.

Chapter 11

Operation of DCS

In light of the so-mentioned relevance of the array near-field in the DCS case, the current chapter illuminates on key aspects regarding the field separation of such antenna arrays.

To begin with, recall from Chapter 1 that the far-field approximation imposes a minimum transmitter-receiver separation distance, notably, so that conventional antenna and propagation models are valid. In fact, the far-field distance increases with the square of the antenna dimension as shown in Sec. 1.1.

11.1 The field decomposition

To be clear, in the standard cell-centric network architecture, the far-field approximation has greatly sufficed as means of characterization. Nevertheless, in the case of DCS, one large issue at stake can be stated as a paradox and, also, related to the fact that it has been mostly conceived as a passively[1] loaded architecture.

Specifically, a DCS must be large as a mean of capturing enough energy; but, as it grows, conventional far-field decomposition mandates that the transmitter and receiver must move away. Consequently, the larger the DCS gets, the farther the transmitter and receiver must be and, therefore, the stronger the path-loss of the transmitter-DCS-receiver link.

Fortunately, this paradox can be circumvented by operating DCS over its near-field[2] region. In order to understand the relevance of its near-field, consider the DCS essentially as the arrangement of multiple antenna elements.

[1]– in the sense that it does not inherently inject energy to the environment.

[2]It must be stressed that we are referring exclusively to the near-field of the array and not to the near-field of the array elementary unit itself.

More specifically, Fig. 11.1 shows the array far-field and the array near-field as disjoint regions. The element near-field is also presented in dark blue for reference. Nonetheless, the element near-field is not considered a region of interest in this work as it is generally too close to the DCS.

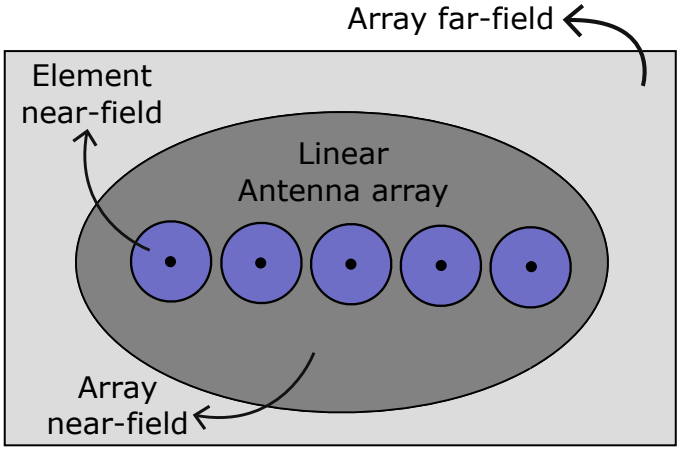

Figure 11.1: Pictorial representation of the field regions of a linear antenna arrangement.

As a matter of fact, any array can be approached close enough to be in the far-field of each elementary unit but not in the far-field of the full array. It is referred here to that particular region of space as the array near-field.

The importance of the array near-field characterization is that a DCS requires large antenna arrangements in the close proximity of users, unlike conventional transmitter-receiver links. Therefore, the term *array near-field* is extensively used here as a way to differentiate it, given its importance in the case of large enough DCS.

In the array far-field, the directional characteristics of DCS naturally decouple from the separation distance. On the other hand, in the array near-field, the previous dependencies are more intricate and call for a different understanding of the problem.

For a simpler insight, recall that Chapter 1 is devoted to the fundamental derivations of the far-field based on elementary Maxwell's equations. In addition, Appendix E formally presents the array near-field characterization via the here-called *generalized array manifold*.

The importance of the generalized array manifold lies on that, as its name suggests, it generalizes the conventional array manifold (also called steering vector) to the array near-field region of interest with the array far-field as a special case. Thus, it allows to characterize DCS on all such regions of operation.

11.2 The Fresnel zone perspective

The aim of this section is to develop an intuition on the interaction of the size of DCS and its near-field region in relation to the Fresnel zones at the DCS interface with the incident and departing radiation.

Let us begin by considering Fig. 11.2 where an unobstructed transmitter-receiver link is presented. Specifically, note the presence of an infinite perfect electrically conducting (PEC) plane parallel to the line joining the transmitter and receiver sides.

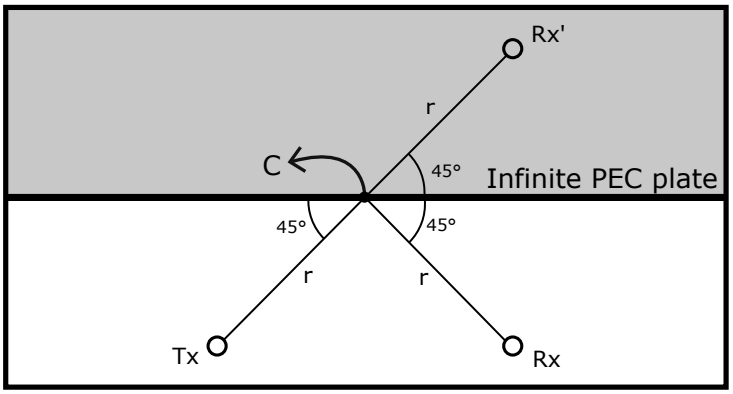

Figure 11.2: Schematic view of the Tx and Rx for mirrored reflection.

Note that, by virtue of the well-known principle of images, the PEC plane can be removed to study separately the line-of-sight and the reflection. In fact, the contribution of the reflection is obtained by mirroring the receiver side and studying the equivalent environment.

Thus, the equivalent setup of Fig. 11.3 is used in what follows to uncover the spatial distribution of the fields around such an interfacing plane. More specifically, it shows the transmitter as well as the mirrored image of the receiver in a perfectly unobstructed environment. Additionally, the first Fresnel zones expose some of the most contributing regions.

The l^{th} Fresnel zone is a region of space whose boundaries are ellipsoids defined as the paths with $(l-1)\,\pi$ and $l\,\pi$ propagation phase-shifts with respect to the shortest central path (containing C in Fig. 11.3) for its inner and outer boundaries, respectively. Additionally, the transmitter and receiver locations are the focal points of such ellipsoids, whose boundaries at the midpoint C can be approximated by [70]:

$$R_l(r) \cong \sqrt{\frac{l\lambda}{2}\, r}\,, \;\; r \gg l\lambda, \tag{11.1}$$

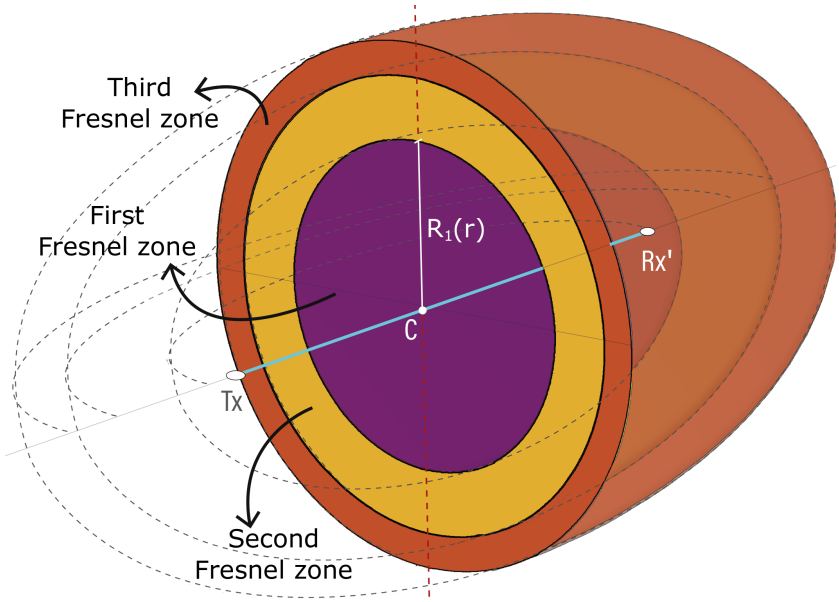

Figure 11.3: View of the equivalent Tx-Rx' scenario for the contribution of the reflector.

where $R_l(r)$ corresponds to the radius of the l^{th} Fresnel zone for the arrangement of Fig. 11.2.

It is well known that the contribution of the first Fresnel zone is the most important one. In order to understand why that is the case, note the following:

1. As shown in Fig. 11.4, the Fresnel zones are defined as ellipsoids with constant propagation phase **relative** to the shortest path between the transmitter and receiver. As a consequence, the closer the transmitter and receiver sides, the smaller the Fresnel zones and vice-versa.

2. The Fresnel zone boundaries get closer for increasing l:

$$R_{l+1}(r) - R_l(r) = \sqrt{r\frac{\lambda}{2}}\,\mathcal{O}\left(\sqrt{l}\right)$$

3. There is a phase difference of 2π between any pair of paths distanced two Fresnel zones from each other.

Therefore, in the extreme of large r, high order Fresnel zones (i.e. higher than one) are significantly weak relative to the first zone and, thus, they do not contribute significantly to the received power; see Item 1.

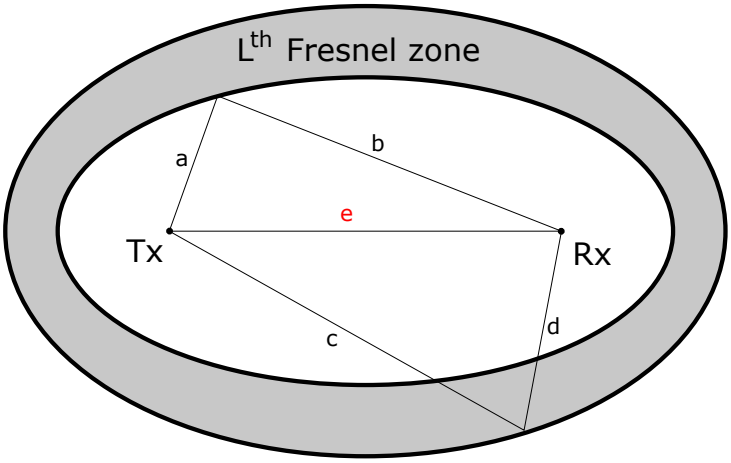

Figure 11.4: Geometrical representation of the l$^{\text{th}}$ Fresnel zone.

On the contrary, for smaller values of r, high order Fresnel zones are almost equally strong due to Item 2 but, at the same time, they interfere destructively with their successive one as a result of Item 3.

In particular, note that even numbered Fresnel zones **always** interfere destructively; as opposed to odd numbered ones that interfere constructively as shown in Fig. 11.5. Thus, the reader might realize that, by a proper dephasing, DCS could in principle outperform free-space propagation.

To continue, it might be useful to look at an infinitely large mirror as spatially integrating the fields over such an infinite aperture. As explained by the equivalence principle over the scenario of Fig. 11.2, such a spatial integration converges to the conventional r^{-2} path-loss dependence. In fact, if the mirror were finite and centered in the shortest transmitter-receiver path, the spatial integration would be truncated. At the same time, due to the Fresnel zone resizing, such a truncation would expose oscillations if the transmitter and receiver were symmetrically moved.

Finally, as a mean of linking DCS' field decomposition and the Fresnel zone perspective, observe from (11.1) (as well as from (E.2) in Appendix E) that $R_{l=1}(r_{\text{FF}}) = D$; with r_{FF} being the low limit of the array far-field and D being the *visible* dimension[3] of the array. In other words, the DCS is being operated in its near-field region when at least the first Fresnel zone of the transmitter-receiver equivalent path (see Fig. 11.3 and Fig. 11.5) is perfectly contained within the DCS itself.

[3]By visible dimension it is referred to the smallest diameter of a circle located on the plane transversal to the direction of propagation and containing the array.

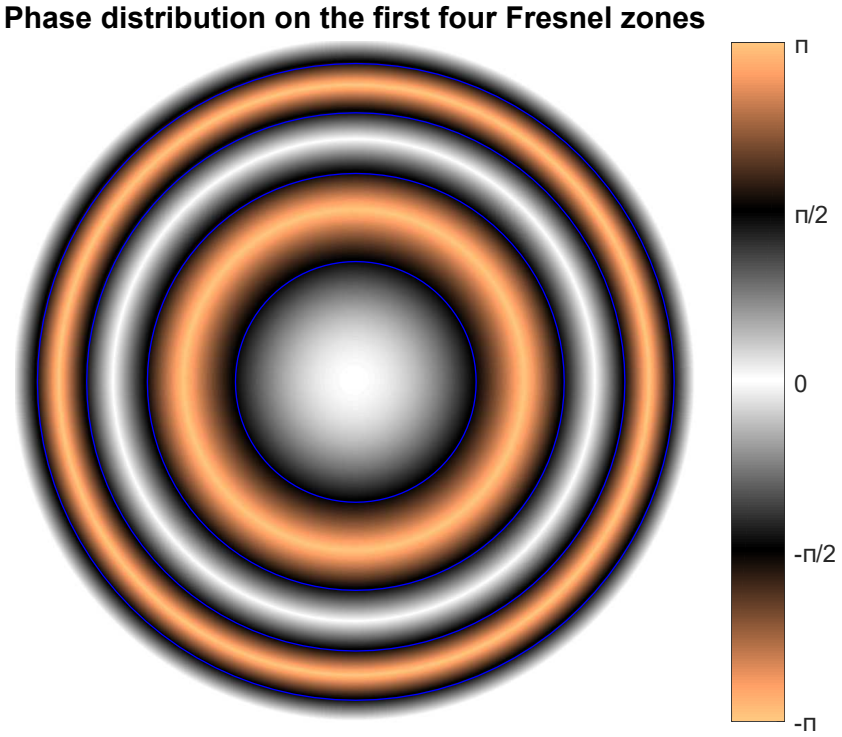

Figure 11.5: Phase distribution on the first four Fresnel zones. White and orange represent constructive and destructive interference, respectively.

Chapter 12

System model

As hinted in the previous chapter, the operation of DCS in the array near-field reveals a behavior different to the one traditionally acknowledged in the DCS and radar literature. In fact, given that such a behavior was not well identified by the beginning of the project, the approach to DCS changed along time. The latter motivated the study of several metrics that better expose the specifics of the array far and near fields.

The current chapter begins by presenting the considered architectures. Subsequently, the derivation of a model for the array far-field metric of RCS is displayed and validated through simulation on an electromagnetic solver[1].

The chapter continues with the derivation of the scattered radiation density as a mean of studying the behavior of DCS in the array near-field. The latter is, likewise, validated by comparison to the EM solver. Indeed, it is shown that the radiation density allows to describe the behavior in the array far-field. Nonetheless, the convenient separability of the directional and distance dependencies of the array far-field is, as a consequence, lost.

Finally, the chapter concludes by presenting the exhaustive signal model for SISO links in the presence of DCS on all such regions of operation.

12.1 Considered architectures

Recall from Chapter 1 that the directional properties of an antenna architecture are determined by the Fourier transform of its current distribution, see (1.19). Thus, the more concentrated a geometry is in one of its major planes, the wider its beam in the corresponding angular coordinate[2].

[1] WIPL-D, *https://wipl-d.com/*

[2] – e.g. explaining why dipoles are omni-directinal radiatiors.

Additionally, the *steerability* of such a beam depends on the available degrees of freedom to control the radiating current distribution. Moreover, dealing with a massive amount of elements, considerations such as their appropriateness to be disposed along a surface become of relevance.

In light of the latter, the following distinct geometries are studied in the current project.

12.1.1 Hexagonal array

To begin with, and because of its directional properties, a dipole-based hexagonal topology is considered. To be precise, its highly circular symmetry makes it a good candidate for narrow-beam yet omni-directionally steerable scattering properties.

Therefore, Fig. 12.1 displays the considered hexagonal architecture. In particular, it is composed of seven hexagons for a total number of 31 elements. Additionally, an interlement spacing of $\lambda/2$ is selected as mean to balance mutual coupling and beam-forming capabilities.

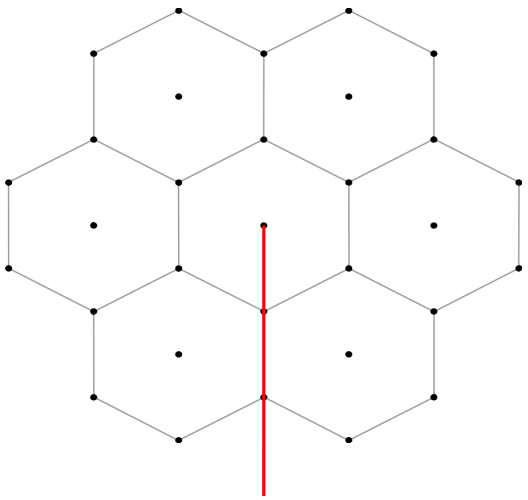

Figure 12.1: Hexagonal element distribution (top view) for the array of dipoles used as DCS. Each sub-cell hexagon radius corresponds to $\lambda/2$.

12.1.2 Ground-plane backed linear array

Note that planar arrangements are convenient for DCS as they can be arranged conformal to surfaces such as walls. In the case of the studied dipole-based architecture, nonetheless, their omni-directional nature comes with a caveat when linearly disposed.

Particularly, as a result of the inability to induce currents on the plane normal to the array, linear arrangements of dipoles present symmetries that become disadvantageous when distributed against a wall.

As a consequence, a linear arrangement of $\lambda/2$-spaced dipoles in front of a finite perfect electrical conducting (PEC) plane is considered as a mean of breaking their symmetry. In fact, as a consequence, the gain from the array ground-plane reflection is further exploited through such a configuration.

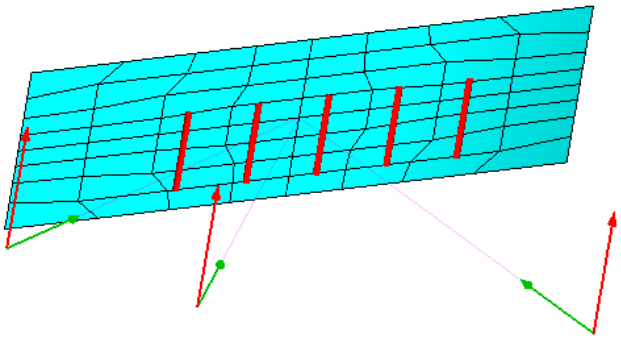

Figure 12.2: Ground-plane backed linear architecture.

12.1.3 Uniform array

Finally, consider a planar and periodic disposition in which $2K_{\mathrm{h}}+1$ horizontal elements and $2K_{\mathrm{v}}+1$ vertical elements arranged as the surface of DCS, for a total of $N=(2K_{\mathrm{h}}+1)(2K_{\mathrm{v}}+1)$ elements.

To be specific, a vertical and horizontal interelement distance of $\lambda/2$ is considered in all cases. Additionally, two different configurations are studied in what follows:

1. A linear DCS with $K_{\mathrm{h}}=10$ and $K_{\mathrm{v}}=0$ for a total number of 21 $\lambda/2$-spaced elements.

2. A planar DCS with $K_{\mathrm{h}}=K_{\mathrm{v}}=10$ for a total number of 441 $\lambda/2$-spaced elements.

In fact, Fig. 12.3 shows a symmetrical setup in which the transmitter and receiver are both a distance r apart from the center of the DCS, which is composed of the so-mentioned periodic structure with a total of N elements.

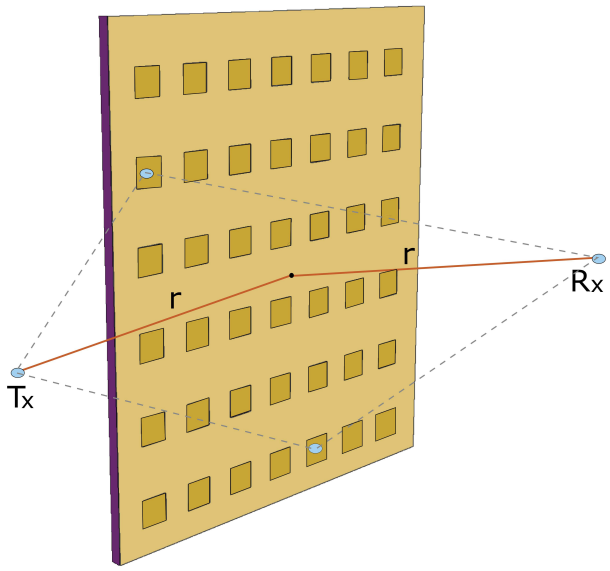

Figure 12.3: Schematic view of Tx, Rx and DCS.

12.2 Far-field characterization

As exposed in Sec. 3.1.2, thin dipoles exhibit a single mode of resonance. As such, their scattering characterization can be realized entirely based on the circuit perspective reviewed in the *Fundamentals* of this document. Although the latter is not the case for general antennas, it allows to obtain a simple yet descriptive model of the scattering dependence with the controllable loads.

Let us begin by considering the problem of reception and elaborate on the induced currents. Subsequently, based of the dependence of the array currents on the reactive loads, the scattered field is derived.

The problem of reception is first solved by the aid of the modified length vector $\boldsymbol{l}_{\mathrm{m}}^{\theta}(\hat{\boldsymbol{r}}_{\mathrm{inc}})$ introduced in Sec. 4.2. Particularly, recall that the array electro-motive force (emf) vector due to a plane wave excitation is given by[3]:

$$\boldsymbol{\mathcal{E}} = \boldsymbol{l}_{\mathrm{m}}^{\theta}(\hat{\boldsymbol{r}}_{\mathrm{inc}})\, E_{\mathrm{inc},\theta}, \tag{12.1}$$

where, on the right hand side, it is assumed that the incident plane wave is θ-polarized, $E_{\mathrm{inc},\theta}$ represents the corresponding θ component of the incident electric field intensity and $\boldsymbol{l}_{\mathrm{m}}^{\theta}(\hat{\boldsymbol{r}}_{\mathrm{inc}})$ corresponds to the θ-polarized modified length vector at the direction of incidence represented by $\hat{\boldsymbol{r}}_{\mathrm{inc}}$.

Particularly, from Sec. 2.1.1 and Sec. 4.2, the modified length vector for

[3]– see Chapter 4 for a comprehensive review of the modified length vector.

an array of vertically oriented half-wave dipoles is given by:

$$\boldsymbol{l}_{\mathrm{m}}^{\theta}(\hat{\boldsymbol{r}}) = \tilde{\boldsymbol{a}}(\hat{\boldsymbol{r}}) \overbrace{\left[-\frac{2}{k}\frac{\cos\left(\frac{\pi}{2}\cos(\theta)\right)}{\sin(\theta)}\right]}^{l_{\mathrm{e},\theta}(\hat{\boldsymbol{r}})}, \tag{12.2}$$

where k corresponds to the wavenumber (i.e. $k = {}^{2\pi}/_{\lambda}$), $\hat{\boldsymbol{r}}$ is a unit norm vector, $\tilde{\boldsymbol{a}}(\hat{\boldsymbol{r}})$ is the array steering vector of Sec. 4.1 and $l_{\mathrm{e},\theta}(\hat{\boldsymbol{r}})$ is the θ-polarized effective length of a dipole introduced in Sec. 2.1.1.

> Note that the modified length vector $\boldsymbol{l}_{\mathrm{m}}^{\theta}(\hat{\boldsymbol{r}})$ consists of the steering vector as effectively impacted by the pattern of the array elementary unit.

Observe that $\hat{\boldsymbol{r}}$ represents a direction specified in terms of the polar and azimuth angles (θ and ϕ, respectively) defined in Fig. 1.4 of Chapter 1.

To be specific, in Cartesian coordinates, $\hat{\boldsymbol{r}}$ is given by:

$$\hat{\boldsymbol{r}}(\theta,\phi) = \sin(\theta)\cos(\phi)\,\hat{\boldsymbol{x}} + \sin(\theta)\sin(\phi)\,\hat{\boldsymbol{y}} + \cos(\theta)\,\hat{\boldsymbol{z}}. \tag{12.3}$$

Even-though (12.1) characterizes the emf at the port of each array element, the current induced at a given dipole will be indirectly impacted by the load set on its neighboring elements due to mutual coupling. As exposed in Sec. 4.4, such an impact is simply characterized via the system admittance matrix, namely through:

$$\boldsymbol{I} = -\overbrace{\left(\boldsymbol{Z} + \jmath\,\mathrm{diag}(\boldsymbol{x}_L)\right)^{-1}}^{\boldsymbol{Y}(\jmath\,\boldsymbol{x}_L)}\boldsymbol{\mathcal{E}}, \tag{12.4}$$

where $\boldsymbol{I} \in C^N$ is the induced current vector and the impact of the reactive loads was included via the admittance matrix $\boldsymbol{Y}(\jmath\,\boldsymbol{x}_L) \in \mathbb{C}^{N\times N}$ with $\boldsymbol{x}_L \in \mathbb{R}^N$ being the vector of reactive loads for a total of N array elements.

From (12.1) and (12.4), it is possible to compute the induced currents due to an incident field on the array. Therefore, the induced array currents (looking *into* the antenna ports) in terms of the incident field and the set of reactive loads can be briefly expressed as:

$$\boldsymbol{I} = -\left(\boldsymbol{Z} + \jmath\,\boldsymbol{X}_L\right)^{-1}\boldsymbol{l}_{\mathrm{m}}^{\theta}(\hat{\boldsymbol{r}}_{\mathrm{inc}})\,E_{\mathrm{inc},\theta}. \tag{12.5}$$

Additionally, as also displayed in Sec. 4.2, the θ polarization of the net field scattered by the array can be expressed in terms of its θ-polarized modified length vector via:

$$E_{\mathrm{scat},\theta}(\boldsymbol{r}_{\mathrm{obs}}) = -\jmath\,k\eta\,\frac{\mathrm{e}^{-\jmath\,kr}}{4\pi r}\,\boldsymbol{I}^{\mathrm{T}}\boldsymbol{l}_{\mathrm{m}}^{\theta}(\hat{\boldsymbol{r}}_{\mathrm{obs}}), \tag{12.6}$$

where η corresponds to the impedance of the medium (i.e. $\eta \approx 120\pi\Omega$ in free space) and r is the observation distance (namely, $\boldsymbol{r}_{\text{obs}} = r\,\hat{\boldsymbol{r}}_{\text{obs}}$).

Based on (12.5) and (12.6) the total scattered field can be given in terms of our quantities of interest. Thus, such a scattered field reads:

$$E_{\text{scat},\theta}(\hat{\boldsymbol{r}}_{\text{inc}}, \hat{\boldsymbol{r}}_{\text{obs}}) = \jmath\, k\eta\, \frac{\mathrm{e}^{-\jmath kr}}{4\pi r} \big[\boldsymbol{l}_{\text{m}}^{\theta}(\hat{\boldsymbol{r}}_{\text{obs}})\big]^{\text{H}} \big(\boldsymbol{Z} + \jmath\, \boldsymbol{X}_L\big)^{-1} \boldsymbol{l}_{\text{m}}^{\theta}(\hat{\boldsymbol{r}}_{\text{inc}})\, E_{\text{inc},\theta}, \quad (12.7)$$

where, to recapitulate, $\boldsymbol{l}_{\text{m}}^{\theta}(\hat{\boldsymbol{r}})$ is the modified length vector of (12.2), $\hat{\boldsymbol{r}}_{\text{inc}}$ is the direction of incidence, $\hat{\boldsymbol{r}}_{\text{obs}}$ the direction of observation and r the observation distance (i.e. $\boldsymbol{r}_{\text{obs}} = r\,\hat{\boldsymbol{r}}_{\text{obs}}$).

Observe that, in (12.7), the transposition of the modified length vector at the direction of observation has been replaced with the Hermitian operator (equivalent to conjugate transposition). The latter is done by defining both $\hat{\boldsymbol{r}}_{\text{obs}}$ and $\hat{\boldsymbol{r}}_{\text{inc}}$ as inward vectors[4], what allows to make use of the Hermitian transpose by properties of the steering vector in (12.2).

Finally, note as well that the scattered electric field intensity of (12.7) is a plane-wave description for the array far-field. A convenient representation can be obtained by removing the dependence of the observation distance through the far-field pattern function $\breve{\boldsymbol{F}}$ of Chapter 3:

$$\breve{\boldsymbol{F}}_{\text{scat}}(\hat{\boldsymbol{r}}_{\text{inc}}, \hat{\boldsymbol{r}}_{\text{obs}}) := \frac{kr}{\mathrm{e}^{-\jmath kr}} \boldsymbol{E}_{\text{scat}}(\hat{\boldsymbol{r}}_{\text{inc}}, \boldsymbol{r}_{\text{obs}}), \quad (3.4)$$

giving for the θ component of the field of interest:

$$\breve{F}_{\text{scat},\theta}(\hat{\boldsymbol{r}}_{\text{inc}}, \hat{\boldsymbol{r}}_{\text{obs}}) = \jmath\, \eta\, \frac{k^2}{4\pi} \big[\boldsymbol{l}_{\text{m}}^{\theta}(\hat{\boldsymbol{r}}_{\text{obs}})\big]^{\text{H}} \big(\boldsymbol{Z} + \jmath\, \boldsymbol{X}_L\big)^{-1} \boldsymbol{l}_{\text{m}}^{\theta}(\hat{\boldsymbol{r}}_{\text{inc}})\, E_{\text{inc},\theta}. \quad (12.8)$$

12.2.1 The RCS and the TSCS

The expression in (12.8) for the far-field pattern function is convenient given that it allows to easily express the radar cross-section (RCS) and can be directly related to the total scattering cross section (TSCS), which is also of interest for the problem of array far-field scattering.

To recall from Chapter 3, the radar cross-section (RCS, denoted σ_b) measures from a receiver's perspective (i.e. direction) the effective capture area that a *target* had, if such a target were isotropically scattering the captured energy from the incident field. The RCS is useful for the radar community and it straightforwardly integrates in the radar equation.

[4]Rigorously, $\hat{\boldsymbol{r}}_{\text{obs}}$ is defined as *leaving* the array, unlike $\hat{\boldsymbol{r}}_{\text{inc}}$ that *approaches* the array.

As shown in Sec. 3.3, the bi-static RCS can be expressed in terms of the far-field pattern function by:

$$\sigma_b(\hat{\boldsymbol{r}}_{\text{inc}}, \hat{\boldsymbol{r}}_{\text{obs}}) = \frac{4\pi}{k^2} \frac{\left|\breve{\boldsymbol{F}}_{\text{scat}}(\hat{\boldsymbol{r}}_{\text{inc}}, \hat{\boldsymbol{r}}_{\text{obs}})\right|^2}{|\boldsymbol{E}_{\text{inc}}|^2}. \tag{3.13}$$

On the other hand, the total scattering cross-section (TSCS, denoted σ_s) is the capture area that relates to the *total* power being scattered in all directions from the incident field, explaining why it is independent of $\hat{\boldsymbol{r}}_{\text{obs}}$.

Computing the TSCS can be computationally expensive as it requires integration over the unit-radius sphere for $\hat{\boldsymbol{r}}_{\text{obs}}$. Nonetheless, with the aid of the forward scattering theorem of Sec. 3.2.2, the TSCS can be straightforwardly written in terms of the far-field pattern function as:

$$\sigma_s(\hat{\boldsymbol{r}}_{\text{inc}}) = \sigma_t(\hat{\boldsymbol{r}}_{\text{inc}}) - \cancelto{0}{\sigma_a(\hat{\boldsymbol{r}}_{\text{inc}})} = \frac{4\pi}{k^2} \Im\left\{ \frac{\breve{F}_{\text{scat},\theta}(\hat{\boldsymbol{r}}_{\text{inc}}, \hat{\boldsymbol{r}}_{\text{inc}})}{E_{\text{inc},\theta}} \right\}, \tag{12.9}$$

where $\Im\{a\}$ corresponds to the imaginary part of a. Note that the forward scattering theorem is relating the sum (σ_t) of the absorbed (σ_a) and total scattered (σ_s) cross-sections to the scattered field in the forward direction, i.e. going through the array. However, $\sigma_a = 0$ as only reactive and non-dissipative loads are assumed here.

To conclude, evaluating the expression of (12.8) in (3.13), the RCS can be readily found to be:

$$\sigma_b(\hat{\boldsymbol{r}}_{\text{inc}}, \hat{\boldsymbol{r}}_{\text{obs}}) = \eta^2 \frac{k^2}{4\pi} \left| \left[\boldsymbol{l}_{\text{m}}^{\theta}(\hat{\boldsymbol{r}}_{\text{obs}})\right]^{\text{H}} \left(\boldsymbol{Z} + \jmath\, \boldsymbol{X}_L\right)^{-1} \boldsymbol{l}_{\text{m}}^{\theta}(\hat{\boldsymbol{r}}_{\text{inc}}) \right|^2. \tag{12.10}$$

Furthermore, evaluating (12.8) in (12.9) and after some algebra, the TSCS can be shortly expressed:

$$\sigma_s(\hat{\boldsymbol{r}}_{\text{inc}}) = \eta \left[\boldsymbol{l}_{\text{m}}^{\theta}(\hat{\boldsymbol{r}}_{\text{inc}})\right]^{\text{H}} \Re\left\{ \left(\boldsymbol{Z} + \jmath\, \boldsymbol{X}_L\right)^{-1} \right\} \boldsymbol{l}_{\text{m}}^{\theta}(\hat{\boldsymbol{r}}_{\text{inc}}), \tag{12.11}$$

where $\Re\{\boldsymbol{A}\}$ corresponds to the real part of any matrix $\boldsymbol{A}$.

12.2.2 Model validation

In light of the derived closed-form expression for the RCS (σ_b), (12.10) is validated in the rest of the current section by comparison to results obtained from a commercially available numerical simulation tool[5].

[5] i.e. WIPL-D, *https://wipl-d.com/*

Specifically, an array of $N = 5$ dipoles distributed as shown in the right bottom of Fig. 12.4 was simulated on such a numerical tool for an arbitrary set of reactive loads. Additionally, in order to compute (12.10), the impedance matrix was obtained by the use of existing analytical expressions to evaluate the mutual coupling of side-by-side arrangements of dipoles as discussed in Sec. 4.3.

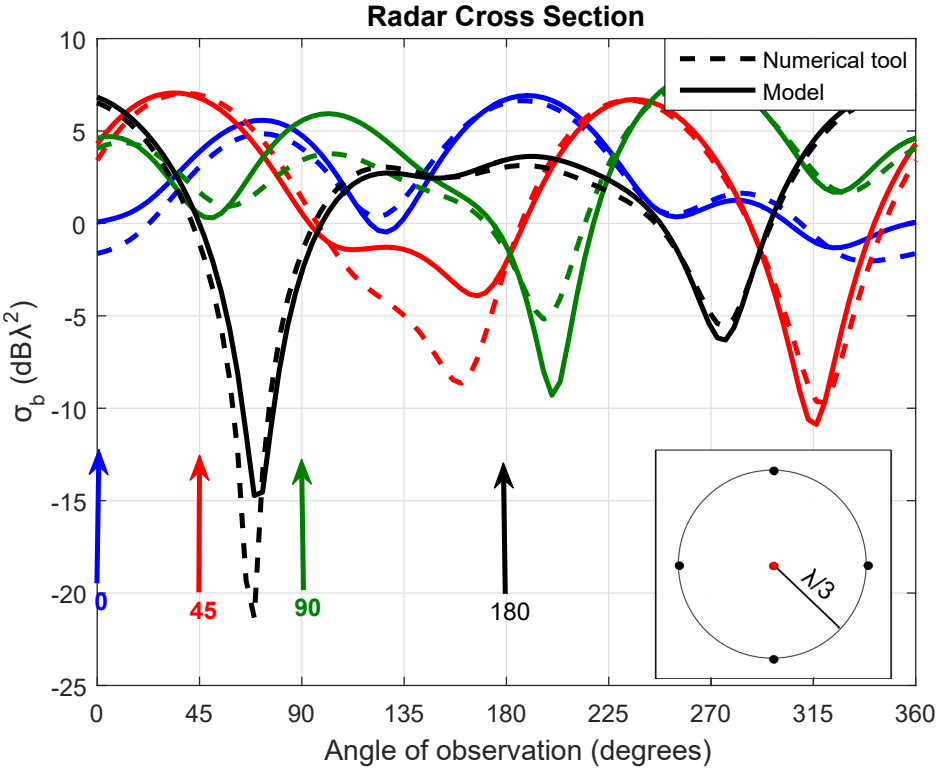

Figure 12.4: RCS vs. ϕ_{obs} for model validation by comparison to WIPL's numerical simulation results. Vertical arrows representing different angles of incidence. Horizontal incidence and observation in all curves.

As it can be observed in Fig. 12.4, there is an overall good correspondence in terms of the values of RCS predicted by the model and, as relevant, on the directions of maximum and minimum scattering. Note the RCS is given in normalized logarithmic units, namely of $10\log_{10}\left(\sigma_b(\hat{\boldsymbol{r}}_{\text{inc}}, \hat{\boldsymbol{r}}_{\text{obs}})\right) - 20\log_{10}(\lambda)$. More specifically, the continuous curves correspond to the evaluation of the model in (12.10), with the colors standing for different directions of incidence.

12.3 Near-field characterization

It must be highlighted that the array far-field approximation of both the reception and transmission processes[6] in (12.7) is captured by the modified length vectors $\boldsymbol{l}_{\mathrm{m}}^{\theta}(\hat{\boldsymbol{r}})$ and, as well, by the implicit distance dependencies.

To begin, as exposed in Appendix. E, an expression valid for the array near-field can be obtained by identifying the steering vector as a special case of the generalized array manifold, the latter of which is given by:

$$\boldsymbol{a}_{\mathrm{p}}(\boldsymbol{r})\big|_{n} := G(\boldsymbol{r}-\boldsymbol{r}_n)\, l_{\mathrm{e,p}}\left(\frac{\boldsymbol{r}-\boldsymbol{r}_n}{|\boldsymbol{r}-\boldsymbol{r}_n|}\right) \forall\, n \leq N, \tag{12.12}$$

where $G(\boldsymbol{r})$ is the free-space Green function of (1.13) and $l_{\mathrm{e,p}}(\hat{\boldsymbol{r}}) = F_{0,\mathrm{p}}(\hat{\boldsymbol{r}})$ correspond, as per (2.3), both to the radiation vector and effective length of the array elementary unit along the p direction of polarization.

> Note that, by the far-field approximation of the Green function (1.16), the generalized array manifold can be related to the modified length vector via:
>
> $$\boldsymbol{a}_{\mathrm{p}}(\boldsymbol{r}) \overset{r \geq r_{\mathrm{FF}}}{=} \frac{\mathrm{e}^{-\jmath kr}}{4\pi r}\, \boldsymbol{l}_{\mathrm{m}}^{\mathrm{p}}(\hat{\boldsymbol{r}}),\ \boldsymbol{r} = r\,\hat{\boldsymbol{r}}, \tag{12.13}$$
>
> with r_{FF} being the array far-field distance in (E.2) of Appendix E.

In what follows, and for simplicity of presentation, we will resort to the assumption that the transmitter antenna is an isotropic source of fields. Consequently, by the identification of (12.13) in (12.7), it can be shown that the scattered electric field intensity at the array near-field reads:

$$E_{\theta}(\boldsymbol{r}_{\mathrm{rx}}, \boldsymbol{r}_{\mathrm{tx}}) = k^2\eta^2\, \boldsymbol{a}_{\theta}^{\mathrm{H}}(\boldsymbol{r}_{\mathrm{rx}})\big(\boldsymbol{Z} + \jmath\, \boldsymbol{X}_L\big)^{-1} \boldsymbol{a}_{\theta}(\boldsymbol{r}_{\mathrm{tx}})\, l_{\mathrm{e},\theta}^{\mathrm{iso}}\, I_{\mathrm{tx}}, \tag{12.14}$$

where $\boldsymbol{r}_{\mathrm{tx}}$ and $\boldsymbol{r}_{\mathrm{rx}}$ are the complete coordinates[7] of the transmitter and receiver relative to the coordinate reference of the controllable scatterer and, as we are dealing with $\hat{\boldsymbol{z}}$-oriented dipoles, only the θ polarization is considered.

Moreover, observe that the dependence on the current feeding the transmitter antenna I_{tx} exposes the role of its respective effective length (i.e. $l_{\mathrm{e},\theta}^{\mathrm{iso}}$).

Note also that $\big(\boldsymbol{Z} + \jmath\, \boldsymbol{X}_L\big)^{-1}$ is a transpose symmetric matrix, which has often (e.g. [67, 66, 65]) been characterized as a diagonal matrix containing complex exponential factors that account for digitally-tunable phase shifts.

---

[6]– those which jointly compose the scattering process.

[7]– as opposed to (12.7) where both the transmitter and receiver are assumed in the array far-field and, therefore, there was only a dependence on the directions of incidence and observation.

12.3.1 Example configuration

In the rest of the current section, a simple but insightful configuration will be evaluated as a mean of exhibiting the appropriateness of the generalized array manifold in describing the behavior of digitally controllable scatterers.

Let us disregard the phenomenon of mutual coupling (i.e. $\boldsymbol{Z} = Z_A\,\mathbb{I}_{N\times N}$) and, additionally, short circuit all elements ($\boldsymbol{x}_L = \mathbf{o}\,\Omega$). Under those circumstances, (12.14) can be simply expressed as:

$$E_\theta(\boldsymbol{r}_{\rm rx}, \boldsymbol{r}_{\rm tx}) = \frac{k^2\eta^2}{Z_A}\boldsymbol{a}_\theta^{\rm H}(\boldsymbol{r}_{\rm rx})\,\boldsymbol{a}_\theta(\boldsymbol{r}_{\rm tx})\,l_{{\rm e},\theta}^{\rm iso}\,I_{\rm tx}. \tag{12.15}$$

If, additionally, we assume that the DCS is provided with θ-polarized isotropic elementary units, i.e. $l_{{\rm e},\theta}(\hat{\boldsymbol{r}}) = l_{{\rm e},\theta}^{\rm iso}$ in (12.12), the expression (12.15) can be simplified further to:

$$E_\theta(\boldsymbol{r}_{\rm rx}, \boldsymbol{r}_{\rm tx}) = \frac{k^2\eta^2}{Z_A}\big[l_{{\rm e},\theta}^{\rm iso}\big]^3 I_{\rm tx}\sum_{n=1}^{N} G\big(\boldsymbol{r}_{\rm rx}-\boldsymbol{r}_n\big)\,G\big(\boldsymbol{r}_{\rm tx}-\boldsymbol{r}_n\big), \tag{12.16}$$

where $G(\boldsymbol{r})$ is, once more, the Green function of (1.13).

Even-though the expression in (12.16) corresponds to the array near-field electric field intensity, it characterizes the linear combination of element-wise far-field sources. Thus, the scattered radiation density (in units of power per unit area) can be related simply to its scattered field through $\mathcal{P} = (2\eta)^{-1}|\boldsymbol{E}|^2$.

In particular, introducing $r_{{\rm t},n}{:=}|\boldsymbol{r}_{\rm tx}-\boldsymbol{r}_n|$ and $r_{{\rm r},n}{:=}|\boldsymbol{r}_{\rm rx}-\boldsymbol{r}_n|$ as the distances from the transmitter and receiver to every DCS element, respectively, the radiation density of the scattered field reads:

$$\mathcal{P}(\boldsymbol{r}_{\rm rx}, \boldsymbol{r}_{\rm tx}) = \frac{k^4\eta^3}{2|Z_A|^2}\big|l_{{\rm e},\theta}^{\rm iso}\big|^6|I_{\rm tx}|^2\left|\sum_{n=1}^{N}\frac{{\rm e}^{-\jmath kr_{{\rm r},n}}}{4\pi r_{{\rm r},n}}\,\frac{{\rm e}^{-\jmath kr_{{\rm t},n}}}{4\pi r_{{\rm t},n}}\right|^2. \tag{12.17}$$

Observe that, although we have assumed hypothetical isotropic elements, expression (12.17) allows to analyze the radiation density as regards the Tx and Rx locations relative to the element's disposition, i.e. $\boldsymbol{r}_n\,\forall\, n \leq N$.

In light of the loading condition under evaluation ($\boldsymbol{x} = \mathbf{o}\,\Omega$), the setup of Sec. 12.1.3 (with the transmitter and receiver positioned symmetrically as required by the Snell-Decartes law) is evaluated. The latter, in order to expose a case in which waves are naturally interfering constructively[8] towards the receiver side.

[8] In fact, they don't interfere perfectly (as it will be clear later) but such a setup serves to illustrate the point the author wants to make.

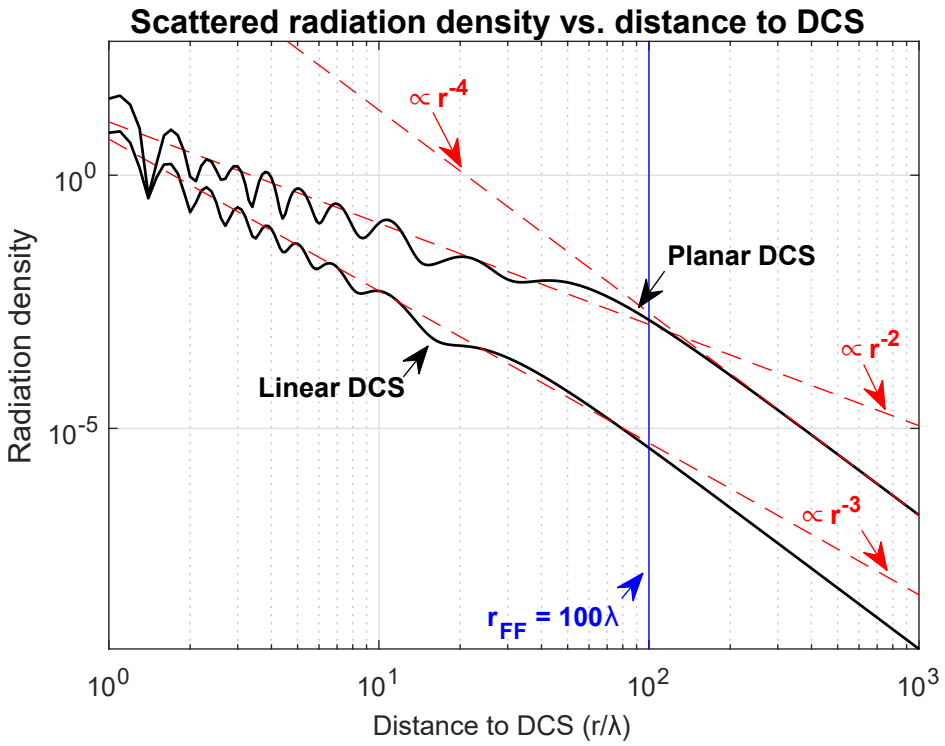

Figure 12.5: Radiation density (power per unit area) of the field scattered by DCS versus distance for the setup of Fig. 12.3.

As observed in Fig. 12.5, the radiation density clearly exposes different behaviors for the array near-field ($r < r_{\text{FF}}$) and its far-field region ($r > r_{\text{FF}}$).

More specifically, the array far-field region unsurprisingly exposes a path-loss related to r^{-4} in both the linear and planar configurations. The operation over such a sector can be characterized through metrics used in the radar community (such as the radar cross section) as done in Sec. 12.2. Nonetheless, the latter is clearly not the most interesting region of operation for the DCS.

On the other hand, the array near-field exposes a seemingly oscillatory behavior around r^{-2} and r^{-3} for the planar and linear configurations, respectively. The latter is explained by the fact that, through its finite number of antenna elements, the DCS is sampling the field at discrete points in space.

In particular, the oscillations illustrate the constructive and destructive interference caused by the complex exponential terms in (12.17) as induced by the Green function. Moreover, as exposed in Sec. 11.2, the oscillations can also be understood as the constructive and destructive interference of interacting Fresnel zones as.

12.3.2 Model validation

In order to validate the model of DCS, as well as the Fresnel zone intuition of Sec. 11.2, a very simple scenario is studied using WIPL-D.

More specifically, a two port setup composed of two vertically-polarized half-wave dipoles (acting as the transmitter and receiver) in the presence of a finite metal plate are simulated. The latter is appropriate given that the example configuration of Sec. 12.3.1 could be considered as its discrete approximation.

The size of the simulated plate is fixed to $10\lambda \times 10\lambda$ and the dipoles are positioned symmetrically (45° from the vector normal to the plate's surface) a distance r; exactly like for the DCS setup of Sec. 12.3.1.

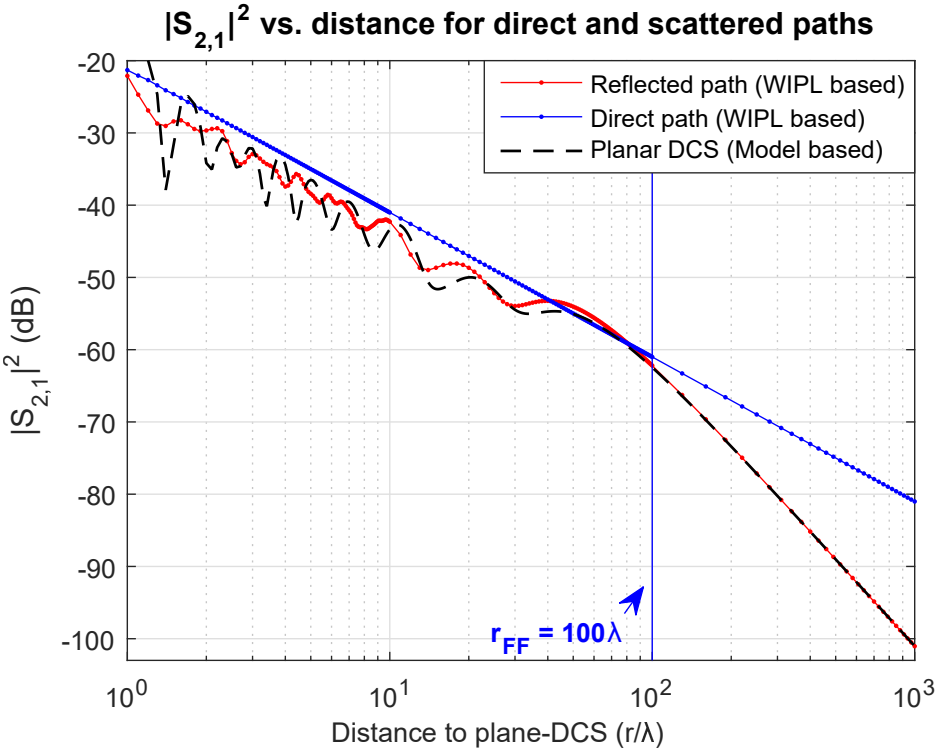

Figure 12.6: $|S_{2,1}|^2$ quantifying the power received through reflection from a finite metal plate vs. transmitter-receiver distance.

In particular, the power transmission coefficient $|S_{2,1}|^2$ was computed as DCS is mostly operating over the near-field of the plate (i.e. making far-field metrics such as the radar cross section invalid).

Additionally, as the aforementioned setup computes the net (direct plus reflected) fields, separate simulations (with and without the plate) were done in order to subtract the the direct path and obtain the reflected contribution.

As observed in Fig. 12.6, the reflected path exhibits the expected oscillatory behavior at the near-field region of the plate. Note as well that, in spite of the discrete nature of the DCS, the model is able to capture with fair accuracy the details of its continuous-equivalent[9]. Nonetheless, it can be shown that the WIPL numerical results and the model converge when the element density of the model is increased within such a confined region of space.

12.4 The SISO signal model

The author would to like to briefly summarize the implications of this chapter for the transmitter-receiver SISO signal model derived in Chapter 5.

For simplicity, in what follows, we will assume single-element, single-polarization and isotropic transmitter and receiver sides. On the other hand, the DCS elementary unit can be arbitrarily chosen as its impact is accounted for in the generalized array manifold of (12.12).

It must also be added that the multi-antenna transmitter/receiver (i.e. MIMO) extension can be straightforwardly envisaged by virtue of the superposition principle. Nonetheless, its mathematical representation can easily become cumbersome as a result of the multi-location dependencies[10].

Therefore, relying on the DCS model derivation of section 12.2, the complete link-level system model can be shown equivalent to:

$$y = \left(\tilde{h}_{\mathrm{tr}}\, G(r_{\mathrm{tr}}) + \tilde{h}_{\mathrm{DCS}}\, \boldsymbol{a}_{\mathrm{p}}^{\mathrm{H}}(\boldsymbol{r}_{\mathrm{rx}}) \big(\boldsymbol{Z} + \jmath\, \boldsymbol{X}_L \big)^{-1} \boldsymbol{a}_{\mathrm{p}}(\boldsymbol{r}_{\mathrm{tx}}) \right) s + n, \qquad (12.18)$$

where s, y and n are the conventional input, output and additive white Gaussian noise at the receiver side, respectively; $G(r)$ is the free-space Green function of (1.13); r_{tr} is the shortest-path transmitter-receiver distance; $\boldsymbol{r}_{\mathrm{tx}}$ and $\boldsymbol{r}_{\mathrm{rx}}$ are the transmitter and receiver locations relative to DCS' coordinate reference, respectively; and $\boldsymbol{a}_{\mathrm{p}}(\boldsymbol{r}) \in \mathbb{C}^N$ is the generalized array manifold of (12.12) (see Appendix E for its derivation) polarized along p for an N element DCS.

Additionally, in (12.18), $\tilde{h}_{\mathrm{tr}}$ and $\tilde{h}_{\mathrm{DCS}}$ are spatially-flat channel coefficients that represent a scenario in which all links (transmitter-receiver, transmitter-DCS and DCS-receiver) are dominated by their line-of-sight components.

[9] Naturally, DCS' curve was vertically shifted to make it coincide with WIPL's results in the array far-field as, in particular, the multiplicative coefficients in (12.17) cannot be determined for hypothetical isotropic antennas.

[10] – in particular for the case in which the array elementary units of the transmitter and receiver sides are not isotropic anymore.

These channel coefficients also absorb all physical quantities that are not of concern for link-level characterization; allowing to introduce the dimensionless *signal* denomination[11].

Note that, if the direct transmitter-receiver link is either obstructed or suffers from strong multi-path propagation, its impact shall be embedded onto $\tilde{h}_{\mathrm{tr}}$. On the other hand, we do not expect $\tilde{h}_{\mathrm{DCS}}$ to be greatly impacted by multi-path propagation as higher order scattering might strongly attenuate contributions other than the line-of-sight ones.

[11]– where a signal is simply defined as an observable change in a quantity.

Chapter 13

Performance evaluation

The previous chapter presented different models to characterize the operation of DCS on its array far-field and near-field regions. Notably, the RCS and the scattered radiation density were used as means of studying their behavior on both of these regions, respectively.

Observe that, while the RCS plays a simple role in the modified link budget of Sec. 3.4, the operation of DCS in the array near-field region does not allow for such a simplified description. Particularly, as exposed in Sec. 12.3, the free-space-like behavior of the planar DCS at the array near-field comes at the expense of more intricate multi-location dependencies[1].

The current chapter displays the performance obtained with the architectures considered in Sec. 12.1. To begin, the ability of the hexagonal dipole-based architecture to *steer* the incident radiation by means of scattering is analyzed through an SPSA-based RCS maximization algorithm.

Subsequently, the dependence of the RCS on the number of antenna elements is studied on the ground-plane backed linear arrangement. Additionally, it is shown that the model given use (based on the principle of images to describe the impact of the ground plane) is accurate if such a ground plane is allowed to extend beyond the array.

To conclude, the uniform planar arrangement is adopted by the end of the chapter to expose the exciting potential of operating DCS in its near-field region. More specifically, it is shown that it is possible to outperform free-space propagation under completely obstructed links through smart dephasing. Such an idea was hinted on in Sec. 11.2. As it shown here, the latter results in a dependence with the fourth power of the distance which, paradoxically, outperforms the conventional free-space propagation.

[1]– namely, of the transmitter and receiver relative to every element in the DCS.

13.1 Steerability of hexagonal architecture

Recall that the far-field RCS of Sec. 12.2 characterizes DCS and plugs into the modified link budget of Sec. 3.4. Additionally, observe that the expression in (12.10) shows an inverse quadratic dependence of the RCS with the set of reactive loads in $\boldsymbol{x}_L$.

Hence, in what follows, an iterative algorithm relying on an approximation of the gradient of (12.10) is adopted. Particularly, as stressed in the second part of this document, the simultaneous perturbation stochastic approximation method (SPSA) emerges due to its computational complexity, which is related to two cost function evaluations per iteration step regardless the number of parameters.

The SPSA method is known for its good behavior on cost functions having multiple extrema [71]. Moreover, SPSA does not require the availability of an analytic expression for the gradient, which makes it appropriate given the non-trivial dependence of (12.10) on $\boldsymbol{x}_L$. Consequently, SPSA is adopted here in order to give a solution to the optimization problem:

$$\sigma_b^{\max}(\hat{\boldsymbol{r}}_{\text{inc}}, \hat{\boldsymbol{r}}_{\text{scat}}) = \max_{\boldsymbol{x}_L} \quad \sigma_b(\boldsymbol{x}_L \,|\hat{\boldsymbol{r}}_{\text{inc}}, \hat{\boldsymbol{r}}_{\text{scat}}), \tag{13.1}$$

where $\hat{\boldsymbol{r}}_{\text{scat}}$ is the direction towards which the incident wave from $\hat{\boldsymbol{r}}_{\text{inc}}$ is intended to be scattered.

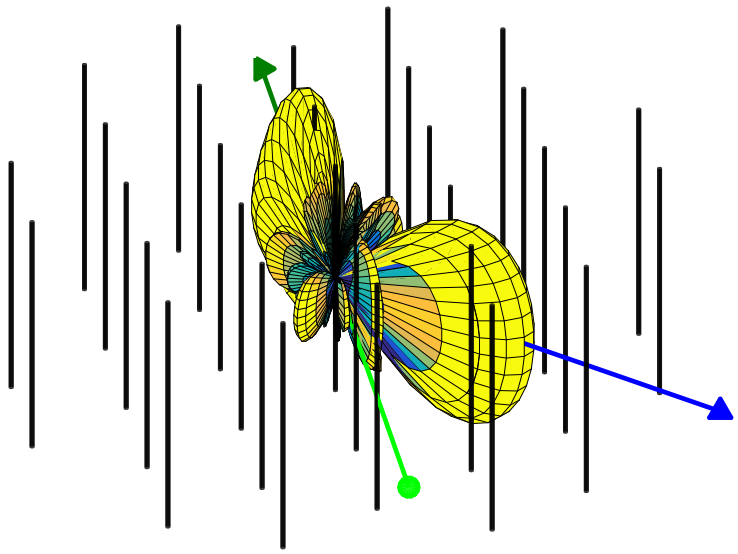

Figure 13.1: 3D representation of the hexagonal architecture and the result $\sigma_b(\hat{\boldsymbol{r}}_{\text{inc}}, \hat{\boldsymbol{r}}_{\text{obs}})$ solving (13.1) for $\hat{\boldsymbol{r}}_{\text{inc}} = \hat{\boldsymbol{r}}(\phi = 0°,\, \theta = 90°)$ and $\hat{\boldsymbol{r}}_{\text{scat}} = \hat{\boldsymbol{r}}(\phi = 45°, \theta = 90°)$.

Note that in (13.1), as well as in (12.4), $\boldsymbol{x}_L$ is defined as a real vector representing the reactive load onto every element. Consequently, the problem in (13.1) can be solved in the $\mathbb{R}$-domain in spite of the complex nature of the quantities involved in the evaluation of $\sigma_b(\boldsymbol{x}_L\,|\hat{\boldsymbol{r}}_{\text{inc}}, \hat{\boldsymbol{r}}_{\text{scat}})$.

As a particular example, observe Fig. 13.1 for the RCS obtained by solving (13.1) for scattering in the directions given by the arrows. In fact, there exists strong scattering in intended direction of scattering (blue arrow) and in the direction going through the array (dark green arrow). The latter is a consequence of the forward scattering theorem of Sec. 3.2.2.

Furthermore, as can be observed in Fig. 12.1, the considered array is highly circularly symmetric. Consequently, as mentioned, the directional behavior of the array is expected to be rotationally invariant. Hence, without loss of generality, the direction of incidence is fixed to $\hat{\boldsymbol{r}}_{\text{inc}} = \hat{\boldsymbol{r}}(\phi = 0°, \theta = 90°)$ in what follows.

Particularly, Fig. 13.2 shows that the maximum RCS of (13.1) is mostly contained within a band of 3 dB wide above 20 dBλ^2 for intended scattering towards most of the horizontal plane, except for the regions highlighted in blue. Moreover, a maximum RCS of 26 dBλ^2 is achieved in the 40° wide region around the forward scattering direction.

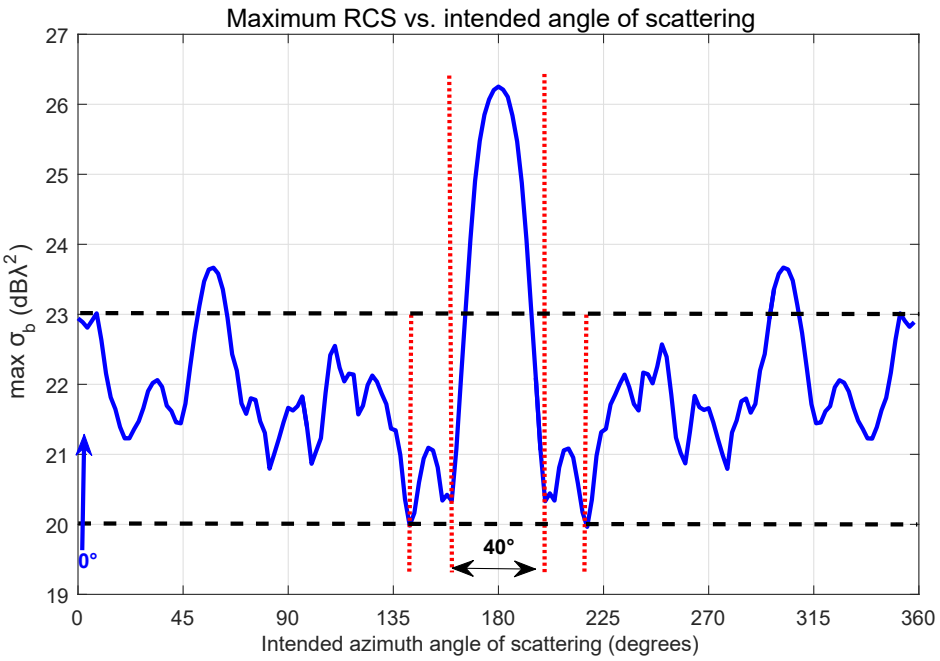

Figure 13.2: Maximum RCS in dBλ^2 vs. intended azimuth angle of scattering obtained by solving (13.1).

13.2 The mirrored linear architecture

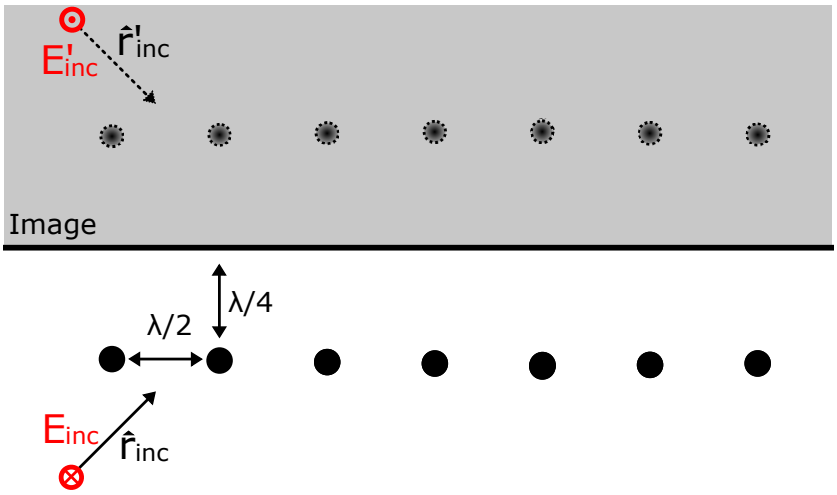

Figure 13.3: Top view of the considered array geometry, the incident field and the mirrored images involved in the scattering characterization of the proposed linear architecture.

Let us consider Fig. 13.3 where a linear arrangement in front of an infinite ground plane creates a mirrored image of the original environment (shown on top of the figure with a gray background).

As explicitly shown, in order to comply with the image principle, we shall mirror the incident wave. Nonetheless, such a mirrored image implies the array is provided with a total of $2N$ elements, all of which must be analyzed strictly as *physical* elements from the EM perspective. More notably, all such elements contribute to the scattered field and are excited by both the original and mirrored incident fields. Likewise, the adopted mutual coupling characterization is still applicable.

As a consequence, the modified length vector and impedance matrix are $\boldsymbol{l}_{\mathrm{m}}^{\theta}(\hat{\boldsymbol{r}}) \in \mathbb{C}^{2N}$ and $\boldsymbol{Z} \in \mathbb{C}^{2N\times 2N}$ in the mirrored case. In particular, the expression in (12.8) for the far-field pattern function is valid if the previous considerations are accounted for, resulting to:

$$\breve{F}_{\mathrm{scat},\theta}(\hat{\boldsymbol{r}}_{\mathrm{inc}},\hat{\boldsymbol{r}}_{\mathrm{obs}}) = \jmath\,\eta\,\frac{k^2}{4\pi}\left[\boldsymbol{l}_{\mathrm{m}}^{\theta}(\hat{\boldsymbol{r}}_{\mathrm{obs}})\right]^{\mathrm{H}}\left(\boldsymbol{Z}+\jmath\,\boldsymbol{X}_L\right)^{-1}\left[\boldsymbol{l}_{\mathrm{m}}^{\theta}(\hat{\boldsymbol{r}}_{\mathrm{inc}}) - \boldsymbol{l}_{\mathrm{m}}^{\theta}(\hat{\boldsymbol{r}}'_{\mathrm{inc}})\right] E_{\mathrm{inc},\theta} \tag{13.2}$$

where $\hat{\boldsymbol{r}}'_{\mathrm{inc}}$ stands for a unitary vector representing the mirrored direction of incidence, and the minus sign at the right-hand-side factor is a result of applying the image principle to the incident electric field intensity $\boldsymbol{E}_{\mathrm{inc}}$[2].

[2]– observe that $\boldsymbol{E}_{\mathrm{inc}}$ and $\boldsymbol{E}'_{\mathrm{inc}}$ are pointing in opposite directions in Fig. 13.3.

Accordingly, the respective RCS can be shortly expressed:

$$\sigma_b(\hat{\boldsymbol{r}}_{\text{inc}}, \hat{\boldsymbol{r}}_{\text{obs}}) = \eta^2 \frac{k^2}{4\pi} \left| \left[\boldsymbol{l}^{\theta}_{\text{m}}(\hat{\boldsymbol{r}}_{\text{obs}})\right]^{\text{H}} \left(\boldsymbol{Z} + \jmath\, \boldsymbol{X}_L\right)^{-1} \left[\boldsymbol{l}^{\theta}_{\text{m}}(\hat{\boldsymbol{r}}_{\text{inc}}) - \boldsymbol{l}^{\theta}_{\text{m}}(\hat{\boldsymbol{r}}'_{\text{inc}})\right] \right|^2. \quad (13.3)$$

In specific, phenomena such as diffraction by the edges cause the *distortion* of the mirrored image and the effective impairment of the infinite ground plane model in (13.3) with respect to the finite ground plane case, specially for grazing angles of incidence. Moreover, in practice, the presence of a ground plane contributes to the *structural mode* of the scattering reviewed in Sec. 3.1.1. Therefore, the previous model only characterizes the respective *antenna mode*[3].

In fact, WIPL is used in what follows to compute the array far-field scattered by the geometry of Fig. 12.2 in short circuit condition (i.e. $\boldsymbol{x}_L = \mathbf{o}$). Moreover, the contribution of the finite ground plane alone is subsequently subtracted in order to evaluate the ability of (13.3) to characterize the antenna mode contribution.

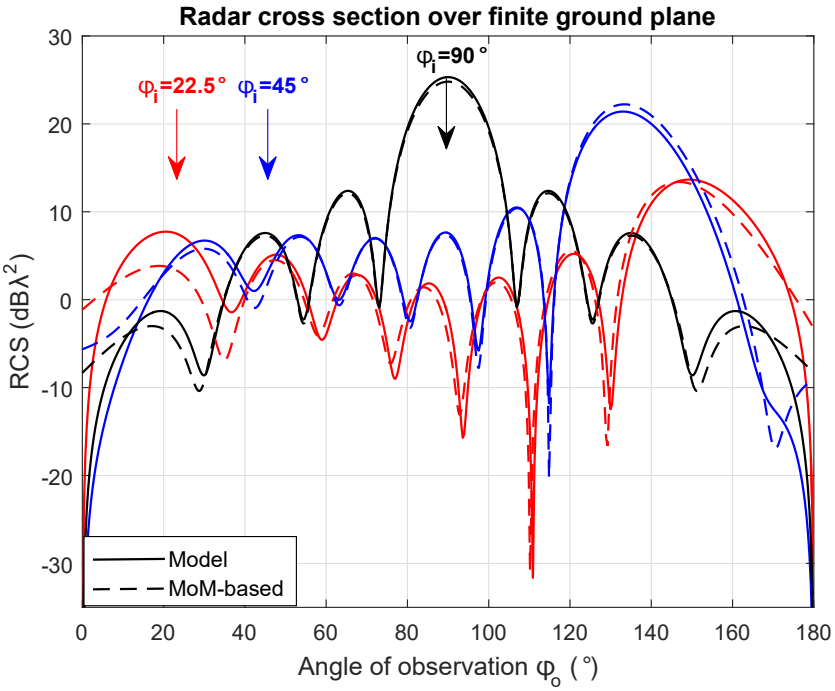

Figure 13.4: Comparison of the RCS as obtained via the derived model and a MoM-based tool (WIPL) over the finite ground plane of Fig. 12.2 for 22.5°, 45° and 90° of incidence. N = 7 elements in all cases.

[3]Specifically, if the structural mode is referenced to high impedance, see Sec. 3.1.1.

As observed in Fig. 13.4, there exists good agreement between the infinite ground plane model and the simulation results from WIPL with degradation towards 0° and 180° (where the missing field-contribution because of the finite ground plane gets more significant). The latter applies both for incidence and observation.

Therefore, it is shown that the model derived for the case of an infinite ground plane gives a good description for a wide range of angles as long as some excess ground plane is allowed (in the considered case an excess of λ in the width and $\lambda/2$ in the height).

The dependence with the number of elements

Recall that the RCS in (13.3) depends quadratically on the far-field pattern function of (13.2).

Let us now consider that, if there is no coupling ($\boldsymbol{Z} = z_{\mathrm{dip}}\,\mathbb{I}_N$) and all elements are short-circuited, (13.3) reduces to:

$$\sigma_b^{\mathrm{NC}}(\hat{\boldsymbol{r}}_{\mathrm{inc}}, \hat{\boldsymbol{r}}_{\mathrm{obs}}) = \frac{k^2\eta^2}{4\pi\,|z_{\mathrm{dip}}|^2}\left|\left[\boldsymbol{l}_{\mathrm{m}}^{\theta}(\hat{\boldsymbol{r}}_{\mathrm{obs}})\right]^{\mathrm{H}}\left[\boldsymbol{l}_{\mathrm{m}}^{\theta}(\hat{\boldsymbol{r}}_{\mathrm{inc}}) - \boldsymbol{l}_{\mathrm{m}}^{\theta}(\hat{\boldsymbol{r}}'_{\mathrm{inc}})\right]\right|^2,$$

whose quadratic expansion contains N^2 terms. Consequently, we could expect the RCS to grow with the square of the number of elements if mutual coupling is sufficiently weak.

As a mean of verifying if the latter is the case of the $\lambda/2$-spaced architecture under consideration, the RCS was computed using the model (13.3) and WIPL with respect to N for such a loading condition, i.e. $\boldsymbol{x}_L = \mathbf{o}$.

It is observed in Fig. 13.5, when contrasted to the reference curve in red, that the RCS (corresponding to the one at the directions given by the Snell-Descartes' law) does indeed grow with the square of the number of elements regardless mutual coupling and the direction of incidence.

Note, in particular, that there is good agreement between the results obtained from the model and the MoM-based simulation tool for the considered array sizes having fixed the excess ground plane equally for all cases.

13.3 Outperforming free-space propagation

Recall from Sec. 11.2 that the contribution of even numbered Fresnel zones is always destructive. As a consequence, if such zones are contained within the DCS[4], a dense enough architecture might in principle be able to compensate for their destructive nature.

[4]Namely, if it is being operated in the array near-field region.

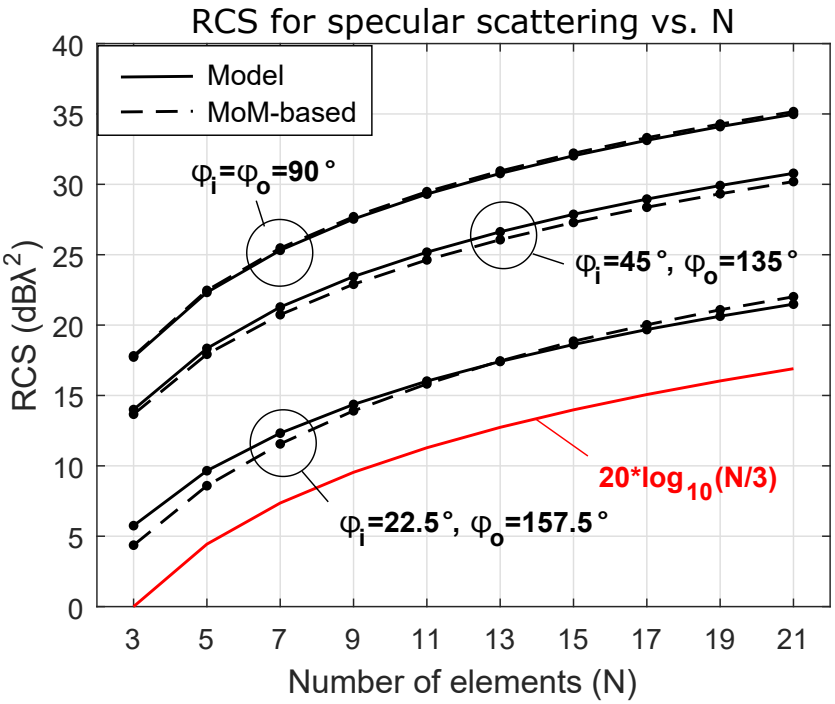

Figure 13.5: RCS for specular scattering vs. N for 22.5°, 45° and 90° of incidence. Red curve shown as a reference of a quadratic dependence on N.

As a matter of fact, the model for the radiation density in Sec 12.3 allows to transparently predict the maximum obtainable power for an architecture-specific digitally controllable scatterer.

In particular, a smart-enough DCS would, at its best, compensate for the path-related phase shift, giving for the received radiation density:

$$\mathcal{P}_{\max}(\boldsymbol{r}_{\rm rx}, \boldsymbol{r}_{\rm tx}) = \frac{k^4\eta^3}{2|Z_A|^2}\left|l^{\rm iso}_{{\rm e},\theta}\right|^6 |I_{\rm tx}|^2 \left|\sum_{n=1}^{N} \frac{1}{4\pi r_{{\rm r},n}} \frac{1}{4\pi r_{{\rm t},n}}\right|^2, \tag{13.4}$$

using the notation of (12.17) to represent all involved quantities.

> Observe that, in the array far-field, short-circuiting all elements ($\boldsymbol{x}_L = \mathbf{o}$) is optimal for Snell-Decartes' scattering if mutual coupling is absent. The latter is in agreement with the example configuration of Sec. 12.3.1.

As a consequence, the radiation density of the smart-dephasing enabled DCS is compared against such an example configuration in what follows.

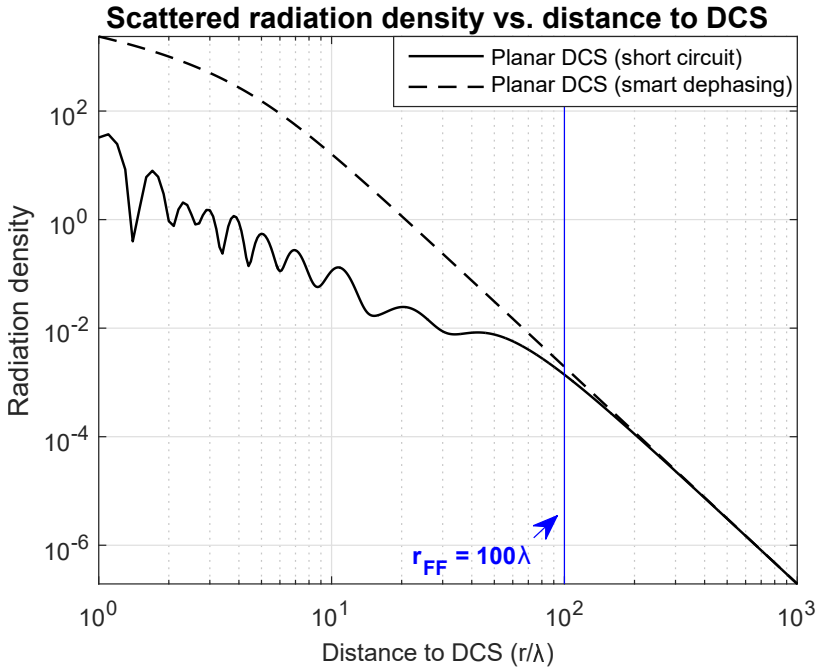

Figure 13.6: Radiation density (power per unit area) of the field scattered by the DCS with smart dephasing versus distance.

In fact, Fig. 13.6 shows that the path-loss related to the smart-dephasing technique does not only deviate from the previously observed r^{-2} but, on the contrary, it exposes a behavior that outperforms free-space propagation for a completely-obstructed (NLOS) transmitter-receiver link. Also, as predicted from Sec. 11.2, the lack of oscillations in the dashed curve results from the removal of the (even-numbered) Fresnel zone destructive nature.

It must be stressed that the considered element density was enough in Fig. 13.6 to maintain a constant log-log increase of the receive power with decreasing distance[5] for a significant part of the array near-field region.

More importantly, the behavior observed in Fig. 13.6 implies that the dependence with the fourth power of the distance is a consequence of the constant phase along the DCS. Typically, the latter manifests at the array far-field region where, as explained in Sec 11.2, the DCS is fully contained within the first Fresnel zone. Nonetheless, as explored in this section, such a behavior can be artificially enforced in the array near-field.

Therefore, while a r^{-4} dependence at large distance may be seen as poor, it turns out to be advantageous when approaching the DCS below r_{FF} as a way to avoid the transition to the (inferior) r^{-2} regime.

[5]– to be specific, of 40 dB per decade.

Chapter 14

Perspectives

This project studied the use of alternative antenna architectures as a way to improve the usability of the spatial domain of wireless channels. An electromagnetic perspective was adopted in order to create an intuition behind the most relevant phenomena at stake. Additionally, the emphasis was placed on the derivation of simple and representative mathematical models by means of exposing the interface between signals and fields. In specific, ESPAR antennas and digitally controllable scatterers were assessed with looks at improving energy efficiency at a low cost.

On the one hand, ESPAR antennas have caused interest for many decades because of their low cost and adaptable radiation properties. As future work, issues such as scalability call for attention in light of their intrinsic reliance on mutual coupling. Additionally, the performance evaluation of the proposed algorithms on a fabricated ESPAR is relevant to display their real potential.

On the other hand, digitally controllable scatterers are at a very early stage but, as shown by the interest these have gained in the recent years, they reveal a promising future for intelligently controlled environments. Indeed, the concept of DCS challenges the conventional paradigm of communication problems. Finally, some open questions on DCS are related to their impact over rich multi-path channels, the configuration of the loads in the array near-field and the contribution of the structural mode.

Part IV

Appendices

Appendix A

Frobenius-ℓ_2 $\boldsymbol{x}$ norm equivalence

Given the role of $\|\mathbf{Z}_{\text{ESPAR}}^{-1}\boldsymbol{X}\|_F$ as a measure of ε in (4.11) and (4.13), its squared norm will be re-expressed by considering the structure of $\mathbf{Z}_{\text{ESPAR}}$ for the architecture of interest (namely, that of Fig. 7.2).

Consequently, let us remind the reader that such a square Frobenius norm can be written as:

$$\begin{aligned}
\|\mathbf{Z}_{\text{ESPAR}}^{-1}\boldsymbol{X}\|_F^2 &= \text{tr}\Big(\mathbf{Z}_{\text{ESPAR}}^{-1}\boldsymbol{X}\big[\mathbf{Z}_{\text{ESPAR}}^{-1}\boldsymbol{X}\big]^{\text{H}}\Big) \\
&= \text{tr}\Big(\mathbf{Z}_{\text{ESPAR}}^{-1}\boldsymbol{X}\boldsymbol{X}^{\text{H}}\mathbf{Z}_{\text{ESPAR}}^{-\text{H}}\Big) \\
&= \text{tr}\Big(\boldsymbol{X}^{\text{H}}\mathbf{Z}_{\text{ESPAR}}^{-\text{H}}\mathbf{Z}_{\text{ESPAR}}^{-1}\boldsymbol{X}\Big) \\
\therefore \|\mathbf{Z}_{\text{ESPAR}}^{-1}\boldsymbol{X}\|_F^2 &= \text{tr}\Bigg(\begin{bmatrix}0\\ \boldsymbol{x}\end{bmatrix}\begin{bmatrix}0 & \boldsymbol{x}^{\intercal}\end{bmatrix} \circ \mathbf{Z}_{\text{ESPAR}}^{-\text{H}}\mathbf{Z}_{\text{ESPAR}}^{-1}\Bigg), \qquad \text{(A.1)}
\end{aligned}$$

where the relation between the complex parasitic load matrix $\boldsymbol{X}$ and the real reactive load vector $\boldsymbol{x}$ of (7.9) was given use.

Moreover, the last step in (A.1) follows from the entry-wise product (also known as Hadamard product) property of:

$$\boldsymbol{D}_{\boldsymbol{y}}\boldsymbol{A}\boldsymbol{D}_{\boldsymbol{y}}^{\text{H}} = \boldsymbol{y}\boldsymbol{y}^{\text{H}} \circ \boldsymbol{A},$$

where $\boldsymbol{D}_{\boldsymbol{y}}$ is a diagonal matrix with $\boldsymbol{y}$ on its main diagonal and $\boldsymbol{A}$ is any matrix of appropriate size.

Note that the trace operator depends exclusively on the components of the main diagonal of the matrix it is operated over. Note also that, unlike the regular matrix product, the Hadamard product does not introduce dependencies among different components. Particularly, it can be easily shown

with respect to the diagonal of the matrices in (A.1) that:

$$\left[\begin{bmatrix}0\\ \boldsymbol{x}\end{bmatrix}\begin{bmatrix}0 & \boldsymbol{x}^{\intercal}\end{bmatrix}\right]_{i,i} = \begin{cases}0,\ i=1\\ \left|[\boldsymbol{x}]_i\right|^2,\ \forall\, i\neq 0\end{cases},$$

$$\left[\mathbf{Z}_{\text{ESPAR}}^{-\text{H}}\mathbf{Z}_{\text{ESPAR}}^{-1}\right]_{i,i} = \sum_{j=1}^{N}\left|\left[\mathbf{Z}_{\text{ESPAR}}^{-1}\right]_{i,j}\right|^2,\ \forall\, i=1,\,2,\,\ldots,\,N,$$

with $\left[\boldsymbol{A}\right]_{i,j}$ representing the component on the i$^{\text{th}}$ row and j$^{\text{th}}$ column of matrix $\boldsymbol{A}$. Thus, (A.1) can be rewritten as:

$$\begin{aligned}\|\mathbf{Z}_{\text{ESPAR}}^{-1}\boldsymbol{X}\|_F^2 &= \text{tr}\left(\begin{bmatrix}0\\ \boldsymbol{x}\end{bmatrix}\begin{bmatrix}0 & \boldsymbol{x}^{\intercal}\end{bmatrix}\circ\mathbf{Z}_{\text{ESPAR}}^{-\text{H}}\mathbf{Z}_{\text{ESPAR}}^{-1}\right)\\ &= \sum_{i=1}^{N}\left(\left[\begin{bmatrix}0\\ \boldsymbol{x}\end{bmatrix}\begin{bmatrix}0 & \boldsymbol{x}^{\intercal}\end{bmatrix}\right]_{i,i}\left[\mathbf{Z}_{\text{ESPAR}}^{-\text{H}}\mathbf{Z}_{\text{ESPAR}}^{-1}\right]_{i,i}\right)\\ &= \sum_{i=2}^{N}\boldsymbol{x}|_i^2\sum_{j=1}^{N}\left|\left[\mathbf{Z}_{\text{ESPAR}}^{-1}\right]_{i,j}\right|^2\\ \therefore\ \|\mathbf{Z}_{\text{ESPAR}}^{-1}\boldsymbol{X}\|_F^2 &= \boldsymbol{x}^{\intercal}\boldsymbol{D}\boldsymbol{x},\end{aligned}\tag{A.2}$$

where $\boldsymbol{D}\in\mathbb{R}^{N-1\times N-1}$ is a diagonal matrix obtained by extracting the lower-right diagonal from $\mathbf{Z}_{\text{ESPAR}}^{-\text{H}}\mathbf{Z}_{\text{ESPAR}}^{-1}$, i.e.

$$\boldsymbol{D} := \begin{bmatrix}\sum_{i=1}^{N}\left|[\mathbf{Z}_{\text{ESPAR}}^{-1}]_{2,i}\right|^2 & \cdots & 0\\ \vdots & \ddots & \vdots\\ 0 & \cdots & \sum_{i=1}^{N}\left|[\mathbf{Z}_{\text{ESPAR}}^{-1}]_{N,i}\right|^2\end{bmatrix}.$$

Finally, for the circularly symmetric architecture of Fig. 7.2, it can be verified that

$$\sum_{j=1}^{N}\left|\left[\mathbf{Z}_{\text{ESPAR}}^{-1}\right]_{m,j}\right|^2 = \sum_{j=1}^{N}\left|\left[\mathbf{Z}_{\text{ESPAR}}^{-1}\right]_{n,j}\right|^2\forall\, m\neq n\neq 1,$$

meaning that $\boldsymbol{D} = k\,\mathbb{I}_{N-1}$. The latter is a result of the fact that from every peripheral element's perspective the array looks identical. Consequently, the expression in (A.2) can be further reduced for the circular architecture of interest to:

$$\therefore\ \|\mathbf{Z}_{\text{ESPAR}}^{-1}\boldsymbol{X}\|_F^2 = k\|\boldsymbol{x}\|^2,\tag{A.3}$$

where k is any of the components on the diagonal of $\boldsymbol{D}$ as previously defined.

Appendix B

Matrix M spectral decomposition

Note that the operation carried out by the symmetric matrix $\boldsymbol{M}$ in (8.8) is a linear transformation that can be alternatively expressed via (8.9) as:

$$\tilde{\boldsymbol{x}} = \boldsymbol{Q}\big(\mu \mathbb{I}_{N-1} - \boldsymbol{\Lambda}\big)^{-1}\boldsymbol{Q}^{\intercal}\,\Re\{\boldsymbol{B}_{\text{ap}}{}^{\text{H}}\boldsymbol{h}\boldsymbol{h}^{\text{H}}\boldsymbol{a}_{\text{ap}}\}, \tag{B.1}$$

where, reminding the reader, $\boldsymbol{Q}\boldsymbol{\Lambda}\boldsymbol{Q}^{\intercal}$ is the eigen decomposition of $\Re\{\boldsymbol{B}_{\text{ap}}{}^{\text{H}}\boldsymbol{h}\boldsymbol{h}^{\text{H}}\boldsymbol{B}_{\text{ap}}\}$, $\boldsymbol{Q} \in \mathbb{R}^{(N-1)\times(N-1)}$ and $\boldsymbol{\Lambda} \in \mathbb{R}^{(N-1)\times(N-1)}$.

Moreover, note that:

$$\begin{aligned}\Re\{\boldsymbol{v}z\} &= \Re\{\boldsymbol{v}\}\Re\{z\} - \Im\{\boldsymbol{v}\}\Im\{z\},\\ \Re\{\boldsymbol{v}\boldsymbol{v}^{\text{H}}\} &= \Re\{\boldsymbol{v}\}\Re\{\boldsymbol{v}\}^{\intercal} + \Im\{\boldsymbol{v}\}\Im\{\boldsymbol{v}\}^{\intercal},\end{aligned}$$

meaning that, defining $\boldsymbol{v} := \boldsymbol{B}_{\text{ap}}{}^{\text{H}}\boldsymbol{h}$ and $z := \boldsymbol{h}^{\text{H}}\boldsymbol{a}_{\text{ap}}$, it can be shown that

$$\begin{aligned}\Re\{\boldsymbol{B}_{\text{ap}}{}^{\text{H}}\boldsymbol{h}\boldsymbol{h}^{\text{H}}\boldsymbol{a}_{\text{ap}}\} &\in \text{colspace}\Big(\Re\{\boldsymbol{B}_{\text{ap}}{}^{\text{H}}\boldsymbol{h}\boldsymbol{h}^{\text{H}}\boldsymbol{B}_{\text{ap}}\}\Big),\\ \therefore \Re\{\boldsymbol{B}_{\text{ap}}{}^{\text{H}}\boldsymbol{h}\boldsymbol{h}^{\text{H}}\boldsymbol{a}_{\text{ap}}\} &\perp \text{nullspace}\Big(\Re\{\boldsymbol{B}_{\text{ap}}{}^{\text{H}}\boldsymbol{h}\boldsymbol{h}^{\text{H}}\boldsymbol{B}_{\text{ap}}\}\Big).\end{aligned}$$

Therefore, as a result of such an orthogonality,

$$\boldsymbol{Q}^{\intercal}\,\Re\{\boldsymbol{B}_{\text{ap}}{}^{\text{H}}\boldsymbol{h}\boldsymbol{h}^{\text{H}}\boldsymbol{a}_{\text{ap}}\} = \begin{bmatrix}\boldsymbol{Q}_R^{\intercal}\,\Re\{\boldsymbol{B}_{\text{ap}}{}^{\text{H}}\boldsymbol{h}\boldsymbol{h}^{\text{H}}\boldsymbol{a}_{\text{ap}}\}\\ \mathbf{o}_{N-3}\end{bmatrix} \tag{B.2}$$

where $\boldsymbol{Q}_R \in \mathbb{R}^{(N-1)\times 2}$ corresponds to selecting, from the previously defined matrix $\boldsymbol{Q}$, the eigenvectors forming a basis for the column space of $\Re\{\boldsymbol{B}_{\text{ap}}{}^{\text{H}}\boldsymbol{h}\boldsymbol{h}^{\text{H}}\boldsymbol{B}_{\text{ap}}\}$, i.e. the ones related to non-zero eigenvalues.

As a consequence, the expression in (B.1) is equivalent to:

$$\tilde{\boldsymbol{x}} = \boldsymbol{Q}_R \begin{bmatrix} \frac{1}{\mu-\lambda_1} & 0 \\ 0 & \frac{1}{\mu-\lambda_2} \end{bmatrix} \boldsymbol{Q}_R^{\mathsf{T}} \Re\{{\boldsymbol{B}_{\text{ap}}}^{\text{H}} \boldsymbol{h}\boldsymbol{h}^{\text{H}} \boldsymbol{a}_{\text{ap}}\}, \tag{8.10}$$

for $\lambda_1 \neq \lambda_2 \neq 0$.

Particularly, when $\lambda_1 = \lambda_2 = \lambda \neq 0$, the solution (8.10) becomes:

$$\tilde{\boldsymbol{x}} = \frac{1}{\mu - \lambda} \Re\{{\boldsymbol{B}_{\text{ap}}}^{\text{H}} \boldsymbol{h}\boldsymbol{h}^{\text{H}} \boldsymbol{a}_{\text{ap}}\},$$

in which case $\tilde{\boldsymbol{x}}$ lies in the span of $\Re\{{\boldsymbol{B}_{\text{ap}}}^{\text{H}} \boldsymbol{h}\boldsymbol{h}^{\text{H}} \boldsymbol{a}_{\text{ap}}\}$ and the only role of μ is fixing the norm of $\boldsymbol{x}$, via the constraint of problem (8.4), regardless λ.

Appendix C

Least mean squares

To begin with, the method of least mean squares (LMS) is a widely known method that, as its name suggests, works by minimizing the ensemble square of an error signal, i.e. e in Fig. 8.2. In particular:

$$e^{\text{LMS}} := \mathbb{E}_{\boldsymbol{x}}\{|y - \hat{y}(\boldsymbol{g})|^2\}. \tag{C.1}$$

As we are interested in finding the model parameter $\boldsymbol{g}$ that minimizes (C.1), we can proceed by taking its gradient:[1]

$$\nabla_{\boldsymbol{g}}\, e^{\text{LMS}} = \mathbb{E}_{\boldsymbol{x}}\{-\boldsymbol{x}_e\, \overline{y} + \boldsymbol{x}_e \boldsymbol{x}_e^{\intercal} \boldsymbol{g}\}. \tag{C.2}$$

From the stationary points of (C.1) (i.e. the values of $\boldsymbol{g}$ for which (C.2) is equal to $\mathbf{o}$) and defining: the covariance matrix, the cross-covariance vector and their estimators [2]

$$\boldsymbol{R}_{xx} := \mathbb{E}_{\boldsymbol{x}}\{\boldsymbol{x}_e \boldsymbol{x}_e^{\intercal}\} \approx \frac{1}{L} \sum_{l=0}^{L} \boldsymbol{x}_e(l) \boldsymbol{x}_e^{\intercal}(l),$$

$$\boldsymbol{p}_{xy} := \mathbb{E}_{\boldsymbol{x}}\{\boldsymbol{x}_e\, \overline{y}\} \approx \frac{1}{L+1} \sum_{l=0}^{L} \boldsymbol{x}_e(l)\, \overline{y}(l),$$

the $\boldsymbol{g}$ that minimizes (C.1) can be readily found to be the Wiener-Hopf equation [73]:

$$\boldsymbol{g}_{\text{LMS}} = \boldsymbol{R}_{xx}^{-1}\, \boldsymbol{p}_{xy}. \tag{C.3}$$

As we are in fact interested in a sample-per-sample update (notice that $\boldsymbol{g}_{\text{LMS}}$ as from (C.3) based on estimates requires a batch of L samples), an

[1] As $\boldsymbol{g}$ is complex and (C.1) is real (i.e. non-complex-analytic), the gradient is defined slightly different to the purely real case. See [72] for details.

[2] L stands for the number of realizations used to compute such estimates.

stochastic single-step variant of LMS is considered instead. In particular, through (C.2), an stochastic update of $\boldsymbol{g}$ via the most recent sample can be written as:

$$\begin{aligned}\boldsymbol{g}(n+1) &= \boldsymbol{g}(n) - \eta\, \nabla_{\boldsymbol{g}}\, e^{\mathrm{LMS}}(n) \\ &\approx \boldsymbol{g}(n) + \eta\, \boldsymbol{x}_e(n) \overbrace{\big(\overline{y}(n) - \boldsymbol{x}_e^{\intercal}(n)\boldsymbol{g}(n)\big)}^{\overline{e}(n)},\end{aligned}$$

where, as it can be observed, $\boldsymbol{g}$ has now a discrete time index n and its update requires only the product of the currently evaluated $\boldsymbol{x}_e$, the conjugate of the error signal $e(n)$ and the step size η.

Note that the shown update is sensitive to scaling of the input vector $\boldsymbol{x}_e(n)$. To deal with this, the normalized LMS has been proposed. Particularly, this variation of LMS is realized by normalizing the updating term, namely:

$$\boldsymbol{g}(n+1) = \boldsymbol{g}(n) + \eta\, \frac{\boldsymbol{x}_e(n)}{\boldsymbol{x}_e^{\intercal}(n)\boldsymbol{x}_e(n)}\, \overline{e}(n), \tag{C.4}$$

with the step size η chosen within $0 \leq \eta \leq 2$ such that it does not compromise the convergence of the algorithm in the mean [73, 74].

Appendix D

Recursive least squares

The recursive least squares (RLS) method, on the other hand, is acknowledged for its convergence speed. As opposed to LMS where the minimization is carried out in the ensemble of the process, RLS minimizes the weighted square of the error signal over the past, i.e.

$$e^{\mathrm{RLS}} := \sum_{l=0}^{n} \lambda^{n-l} |\, y(l) - \hat{y}(l)|^2, \tag{D.1}$$

where $0 \leq \lambda \leq 1$ is a exponential weighting parameter known as the forgetting factor and n corresponds to the most recent time index.

Note that, on the one hand, if $\lambda = 1$ in (D.1) all past samples are equally weighted making it appropriate for fixed environments. On the other hand, if $\lambda < 1$ the more recent the sample is, the bigger its contribution with $\lambda = 0$ on the extreme where only the most recent (n^{th}) sample is taken into account.

The stationary points of (D.1) (being real valued) can be obtained by equating to zero its partial derivatives with respect to the conjugate coefficients $\overline{\boldsymbol{g}}$, namely [72]:

$$\frac{\partial\, e^{\mathrm{RLS}}}{\partial\, \overline{\boldsymbol{g}}} = \sum_{l=0}^{n} \lambda^{n-l} \big[\boldsymbol{x}_e(l) \boldsymbol{x}_e^{\mathsf{T}}(l) \boldsymbol{g} - \boldsymbol{x}_e(l) \overline{y}(l) \big] = \mathbf{o}.$$

Furthermore, by defining the weighted-approximate covariance matrix and cross-covariance vector:

$$\boldsymbol{R}_{\lambda,xx}(n) := \sum_{l=0}^{n} \lambda^{n-l} \boldsymbol{x}_e(l) \boldsymbol{x}_e^{\mathsf{T}}(l),$$

$$\boldsymbol{p}_{\lambda,xy}(n) := \sum_{l=0}^{n} \lambda^{n-l} \boldsymbol{x}_e(l) \overline{y}(l),$$

the optimal parameters $\boldsymbol{g}$ that minimize (D.1) at time n can be shown to be:

$$\boldsymbol{g}_{\mathrm{RLS}}(n) = \boldsymbol{R}_{\lambda,xx}^{-1}(n)\, \boldsymbol{p}_{\lambda,xy}(n). \tag{D.2}$$

Moreover, the recursive denomination in RLS comes from the expansion of the summation in the so-defined weighted covariance matrix and cross-covariance vector. In particular, it can be shown that

$$\boldsymbol{p}_{\lambda,xy}(n) = \lambda\, \boldsymbol{p}_{\lambda,xy}(n-1) + \boldsymbol{x}_e(n)\, \overline{y}(n), \tag{D.3}$$
$$\boldsymbol{R}_{\lambda,xx}(n) = \lambda\, \boldsymbol{R}_{\lambda,xx}(n-1) + \boldsymbol{x}_e(n)\boldsymbol{x}_e^{\intercal}(n), \tag{D.4}$$

meaning that the matrix inverse in (D.2) can be avoided, by recursively expressing it as a rank-1 update of itself through the matrix inverse lemma and (D.4), namely:

$$\boldsymbol{R}_{\lambda,xx}^{-1}(n) = \frac{1}{\lambda}\left(\mathbb{I}_N - \frac{\boldsymbol{R}_{\lambda,xx}^{-1}(n-1)\, \boldsymbol{x}_e(n)\boldsymbol{x}_e^{\intercal}(n)}{\lambda + \boldsymbol{x}_e^{\intercal}(n)\boldsymbol{R}_{\lambda,xx}^{-1}(n-1)\boldsymbol{x}_e(n)}\right) \boldsymbol{R}_{\lambda,xx}^{-1}(n-1).$$

Subsequently, by defining the so-called gain vector:

$$\boldsymbol{q} := \frac{1}{\lambda + \boldsymbol{x}_e^{\intercal}(n)\boldsymbol{R}_{\lambda,xx}^{-1}(n-1)\boldsymbol{x}_e(n)}\, \boldsymbol{R}_{\lambda,xx}^{-1}(n-1)\boldsymbol{x}_e(n), \tag{D.5}$$

the inverse covariance matrix update can be re-expressed as:

$$\boldsymbol{R}_{\lambda,xx}^{-1}(n) = \frac{1}{\lambda}\Big(\mathbb{I}_N - \boldsymbol{q}\boldsymbol{x}_e^{\intercal}(n)\Big)\boldsymbol{R}_{\lambda,xx}^{-1}(n-1). \tag{D.6}$$

In particular, (D.6) allows, after some algebra on (D.3), to write the recursion of the optimal $\boldsymbol{g}(n)$ in (D.2) as a function of itself at time $n-1$ as:

$$\boldsymbol{g}(n) = \boldsymbol{g}(n-1) + \boldsymbol{q}\, \underbrace{\Big(\overline{y}(n) - \boldsymbol{x}_e^{\intercal}(n)\boldsymbol{g}(n-1)\Big)}_{\overline{\alpha}(n)}, \tag{D.7}$$

where $\alpha(n)$ is known as the a priori error given that it is computed based on $\boldsymbol{g}(n-1)$.

Therefore, to summarize, the recursion for $\boldsymbol{g}$ requires to obtain $\boldsymbol{q}$ based on $\boldsymbol{R}_{\lambda,xx}^{-1}(n-1)$ with (D.5), followed by updating $\boldsymbol{g}(n)$ based on (D.7). Finally, the matrix $\boldsymbol{R}_{\lambda,xx}^{-1}(n)$, as required by the following recursion, is updated using $\boldsymbol{q}$ through (D.6).

Note that the RLS algorithm, giving an exact solution, is able to replace the computationally expensive matrix inverse of $\boldsymbol{R}_{\lambda,xx}$ in (D.2), which would be $\mathcal{O}(N^3)$, with operations that are $\mathcal{O}(N^2)$ of complexity in big O notation.

Appendix E

Derivation of the generalized array manifold

In spite of the attention given in the *Fundamentals* to the *array far-field*, a new quantity (so-called *generalized* array manifold) is introduced as a way to characterize arrays in a different region of operation. More specifically, the generalized array manifold describes arrays operating in the region referred to as the array near-field.

As seen in the third *part* of this manuscript, the array near-field characterization is fundamental to the understanding of digitally controllable scatterers in their most interesting region of operation.

Recall that the far-field approximation imposes a minimum transmitter-receiver separation distance, notably, so that conventional antenna and propagation models are valid. In fact, the far-field distance increases with the

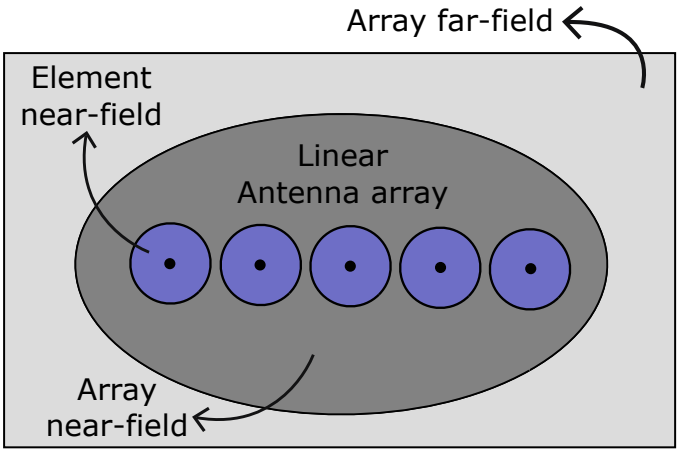

Figure E.1: Field regions of a linear antenna arrangement.

square of the largest dimension of the antenna as shown in Sec. 1.1.

In particular, observe the array regions as pictorially represented in Fig. E.1. Note that, as depicted there, the element near-field is in general much smaller than the array near-field[1].

Consider the problem of determining the electric field intensity $\boldsymbol{E}$ at the array near-field region resulting from a multi-antenna arrangement as source of fields. As it will be clear in what follows, the characterization at the array near-field region captures the behavior over the array far-field as a particular case. Thus, allowing to describe the behavior on both such regions of interest. Nonetheless, as it is too close to the array, the element near-field (dark blue region in Fig. E.1) will not be accounted for throughout this work.

Therefore, as a first step, reconsider the source current density of a multiple antenna architecture of (4.1). Based on Chapter 1, the magnetic potential vector for such an architecture can be written as[2]:

$$\boldsymbol{A}(\boldsymbol{r}) = \mu \int_{V'} \sum_{n=1}^{N} I_n \, \boldsymbol{J}_0(\boldsymbol{r}' - \boldsymbol{r}_n) \, G(\boldsymbol{r} - \boldsymbol{r}') \, d^3\boldsymbol{r}', \tag{E.1}$$

where V' should include all the sources represented by (4.1).

Recall that the most commonly used antenna metrics (directivity, gain, antenna aperture, etc.) give an approximately correct characterization for the far-field region of the antenna or antenna array under consideration.

Consequently, note from Sec. 1.1 that the limit of the array and element far-field regions are given in terms of the largest dimension of the array D and its elementary unit D_0 by:

$$r_{\text{FF}} = \frac{2D^2}{\lambda}, \; r_{\text{FF}}^{\text{elem}} = \frac{2D_0^2}{\lambda}, \tag{E.2}$$

where $\lambda = {}^{c}\!/_{f}$ corresponds to the wavelength and c to the speed of light.

Thus, the far-field approximation of the Green function of (1.16) cannot be used in (E.1) to compute $\boldsymbol{A}$ over the array near-field region of interest (roughly, the region described by $r_{\text{FF}}^{\text{elem}} < |\boldsymbol{r}| < r_{\text{FF}}$).

On the other hand, in the following, we will resort to a different strategy as a mean of approximating it at such a region of interest.

---

[1]– particularly in massive antenna arrangements.

[2]– observe that we don't resort directly to the radiation vector as this one would inherently solve the problem in the array far-field region.

The far-field condition revisited

If the integration and summation are swapped in (E.1), such an expression can be rewritten as:

$$\boldsymbol{A}(\boldsymbol{r}) = \mu \sum_{n=1}^{N} I_n \int_{V''} \boldsymbol{J}_0(\boldsymbol{r}'')\, G\big((\boldsymbol{r}-\boldsymbol{r}_n)-\boldsymbol{r}''\big)\, d^3\boldsymbol{r}'', \tag{E.3}$$

where the substitution $\boldsymbol{r}'' = \boldsymbol{r}' - \boldsymbol{r}_n$ was used and accounted for in the volume of integration.

Note that, if $\boldsymbol{J}_0(\boldsymbol{r})$ is concentrated in a closed domain over $\boldsymbol{r} \in \mathbb{R}^3$ and $|\boldsymbol{r}_n - \boldsymbol{r}_m| > d_{\max}\, \forall n \neq m$ with $d_{\max}$ being the largest dimension of such a closed domain, (E.3) can be expressed as:

$$\boldsymbol{A}(\boldsymbol{r}) = \mu \sum_{n=1}^{N} I_n \int_{V_n''} \boldsymbol{J}_0(\boldsymbol{r}'')\, G\big((\boldsymbol{r}-\boldsymbol{r}_n)-\boldsymbol{r}''\big)\, d^3\boldsymbol{r}'', \tag{E.4}$$

where $V'' = \bigcup_{n=1}^{N} V_n''$ with V_n'' tightly enclosing the domain over which the current distribution $\boldsymbol{J}_0(\boldsymbol{r}-\boldsymbol{r}_n)$ is concentrated and, more importantly, such regions are disjoint, i.e. $V_i'' \bigcap V_j'' = \varnothing\ \forall\, i \neq j$.

The importance of the previous result lies on that, while the far-field Green function cannot be used in (E.3), it can be used over the separate domains of integration in (E.4). The latter, as long as $|\boldsymbol{r}-\boldsymbol{r}_n| > r_{\text{FF}}^{\text{elem}}\, \forall n$ with $r_{\text{FF}}^{\text{elem}}$ given by (E.2).

In particular, the expression (E.4) can be largely simplified by identifying the radiation vector of (1.19) through:

$$\boldsymbol{A}(\boldsymbol{r}) = \sum_{n=1}^{N} I_n \overbrace{\mu \underbrace{\frac{\mathrm{e}^{-\jmath k|\boldsymbol{r}-\boldsymbol{r}_n|}}{4\pi|\boldsymbol{r}-\boldsymbol{r}_n|}}_{G(\boldsymbol{r}-\boldsymbol{r}_n)} \boldsymbol{F}_0\left(\frac{\boldsymbol{r}-\boldsymbol{r}_n}{|\boldsymbol{r}-\boldsymbol{r}_n|}\right)}^{\boldsymbol{A}_0^{\text{FF}}(\boldsymbol{r}-\boldsymbol{r}_n)}, \tag{E.5}$$

where $\boldsymbol{A}_0^{\text{FF}}(\boldsymbol{r})$ is identified as the far-field approximation of the magnetic potential vector of the array elementary unit, $G(\boldsymbol{r})$ as the Green function in (1.13) and $\boldsymbol{F}_0(\hat{\boldsymbol{r}})$ is the radiation vector of the elementary array unit of Chapter 1.

Note that $\boldsymbol{F}_0(\hat{\boldsymbol{r}})$ in (E.5) depends **exclusively** on the direction of the observation point relative to the location of the n$^{\text{th}}$ element[3]. Moreover, unlike in the array far-field, the radiation vector cannot be factored out of the summation and, therefore, an array factor cannot be defined anymore.

[3]– as this last one is a far-field measure with respect to such an element.

By properties of the operators in (1.7), given that the argument of $\boldsymbol{A}_0^{\text{FF}}(\boldsymbol{r})$ in (E.5) is simply translated on every summation term, the total radiated field in the array near-field region can be written as:

$$\boldsymbol{E}(\boldsymbol{r}) = -\jmath\, k\eta \sum_{n=1}^{N} I_n\, G(\boldsymbol{r}-\boldsymbol{r}_n)\, \boldsymbol{F}_{0,\perp}\left(\frac{\boldsymbol{r}-\boldsymbol{r}_n}{|\boldsymbol{r}-\boldsymbol{r}_n|}\right). \tag{E.6}$$

Note also that, for the general case of dual polarized transmitting antennas, the net radiated field can be written in terms of its p polarization as:

$$E_{\text{p}}(\boldsymbol{r}) = -\jmath\, k\eta \sum_{n=1}^{N} I_n\, a_{n,\text{p}}(\boldsymbol{r}). \tag{E.7}$$

where $a_{n,\text{p}}(\boldsymbol{r})$ is an order-2 tensor quantity called here the generalized array manifold, formally defined as:

$$a_{n,\text{p}}(\boldsymbol{r}) := G(\boldsymbol{r}-\boldsymbol{r}_n)\, F_{0,\text{p}}\left(\frac{\boldsymbol{r}-\boldsymbol{r}_n}{|\boldsymbol{r}-\boldsymbol{r}_n|}\right) \forall\, n \leq N, \tag{E.8}$$

with $G(\boldsymbol{r}-\boldsymbol{r}_n)$ being the translation of the Green function of (1.13) and $F_{0,\text{p}}(\boldsymbol{r})$ denoting the radiation vector along the p direction of polarization[4].

Observe that, if single p-polarized radiation is considered, the array manifold in (E.8) collapses into a vector simply denoted $\boldsymbol{a}_{\text{p}}(\boldsymbol{r}) \in \mathbb{C}^N$.

Moreover, if (E.6) is to be evaluated in the array far-field region (i.e. if $|\boldsymbol{r}| > r_{\text{FF}}$), the conventional array factor can be recovered by replacing the Green function with its far-field approximation of (1.16). Thus, showing that (E.8) indeed generalizes the array manifold with the array far-field region as a special case.

[4]note that $\hat{\boldsymbol{p}}$ must always be orthogonal to $\hat{\boldsymbol{r}}$.

Appendix F

Publications

Accepted articles

- **J. C. Bucheli Garcia, M. Kamoun and A. Sibille, "Digital vs. analog coherent combining on RL-ESPAR antennas," 2018 IEEE Wireless Communications and Networking Conference (WCNC), Barcelona, 2018, pp. 1-6.**

  DOI: 10.1109/WCNC.2018.8377392

  Abstract: The reactively loaded parasitic array radiator (RL-ESPAR) receiver has been acknowledged due to its compactness, fabrication cost and reconfigurability; showing significant beam-forming trade-off capabilities compared to conventional multi-element receiver ends. When used on reception, one relevant problem is to find the value of the reactance loadings to obtain the best signal to noise ratio performance. In the current paper, we compare the performance of digital and analog coherent combining over RL-ESPAR. Particularly, digital combining is realized by virtually rotating such a receiver and then applying the known maximum ratio combining (MRC) technique. On the other hand, analog combining is realized by synthesizing MRC on the reactance loadings via a technique that relies on the simultaneous perturbation stochastic approximation method (SPSA) method (widely applied on ESPAR in the literature). We show that analog combining exceeds digital combining and single dipole reception by around 3 dBs and 4 dBs via the proposed technique, respectively.

- **J. C. Bucheli Garcia, M. Kamoun and A. Sibille, "Reconfigurable passive relaying array for coverage enhancement," 2019 IEEE Wireless Communications and Networking Conference (WCNC), Marrakesh, Morocco, 2019, pp. 1-6.**

  DOI: 10.1109/WCNC.2019.8885448

  Abstract: The use of decode-and-forward (DAF) and amplify-and-forward (AAF) relays with the purpose of receiving and re-transmitting information has long been proposed. Nonetheless, DAF relays increase latency and AAF relays suffer from inherent stability issues due to potential echoes on the relayed signal. Alternatively, a passive relaying array (PRA) is proposed as a means of coping with both of the so-mentioned drawbacks. The role of PRA is that of capturing and scattering energy in a desired direction. The current work proposes a closed-form model for a dipole-based PRA with an electronically tunable response. The validation of the proposed model and the link budget for communication through the relay are also shown. Furthermore, given the non-linear relationship of PRA on the electronically tunable loads, the simultaneous perturbation stochastic approximation (SPSA) method is used as a means of finding the set of loads that maximizes energy transfer in a desired direction.

- **J. C. Bucheli Garcia, M. Kamoun and A. Sibille, "On the performance of ESPAR for spatial multiplexing in reception," 2019 IEEE Wireless Communications and Networking Conference (WCNC), Marrakesh, Morocco, 2019, pp. 1-5.**

  DOI: 10.1109/WCNC.2019.8885547

  Abstract: The electronically steerable parasitic array radiator (ESPAR) has been proposed as an inexpensive device for spatial multiplexing in transmission via the so-called beamspace modulation. On the other hand, spatial multiplexing (SM) is well known to allow a linear increase of capacity in MIMO systems with the number of antennas under rich scattering, unlike its corresponding logarithmic increase via signal to noise ratio (SNR). When it comes to ESPAR in reception for SM, nonetheless, the issue at hand is the so-called SNR degradation due to oversampling. In particular, oversampling is required given that, although all parasitic elements can be simultaneously controlled, up to a single simultaneous sample can be conveyed in reception. The counter intuitive role of the oversampling rate when seen as the number of spatial samples and its negative impact on SNR is studied in the present paper. It is shown that, from a capacity perspective, the ideal number

of spatial samples depends on both the SNR and channel conditions. Furthermore, an algorithm for capacity maximization over the set of reactive loads relying on the simultaneous perturbation stochastic approximation method (SPSA) is shown. Particularly, as an extension of previous work, such an algorithm converges to analog maximum ratio combining (A-MRC) when the oversampling rate is equal to one.

- **J. C. Bucheli Garcia, M. Kamoun and A. Sibille, "Low Complexity MRC for ESPAR Based on the Polynomial Expansion of the Admittance Matrix," 2019 IEEE International Conference on Communications (ICC), Shanghai, China, 2019, pp. 1-6.**

  DOI: 10.1109/ICC.2019.8761229

  Abstract: The electronically steerable parasitic array radiator (ESPAR) has been acknowledged as an inexpensive multiple antenna architecture. Nonetheless, due to the non-linear behavior on the loads used in its control, its related computational complexity can be prohibitive for practical implementations. The current paper deals with such an issue by proposing an approximation of its model via a truncated polynomial expansion of the inverse impedance matrix. The proposed approximation allows to reframe the problem of reactance optimization for beamforming, referred to as analog maximum ratio combining (A-MRC) in previous work. The method proposed in this paper provides a means to obtain a computationally efficient solution to the problem of reactance optimization and it avoids the need of an iterative-based approach. Therefore, resulting in a major computational complexity reduction with respect to related work in the literature.

- **J. C. Bucheli Garcia, A. Sibille and M. Kamoun, "Smart Dipole Arrays for Radio Channel Enhancement," 2020 IEEE European Conference in Antennas and Propagation (EuCAP).**

  DOI: pending, accepted for publication.

  Abstract: In this work we address the use of smart mirrors and smart scatterers as a way to enhance the radio channel properties from the point of view of the wireless link performance. The difference between both depends on their size, resulting in the 2nd or 4th power of the distance to the transmitter and the receiver, respectively, as explained on the basis of elementary electromagnetics. The performance of a smart device made of an array of dipoles in front of a perfectly conducting background reflector is subsequently analyzed, when operated

as a scatterer. A simple model explains well the scattering behavior, provided the size of the reflector is sufficient, resulting in a performance as scatterer varying as the square of the number of dipoles.

Under review

- **J. C. Bucheli Garcia, M. Kamoun and A. Sibille, "Low-complexity adaptive spatial processing of ESPAR antenna systems," currently under minor revision for journal IEEE Transactions on Wireless Communications.**

  Abstract: Accessing the spatial domain of wireless environments through antenna arrays has become key to improve the use of energy and, in light of this, there is an increasing need for low cost multi-antenna architectures. As one alternative, the Electronically Steerable Parasitic Array Radiator (ESPAR) was proposed as a coupling-based inexpensive option; allowing to significantly reduce the amount of required radio frequency (RF) front-ends. As a caveat, due to its inherent non-linear behavior, the required computational complexity can be prohibitive. Additionally, the unavailability of precise mutual coupling and channel state information (CSI) becomes a further issue difficult to avoid in practical setups. In this regard, the current work has two main contributions: a) it deals with the computational complexity by proposing the linearization of ESPAR's system model through the truncated Taylor expansion of the admittance matrix; facilitating the spatial processing algorithm of interest. Also, the authors propose b) to face the mutual coupling and CSI unavailability issue via the joint estimation of the channel-ESPAR parameters as directly observed through the single RF front-end. Relying on the optimization of the linearized system model, the pilot-based algorithm to be introduced allows ESPAR to track the configuration that synthesizes coherent combination at a significantly low complexity. Particularly, as shown through Monte-Carlo simulation, the latter allows to obtain 4 dB of array gain with a single RF front-end via a 5-element ESPAR.

- **J. C. Bucheli Garcia, A. Sibille and M. Kamoun, "Reconfigurable Intelligent Surfaces: Bridging the gap between scattering and reflection," for journal IEEE JSAC Special issue on Wireless Networks Empowered by Reconfigurable Intelligent Surfaces (JSAC-SI-RIS) 2019.**

  Abstract: In this work we address the distance dependence of reconfigurable intelligent surfaces (RIS). As differentiating factor to other works in the literature, we focus on the array near-field, what allows us to comprehend and expose the promising potential of RIS. The latter mostly implies an interplay between the physical size of the RIS and the size of the Fresnel zones at the RIS location, highlighting the major role of the phase.

  To be specific, the point-like (or zero-dimensional) conventional scattering characterization results in the well-known dependence with the fourth power of the distance. On the contrary, the characterization of its near-field region exposes a reflective behavior following a dependence with the second and third power of distance, respectively, for a two-dimensional (planar) and one-dimensional (linear) RIS. Furthermore, a smart RIS implementing an optimized phase control can result in a power exponent of four that, paradoxically, outperforms free-space propagation when operated in its near-field vicinity. All these features have a major impact on the practical applicability of the RIS concept.

  As one contribution of this work, the article concludes by presenting a complete signal characterization for a wireless link in the presence of RIS on all such regions of operation.

Non-peer-reviewed publications

- **J. C. Bucheli Garcia, A. Sibille and M. Kamoun, "Reconfigurable Intelligent Surfaces: Bridging the gap between scattering and reflection," December 2019. [Online].**
  Available: arXiv:1912.05344.

Appendix G

ESPAR in the literature

The following page contains a vectorized map with an overview of the main directions of research related to ESPAR in the scientific literature.

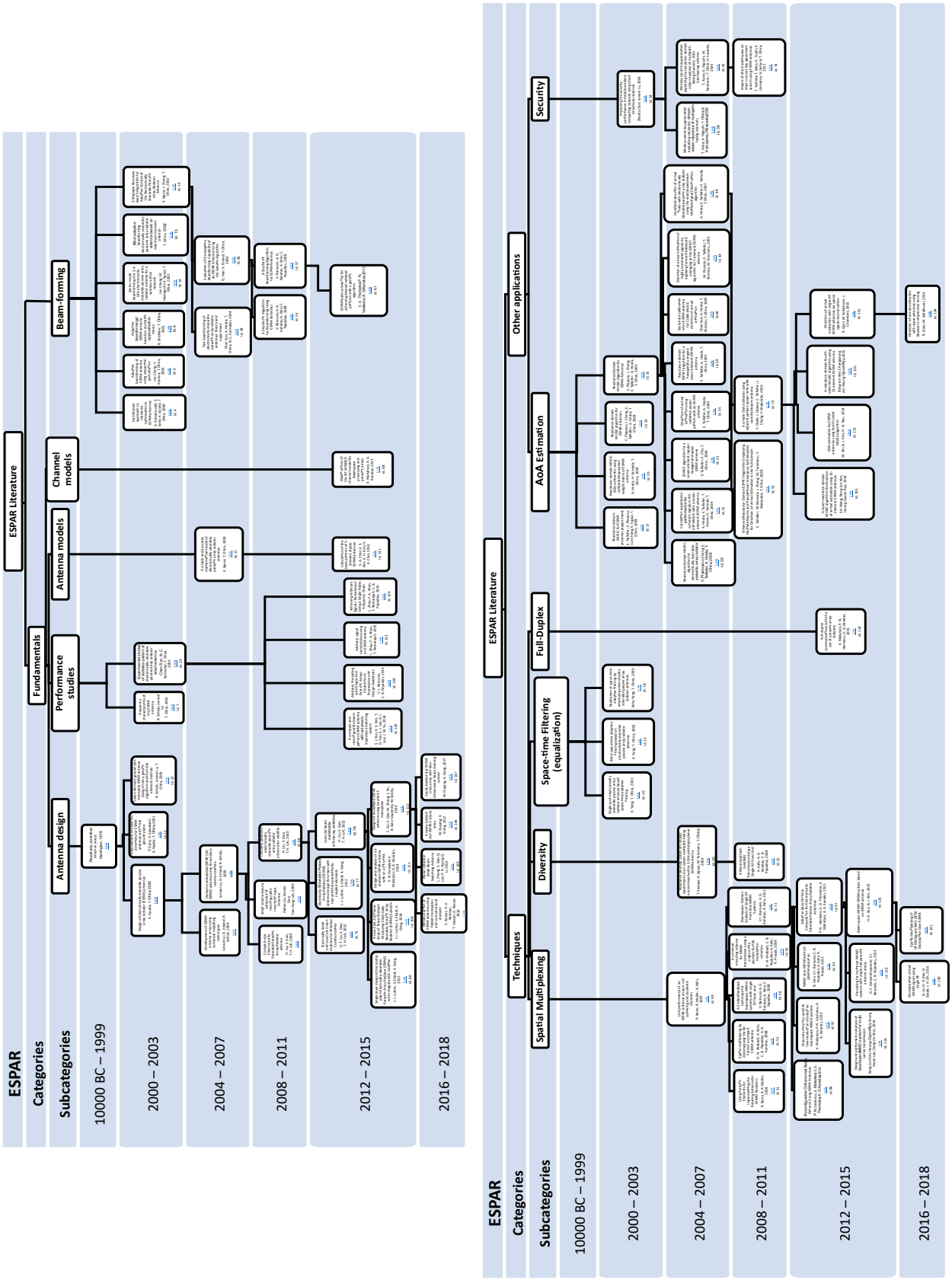

Figure G.1: Overview of ESPAR in the literature.

Bibliography

[1] R. E. Collin, "Limitations of the thevenin and norton equivalent circuits for a receiving antenna," *IEEE Antennas and Propagation Magazine*, vol. 45, pp. 119–124, April 2003.

[2] S. J. Orfanidis, "Electromagnetic waves and antennas,"

[3] J. Shaw, *Vector Calculus: With Applications to Physics*. D. Van Nostrand Company, 1922.

[4] C. A. Balanis, "Antenna theory: a review," *Proceedings of the IEEE*, vol. 80, pp. 7–23, Jan 1992.

[5] C. Balanis, *Antenna Theory: Analysis and Design*. Wiley, 2012.

[6] T. Bernabeu Jiménez, *Contribution to the physical interpretation of characteristic mode resonances. Application to dielectric resonator antennas*. PhD thesis, 2017.

[7] R. C. Hansen, "Relationships between antennas as scatterers and as radiators," *Proceedings of the IEEE*, vol. 77, pp. 659–662, May 1989.

[8] J. B. Andersen and A. Frandsen, "Absorption efficiency of receiving antennas," *IEEE Transactions on Antennas and Propagation*, vol. 53, pp. 2843–289, Sep. 2005.

[9] M. Karam and A. Fung, "Vector forward scattering theorem," *Radio Science*, vol. 17, no. 4, pp. 752–756, 1982.

[10] Feng Xia, Shaohui Quan, and Guoyu He, "Rcs calculations of resonant dipole antennas with arbitrary loads based on the equivalent circuit method," in *2008 8th International Symposium on Antennas, Propagation and EM Theory*, pp. 867–870, Nov 2008.

[11] A. Molisch, *Wireless Communications*. Wiley - IEEE, Wiley, 2010.

[12] B. Clerckx, C. Craeye, D. Vanhoenacker-Janvier, and C. Oestges, "Impact of antenna coupling on 2 × 2 mimo communications," *IEEE Transactions on Vehicular Technology*, vol. 56, pp. 1009–1018, May 2007.

[13] C. Craeye and D. González-Ovejero, "A review on array mutual coupling analysis," *Radio Science*, vol. 46, pp. 1–25, April 2011.

[14] R. Harrington, "Reactively controlled directive arrays," *IEEE Transactions on Antennas and Propagation*, vol. 26, pp. 390–395, May 1978.

[15] T. Ohira and K. Gyoda, "Electronically steerable passive array radiator antennas for low-cost analog adaptive beamforming," in *Proceedings 2000 IEEE International Conference on Phased Array Systems and Technology (Cat. No.00TH8510)*, pp. 101–104, May 2000.

[16] K. Gyoda and T. Ohira, "Design of electronically steerable passive array radiator (espar) antennas," IEEE Antennas and Propagation Society International Symposium, 2000.

[17] A. Kalis, A. G. Kanatas, and C. B. Papadias, "An espar antenna for beamspace-mimo systems using psk modulation schemes," 2007 IEEE International Conference on Communications, 2007.

[18] E. P. Tsakalaki, O. N. Alrabadi, C. B. Papadias, and R. Prasad, "Adaptive reactance-controlled antenna systems for multi-input multi-output applications," *IET Microwaves, Antennas Propagation*, vol. 5, pp. 975–984, June 2011.

[19] A. Kalis, A. G. Kanatas, and C. B. Papadias, *Parasitic Antenna Arrays for Wireless MIMO Systems*. Springer Publishing Company, Incorporated, 1st ed., 2016.

[20] Y. Ojiro, H. Kawakami, K. Gyoda, and T. Ohira, "Improvement of elevation directivity for espar antennas with finite ground plane," *IEEE Antennas and Propagation Society International Symposium. 2001 Digest. Held in conjunction with: USNC/URSI National Radio Science Meeting (Cat. No.01CH37229)*, 2001.

[21] R. Schlub, J. Lu, and T. Ohira, "Seven-element ground skirt monopole espar antenna design from a genetic algorithm and the finite element method," *IEEE Transactions on Antennas and Propagation*, 2003.

[22] H. Liu, S. Gao, and T. H. Loh, "Compact-size electronically steerable parasitic array radiator antenna," *2009 Loughborough Antennas Propagation Conference*, 2009.

[23] H. T. Liu, S. Gao, and T. H. Loh, "Electrically small and low cost smart antenna for wireless communication," *IEEE Transactions on Antennas and Propagation*, 2012.

[24] C. Gu, S. Gao, M. Zhang, L. Xu, B. Sanz-Izquierdo, and M. Sobhy, "Design of broadband espar antenna using inverted f monopoles," *The 8th European Conference on Antennas and Propagation (EuCAP 2014)*, 2014.

[25] J. J. Luther, S. Ebadi, and X. Gong, "Single-layer design of microstrip patch electrically-steerable parasitic array radiator (espar) with integrated dc isolation," *2012 IEEE/MTT-S International Microwave Symposium Digest*, 2012.

[26] J. J. Luther, S. Ebadi, and X. Gong, "A low-cost 2x2 planar array of three-element microstrip electrically steerable parasitic array radiator (espar) subcells," *IEEE Transactions on Microwave Theory and Techniques*, 2014.

[27] W. Ouyang and X. Gong, "A cavity-backed slot espar e-plane array," 2017 IEEE 18th Wireless and Microwave Technology Conference (WAMICON), 2017.

[28] W. Ouyang and X. Gong, "Cavity-backed slot espar cross array with two-dimensional beam steering control," 2017 IEEE International Symposium on Antennas and Propagation USNC/URSI National Radio Science Meeting, 2017.

[29] A. Komatsuzaki, S. Saito, K. Gyoda, and T. Ohira, "Hamiltonian approach to reactance optimization in espar antennas," 2000.

[30] J. Cheng, Y. Kamiya, and T. Ohira, "Adaptive beamforming of espar antenna using sequential perturbation," 2001 IEEE MTT-S International Microwave Sympsoium Digest (Cat. No.01CH37157), 2001.

[31] B. Shishkov and T. Ohira, "Adaptive beamforming of espar antenna based on stochastic approximation theory," APMC 2001. 2001 Asia-Pacific Microwave Conference (Cat. No.01TH8577), 2001.

[32] C. Sun, A. Hirata, T. Ohira, and N. C. Karmakar, "Fast beamforming of electronically steerable parasitic array radiator antennas: theory and experiment," IEEE Transactions on Antennas and Propagation, 2004.

[33] Q. Han, V. Briend, and T. Ohira, "Evaluation of the adaptive beamforming capability of an espar antenna using the genetic algorithm," 2006 European Conference on Wireless Technology, 2006.

[34] V. Barousis, A. G. Kanatas, A. Kalis, and C. Papadias, "A stochastic algorithm for beamforming using espar antennas," IEEE GLOBECOM 2008 - 2008 IEEE Global Telecommunications Conference, 2008.

[35] V. Barousis, A. G. Kanatas, A. Kalis, and C. Papadias, "A stochastic beamforming algorithm for espar antennas," *IEEE Antennas and Wireless Propagation Letters*, 2008.

[36] R. Bains, R. Muller, and A. Kalis, "Link performance of an espar-antenna array in rich scattering and clustered channels," 2007 4th International Symposium on Wireless Communication Systems, 2007.

[37] R. Bains and R. R. Muller, "Using parasitic elements for implementing the rotating antenna for mimo receivers," *IEEE Transactions on Wireless Communications*, 2008.

[38] O. N. Alrabadi, A. Kalis, C. B. Papadias, and A. G. Kanatas, "Spatial multiplexing by decomposing the far-field of a compact espar antenna," 2008 IEEE 19th International Symposium on Personal, Indoor and Mobile Radio Communications, 2008.

[39] O. N. Alrabadi, C. B. Papadias, A. Kalis, and R. Prasad, "A universal encoding scheme for mimo transmission using a single active element for psk modulation schemes," *IEEE Transactions on Wireless Communications*, 2009.

[40] B. Han, V. I. Barousis, C. B. Papadias, A. Kalis, and R. Prasad, "Mimo over espar with 16-qam modulation," *IEEE Wireless Communications Letters*, 2013.

[41] V. I. Barousis, A. G. Kanatas, and A. Kalis, "Beamspace-domain analysis of single-rf front-end mimo systems," *IEEE Transactions on Vehicular Technology*, 2011.

[42] P. N. Vasileiou, K. Maliatsos, E. D. Thomatos, and A. G. Kanatas, "Reconfigurable orthonormal basis patterns using espar antennas," *IEEE Antennas and Wireless Propagation Letters*, 2013.

[43] H. G. Ryu and B. J. Kim, "Beam space mimo-ofdm system based on espar antenna," 2015 International Workshop on Antenna Technology (iWAT), 2015.

[44] J. Lee, J. Y. Lee, and Y. H. Lee, "Spatial multiplexing of ofdm signals with qpsk modulation over espar," IEEE Transactions on Vehicular Technology, 2017.

[45] C. Plapous, Jun Cheng, E. Taillefer, A. Hirata, and T. Ohira, "Reactance domain music algorithm for electronically steerable parasitic array radiator," *IEEE Transactions on Antennas and Propagation*, vol. 52, pp. 3257–3264, Dec 2004.

[46] A. Hirata, H. Yamada, and T. Ohira, "Reactance-domain music doa estimation using calibrated equivalent weight matrix of espar antenna," in *IEEE Antennas and Propagation Society International Symposium. Digest. Held in conjunction with: USNC/CNC/URSI North American Radio Sci. Meeting (Cat. No.03CH37450)*, vol. 3, pp. 252–255 vol.3, June 2003.

[47] E. Taillefer, C. Plapous, Jun Cheng, K. Iigusa, and T. Ohira, "Reactance-domain music for espar antennas (experiment)," in *2003 IEEE Wireless Communications and Networking, 2003. WCNC 2003.*, vol. 1, pp. 98–102 vol.1, March 2003.

[48] E. Taillefer, A. Hirata, and T. Ohira, "Reactance-domain esprit algorithm for a hexagonally shaped seven-element espar antenna," *IEEE Transactions on Antennas and Propagation*, vol. 53, pp. 3486–3495, Nov 2005.

[49] R. Qian, M. Sellathurai, and J. Chambers, "Direction-of-arrival estimation with single-rf espar antennas via sparse signal reconstruction," in *2015 IEEE 16th International Workshop on Signal Processing Advances in Wireless Communications (SPAWC)*, pp. 485–489, June 2015.

[50] R. Qian and M. Sellathurai, "Direction-of-arrival estimation with espar antennas using bayesian compressive sensing," in *2016 IEEE International Conference on Acoustics, Speech and Signal Processing (ICASSP)*, pp. 3076–3080, March 2016.

[51] M. Rzymowski and L. Kulas, "Influence of espar antenna radiation patterns shape on ppcc-based doa estimation accuracy," in *2018 22nd International Microwave and Radar Conference (MIKON)*, pp. 69–72, May 2018.

[52] M. Groth and L. Kulas, "Accurate ppcc-based doa estimation using multiple calibration planes for wsn nodes equipped with espar antennas,"

in *2018 15th European Radar Conference (EuRAD)*, pp. 545–548, Sep. 2018.

[53] M. Plotka, M. Tarkowski, K. Nyka, and L. Kulas, "A novel calibration method for rss-based doa estimation using espar antennas," in *2018 22nd International Microwave and Radar Conference (MIKON)*, pp. 65–68, May 2018.

[54] J. S. K. Raj, A. S. Prabu, N. Vikram, and J. Schoebel, "Spatial correlation and mimo capacity of uniform rectangular dipole arrays," *IEEE Antennas and Wireless Propagation Letters*, vol. 7, pp. 97–100, 2008.

[55] B. Han, A. Kalis, and R. Prasad, "Matching parasitic antenna for single rf mimo," in *2012 International Conference on Microwave and Millimeter Wave Technology (ICMMT)*, vol. 1, pp. 1–4, May 2012.

[56] S. Yoo, K. Kim, T. Yeo, S. Lee, D. Lee, and J. Yu, "A compact and reconfigurable beam pattern espar antenna with automatic impedance matching system," in *2014 44th European Microwave Conference*, pp. 53–56, Oct 2014.

[57] J. Bucheli, M. Kamoun, and A. Sibille, "Digital vs. analog coherent combining on RL-ESPAR antennas," 2018 IEEE Wireless Communications and Networking Conference (WCNC), 2018.

[58] S. A. Mitilineos, K. S. Mougiakos, and S. C. A. Thomopoulos, "Design and optimization of espar antennas via impedance measurements and a genetic algorithm [antenna designer's notebook]," *IEEE Antennas and Propagation Magazine*, vol. 51, no. 2, pp. 118–123, 2009.

[59] R. Bains, *On the Usage of Parasitic Antenna Elements in Wireless Communication Systems*. PhD thesis, Norwegian University of Science and Technology, May 2008.

[60] B. Ricaud and B. Torresani, "A survey of uncertainty principles and some signal processing applications," 2012, 1211.5914.

[61] A. Akeyama, T. Suzuki, and T. Hanazawa, "Mobile radio telephone system for express highways," in *30th IEEE Vehicular Technology Conference*, vol. 30, pp. 499–504, Sep. 1980.

[62] C. Song, K. Lee, and I. Lee, "Designs of mimo amplify-and-forward wireless relaying networks: Practical challenges and solutions based on mse decomposition," *IEEE Access*, vol. 5, pp. 9223–9234, 2017.

[63] M. S. Elbamby, C. Perfecto, M. Bennis, and K. Doppler, "Edge computing meets millimeter-wave enabled vr: Paving the way to cutting the cord," in *2018 IEEE Wireless Communications and Networking Conference (WCNC)*, pp. 1–6, April 2018.

[64] J. Shen, Y. Oda, T. Furuno, T. Maruyama, and T. Ohya, "A novel approach for capacity improvement of 2x2 mimo in los channel using reflectarray," in *2011 IEEE 73rd Vehicular Technology Conference (VTC Spring)*, pp. 1–5, May 2011.

[65] E. Björnson, . Özdogan, and E. G. Larsson, "Intelligent reflecting surface vs. decode-and-forward: How large surfaces are needed to beat relaying?," *IEEE Wireless Communications Letters*, pp. 1–1, 2019.

[66] Y. Han, W. Tang, S. Jin, C. Wen, and X. Ma, "Large intelligent surface-assisted wireless communication exploiting statistical csi," *IEEE Transactions on Vehicular Technology*, vol. 68, pp. 8238–8242, Aug 2019.

[67] E. Basar, M. Di Renzo, J. De Rosny, M. Debbah, M. Alouini, and R. Zhang, "Wireless communications through reconfigurable intelligent surfaces," *IEEE Access*, vol. 7, pp. 116753–116773, 2019.

[68] J. C. Bucheli Garcia, M. Kamoun, and A. Sibille, "On the performance of espar for spatial multiplexing in reception," in *2019 IEEE Wireless Communications and Networking Conference (WCNC)*, pp. 1–5, April 2019.

[69] Özgecan Özdogan, E. Björnson, and E. G. Larsson, "Intelligent reflecting surfaces: Physics, propagation, and pathloss modeling," 2019, 1911.03359.

[70] S. Haykin and S. Haykin, *Adaptive Filter Theory*. Pearson, 2014.

[71] J. C. Spall, "Multivariate stochastic approximation using a simultaneous perturbation gradient approximation," *IEEE Transactions on Automatic Control*, vol. 37, pp. 332–341, March 1992.

[72] K. Kreutz-Delgado, "The complex gradient operator and the cr-calculus," 2009, 0906.4835.

[73] S. Haykin and S. Haykin, *Adaptive Filter Theory*. Pearson, 2014.

[74] D. T. M. Slock, "On the convergence behavior of the lms and the normalized lms algorithms," *IEEE Transactions on Signal Processing*, vol. 41, pp. 2811–2825, Sep. 1993.

TELECOM Paris

IP PARIS

Titre : Aspects électromagnétiques d'ESPAR et des diffuseurs contrôlables numériquement avec un regard sur la conception d'algorithmes de faible complexité

Mots clés : Antennes intelligentes, ESPAR, diffuseurs contrôlables numériquement, faible complexité, algorithme.

Résumé : Cette thèse se concentre sur l'idée d'exploiter le domaine spatial (contrairement à l'exploitation de la ressource temps-fréquence) des environnements sans fil à partir de deux fronts: a) Antennes ESPAR (pour Electronically Steerable Parasitic Array Radiator) comme alternative peu coûteuse au multi-conventionnel architectures d'antennes (peu coûteuses par rapport au nombre de frontaux radiofréquences que ces architectures conventionnelles sont souvent supposées fournies), et b) l'étude de réseaux d'antennes chargés de manière réactive pour fournir une diffusion contrôlable comme moyen d'ajouter des degrés de liberté à l'environnement de propagation lui-même. Ce dernier est atteint ici via des diffuseurs contrôlables numériquement (DCS).
En particulier, la thèse se concentre sur l'objectif de mieux conditionner les problèmes d'optimisation comme moyen de proposer des algorithmes de faible complexité. Par conséquent, un aspect clé est l'équilibre requis entre la précision et la complexité des modèles électromagnétiques adoptés. Ainsi, il convient de souligner l'importance accordée à l'interface entre l'électromagnétisme et la caractérisation du signal. Plus précisément, ESPAR et DCS nécessitent la compréhension des phénomènes électromagnétiques (EM) qui ne sont pas entièrement pris en compte dans les descriptions conventionnelles au niveau des liaisons. Plus important encore, ce dernier est la preuve de la nécessité de rejoindre les approches de deux communautés de recherche apparentées pour faire face à la rareté des ressources qui ne devrait qu'augmenter dans les décennies à venir.
En fait, le document est principalement positionné du point de vue d'une personne ayant une formation en télécommunications (contrairement à l'électromagnétisme pur) et qui cherche à éclairer les mécanismes EM sousjacents. Il se compose approximativement de trois parties, à savoir: les principes fondamentaux, l'antenne ESPAR et les diffuseurs contrôlables numériquement. En fait, le but d'avoir une partie du document consacrée uniquement aux fondamentaux est de décrire les phénomènes EM tout en mettant en évidence tous les détails pertinents pour les deux autres.
La partie "fondamentaux" commence par les équations de Maxwell (et leur solution pratique pour les problèmes derayonnement en champ lointain) jusqu'à la caractérisation bien connue du signal y = hx + n. En tant que description apparemment la moins appropriée pour travailler avec, mais la caractérisation la plus complète des phénomènes EM, les équations de Maxwell sont la base qui relie notre description mathématique à la même réalité. Ainsi, l'objectif de cette partie est d'exposer la connexion entre champs et signaux, ainsi que d'ouvrir la porte à la remise en cause du modèle conventionnel de signal émetteur-récepteur.
Pour continuer, la deuxième partie est consacrée à l'antenne ESPAR. En particulier, ESPAR nous oblige à s'écarter de l'espace de signal abstrait dans lequel les caractérisations traditionnelles au niveau de la liaison multi-antennes sont représentées. En tant que contribution de ce travail, il sera montré comment une approximation locale du modèle de système offre une vue alternative. Notamment, grâce à une telle approximation du modèle de système, une solution efficace sur le plan informatique au problème non trivial de l'adaptation basée sur les canaux des caractéristiques de rayonnement d'ESPAR est trouvée.
Enfin et surtout, la troisième partie traite des diffuseurs à commande numérique comme moyen d'améliorer l'efficacité énergétique. Un concept aussi passionnant a attiré une attention considérable ces dernières années et, en un sens, ouvre la porte à une manière radicalement différente de concevoir les problèmes de communication. Même si ces appareils en sont à leurs balbutiements, il n'est pas difficile pour moi d'imaginer comment les décennies à venir pourraient être marquées par la massification de cette technologie.

Title : Electromagnetic aspects of ESPAR and digitally controllable scatterers with a look at low-complexity algorithm design

Keywords : Smart antennas, ESPAR, digitally controllable scatterers, low complexity, algorithm.

Abstract : The thesis focuses on the idea of exploiting the spatial domain (as opposed to the exploitation of the time-frequency resource) of wireless environments from two fronts: a) ESPAR antennas (standing for Electronically Steerable Parasitic Array Radiator) as a potential inexpensive alternative to conventional multi-antenna architectures (inexpensive in relation to the number of radio frequency front-ends these conventional architectures are often assumed to be provided with), and b) the study of reactively loaded arrays to deliver controllable scattering as a mean of adding degrees of freedom to the propagation environment itself. The latter is achieved here via digitally controllable scatterers (DCS).

Particularly, the thesis focuses on the goal of better conditioning optimization problems as means of proposing low-complexity algorithms. Therefore, one key aspect is the required balance between the accuracy and complexity of the adopted electromagnetic models.

Thus, it is appropriate to highlight the importance given to the interface between electromagnetism and the signal characterization. More specifically, both ESPAR and DCS require the understanding of electromagnetic (EM) phenomena that is not fully accounted for through conventional link-level descriptions. More importantly, the latter is proof of the need to join the approaches of two related research communities to cope with the scarcity of resources that is only expected to grow in the decades to come.

In fact, the document is mostly positioned from the view of someone with a background in telecommunications (unlike pure electromagnetism) with looks at enlightening the underlying EM mechanisms. It is roughly composed of three parts, namely: fundamentals, the ESPAR antenna and digitally controllable scatterers. In fact, the aim of having one part of the document dedicated purely to fundamentals is to describe the EM phenomena while highlighting all relevant details to the remaining two.

The part "fundamentals" begins with Maxwell's equations (and their convenient solution for far-field radiation problems) all the way to the well-known $y = hx + n$ signal characterization. As the seemingly least appropriate description to work with, but most complete characterization of the EM phenomena, Maxwell's equations are the basis that link our mathematical description to the very same reality. Thus, the objective of this part is to expose the connection between fields and signals, as well as to open the door to questioning the conventional transmitter-receiver signal model. The latter becomes one of the most exciting outcomes of this project in line with the research-related aim of challenging our vision to expand our understanding of a problem.

To continue, the second part is dedicated to the ESPAR antenna as a preamble of what is meant by "questioning the conventional transmitter-receiver signal model". Particularly, ESPAR obliges us to depart from the abstract signal space in which traditional multi-antenna link-level characterizations are depicted. As a contribution of this work, it will be shown how a local approximation of the system model offers an alternative view. Notably, through such an approximation of the system model, a computationally-efficient solution to the non-trivial problem of channel-based adaptation of the radiation characteristics of ESPAR is found.

Last, but not least, the third part deals with digitally controllable scatterers as a mean of improving energy efficiency. Such an exciting concept has gained significant attention in the recent years and, in a sense, opens the door to a radically different way to conceive communication problems. Even though these devices are in their infancy, it is not difficult for me to imagine how the decades to come could be marked by the massification of this technology.

Institut Polytechnique de Paris
91120 Palaiseau, France